Aeroelastic Investigation of a Wind Turbine Airfoil with Self-Adaptive Camber

Vom Fachbereich Maschinenbau
an der Technischen Universität Darmstadt
zur
Erlangung des Grades eines Doktor-Ingenieurs (Dr.-Ing.)
genehmigte

D i s s e r t a t i o n

vorgelegt von

Dipl.-Ing. Benjamin Lambie

aus Essen

Berichterstatter:	Prof. Dr.-Ing. C. Tropea
Mitberichterstatter:	Prof. Dr.-Ing. O. Paschereit
Tag der Einreichung:	27. April 2011
Tag der mündlichen Prüfung:	22. Juni 2011

Darmstadt 2011
D17

Eidesstattliche Erklärung

Hiermit erkläre ich an Eides statt, dass ich die vorliegende Dissertation selbstständig und nur mit den angegebenen Hilfsmitteln angefertigt habe.

Benjamin Lambie

Abstract

A load-dependent passive camber control concept is introduced for alleviating load fluctuations on wind turbine rotor blades with the overall goal of reducing fatigue and increasing durability and turbine lifetime. The passive change of the camber line is realized through kinematically coupled leading and trailing-edge flaps. The leading-edge flap is actuated by the increased pressure forces due to the change in angle of attack. The trailing-edge flap is kinematically coupled to the rotation of the leading-edge flap. This combined motion results in an increase or decrease in airfoil camber dependent on the pressure difference along the airfoil and the restoring force applied at the leading-edge flap. This concept works fully passive, i.e. its characteristics are determined solely by the fluid-structure interaction. The quantification of these aerodynamic characteristics is the objective of the present study.

The concept has been studied experimentally and numerically. The numerical simulations consider quasi-steady aerodynamics and the combined flap motion is described by one degree of freedom. The concept has been confirmed experimentally under quasi-steady conditions in the large scale low-speed wind tunnel at TU Darmstadt.

The structural parameters which characterize the flap deflections are investigated systematically. The results show how the lift curve slope can be adjusted by the preload moment, the stiffness and the coupling ratio between the leading and trailing-edge flap. It is shown that it is possible to keep the lift coefficient constant due to the self-adaptive camber line. The numerical model is compared to the experimental results. The model is able to predict the effects revealed through the wind tunnel measurements.

In the second part the numerical model of the airfoil section with lead-

ing and trailing-edge flaps is extended to consider also the bending and torsional degree of freedom. The results show that although the dynamic behavior of the blade changes significantly, load reduction is achieved and a flexible camber line is advantageous for the dynamic response of the rotor blade.

Finally the concept is evaluated with the wind turbine simulator FAST. The underlying look-up tables are modified to incorporate the flapped airfoil characteristics. The results provide a baseline for the evaluation of the concept in conjunction with the aerodynamics encountered by wind turbines.

Kurzfassung

Die vorliegende Arbeit befasst sich mit der Entwicklung eines aerodynamischen Profils mit kinematisch gekoppelter Vorder- und Hinterkantenklappe zur passiven Einstellung der Profilwölbung. Mit Hilfe dieses Konzeptes sollen Auftriebsschwankungen an Rotorblättern von Windkraftanlagen verringert werden. Damit wird das Ziel verfolgt die Lebensdauer und Zuverlässigkeit der Anlage und Komponenten zu erhöhen. Die Vorderkantenklappe wird über eine Feder vorgespannt, so dass Druckänderungen aufgrund von Anstellwinkeländerungen die Klappe bewegen. Durch eine kinematische Kopplung wird diese Bewegung an die Hinterkante übertragen. Diese gekoppelte Bewegung ermöglicht es die Wölbung des Profils entsprechend der Druckverteilung anzupassen. Das Verhalten dieses Konzeptes wird ausschließlich durch die Fluid-Struktur Interaktion bestimmt. Aufgabe der vorliegenden Arbeit ist dieses Verhalten zu untersuchen und zu quantifizieren.

Das Konzept wurde experimentell und numerisch untersucht. In den numerischen Simulationen wird die Strömung als quasi-stationär betrachtet. Die Klappenbewegung wird durch einen rotatorischen Freiheitsgrad beschrieben. Die experimentelle Machbarkeitsstudie wurde für das Konzept unter quasi-stationären Bedingungen im Niedergeschwindigkeitswindkanal der TU Darmstadt durchgeführt.

Die Strukturparameter, die das Wölbungsverhalten bestimmen, werden systematisch untersucht. Die Ergebnisse zeigen wie durch Einstellung des Vorspannmoments, der Steifigkeit und des Übersetzungsverhältnisses das Auftriebsverhalten beeinflusst wird. Dabei wird nachgewiesen, dass es möglich ist den Auftriebsbeiwert durch eine passive Wölbungsänderung konstant zu halten. Ein Vergleich des numerischen Modells mit den experimentellen Daten zeigt, dass die in den Messungen gefundenen Effekte

abgebildet werden.

Im zweiten Teil der Arbeit wird das numerische Strukturmodell um 2 weitere Freiheitsgrade erweitert. Das Profil wird zusätzlich in Hub- sowie Nickrichtung elastisch gelagert. Dadurch wird die Biege- und Torsionssteifigkeit des Rotorblattes abgebildet. Die Ergebnisse zeigen, dass obwohl sich das dynamische Verhalten des Rotorblattes entscheidend ändert, insgesamt eine Lastminderung erreicht wird und daraus geschlossen wird, dass die passive Wölbungsänderung vorteilhaft für die dynamische Antwort des Profils ist.

Abschließend wird das Konzept mit Hilfe des Windturbinen Simulationsprogramms FAST untersucht. Die hinterlegten Profilpolaren wurden derart verändert, dass sie die ermittelten Profilcharakteristiken der sich anpassenden Wölbung berücksichtigen. Die Ergebnisse liefern die Basis für die Bewertung des Konzepts im Zusammenhang mit den Betriebsbedingungen, die eine Windkraftanlage erfährt.

Danksagung

Die vorliegende Dissertation entstand während meiner Tätigkeit im Forschungsbereich Drag and Circulation Control des Exzellenzclusters Center of Smart Interfaces der TU Darmstadt.

Der Deutschen Forschungsgemeinschaft (DFG) möchte ich für die Förderung dieser Untersuchung danken.

Dem Direktor des Center of Smart Interfaces und Leiter des Fachgebiets für Strömungslehre und Aerodynamik Herrn Prof. Dr.-Ing. Cameron Tropea gilt mein ausdrücklicher Dank für die Förderung und Betreuung dieser Arbeit, sowie das mir entgegengebrachte Vertrauen. Sein Engagement und das Stellen entscheidender Fragen haben maßgeblich zum Erfolg dieser Arbeit beigetragen.

Herrn Prof. Dr.-Ing. Oliver Paschereit, Leiter des Fachgebiets Experimentelle Strömungsmechanik der TU Berlin, gilt mein Dank für die Übernahme des Korreferats.

Herrn Dr.-Ing. Klaus Hufnagel danke ich ganz besonders für die vielen Gespräche und Diskussionen, die zum Gelingen der Arbeit beigetragen haben.

Herrn Dr. rer.nat. Wolfgang Send danke ich herzlich für die vielen Gespräche und Erklärungen sowie die Hilfe bei der Modellierung der instationären Aerodynamik.

Den Leitern des Forschungsbereiches Drag and Circulation Control Frau Dr.-Ing. Bettina Frohnapfel und Herr Dr.-Ing. Sven Grundmann danke ich für ihre stete Unterstützung.

Ich bedanke mich bei allen Kollegen vom Fachgebiet Strömungslehre und Aerodynamik und Center of Smart Interfaces für die gute Zusammenarbeit, die vielen Anregungen und die nette Atmosphäre in Griesheim. Insbesondere danke ich Herrn Dipl.-Ing. Andreas Güttler für die gute

Zusammenarbeit und vor allem für die große Unterstützung beim Bau des Windkanalmodells. Ebenso möchte ich mich bei Herrn Dipl.-Ing. Andreas Reeh bedanken. Herrn Dipl.-Ing. Matthias Quade danke ich für das Erstellen des LabView Programms.

Den Herren cand.-Ing Alexander Krenik und Manuel Jain, B.Sc., gilt mein ganz besonderer Dank für den enormen Einsatz und die Mitarbeit an diesem Projekt. Ihre Arbeiten haben außerordentlich zum Gelingen dieser Dissertation beigetragen. Weiterhin möchte ich den Herren cand.-Ing. Andreas Ferber, Dipl.-Ing. Nima Aghajari, Dipl.-Ing. Roman Braun und Dipl.-Wirtsch.-Ing. Norbert Enste danken.

Für die gute Zusammenarbeit auf dem Gebiet der Strukturmodellierung bedanke ich mich bei Herrn Dr.-Ing. Gottfried Spelsberg-Korspeter und meinem guten Freund Dipl.-Ing. Steffen Wiendl vom Fachgebiet Dynamik und Schwingungen.

Weiterhin möchte ich mich bei allen Mitarbeitern der Werkstätten in Griesheim für den tatkräftigen Einsatz beim Bau des Windkanalmodells und allen weiteren Komponenten bedanken.

Benjamin Lambie
April 2011

Contents

Nomenclature

Roman Notation

A	$[-]$	influence coefficients of source
a	$[-]$	translation vector
B	$[-]$	influence coefficients of vortex or basis of body fixed reference system
b	[m]	span
C	$[-]$	influence coefficients of discrete vortex wake
c	[m]	chord
c_D	$[-]$	drag coefficient
c_L	$[-]$	lift coefficient
c_M	$[-]$	moment coefficient
c_p	$[-]$	pressure coefficient
c_P	$[-]$	power coefficient
D	$[-]$	influence coefficients of shed vortex
d_β	$[\frac{\text{Nms}}{\text{rad}}]$	torsional damper constant
E	$[-]$	rotation matrix
F_B	[N]	aerodynamic force at leading-edge flap
F_C	[N]	aerodynamic force at main wing
F_D	[N]	aerodynamic force at trailing-edge flap
k	$[-]$	reduced frequency
k_h	$[\frac{\text{N}}{\text{m}}]$	bending stiffness
k_γ	$[\frac{\text{Nm}}{\text{rad}}]$	torsional spring constant at leading edge
k_θ	$[\frac{\text{Nm}}{\text{rad}}]$	torsional stiffness
M_B	[Nm]	aerodynamic moment at leading-edge flap

M_C	[Nm]	aerodynamic moment at main wing
M_D	[Nm]	aerodynamic moment at trailing-edge flap
M_y	[Nm]	blade root bending moment
M_t	[Nm]	rotor torque
m_l	[Nm]	mass of leading-edge flap
m_f	[Nm]	mass of main wing
m_t	[Nm]	mass of trailing-edge flap
N	$[-]$	basis of inertial frame of reference
n	$[-]$	coupling ratio or normal vector
q_1	[m]	heaving motion
q_2	$[^\circ]$	pitching motion
q_3	$[^\circ]$	flap motion
q_∞	$[\frac{\mathrm{N}}{\mathrm{m}^2}]$	dynamic pressure
V_∞	$[\frac{\mathrm{m}}{\mathrm{s}}]$	freestream velocity
V_w	$[\frac{\mathrm{m}}{\mathrm{s}}]$	wind velocity
v	$[\frac{\mathrm{m}}{\mathrm{s}}]$	velocity
r	[m]	distance or position vector
s	[m]	distance to center of gravity
T	[N]	rotor thrust
t	[s]	time

Greek Notation

α	$[^\circ]$	angle of attack
β	$[^\circ]$	trailing-edge flap angle
Γ	$[\frac{\mathrm{m}^2}{\mathrm{s}}]$	circulationn
γ	$[^\circ]$	leading-edge flap angle
ρ	$[\frac{\mathrm{kg}}{\mathrm{m}^3}]$	density of air ($= 1,204$)
ϕ	$[\frac{\mathrm{m}^2}{\mathrm{s}}]$	velocity potential
∇	$[-]$	Nabla-Operator
σ	$[\frac{\mathrm{m}}{\mathrm{s}}]$	source
σ	$[-]$	uncertainty
τ	$[\frac{\mathrm{m}}{\mathrm{s}}]$	vortex strength
θ_i	$[^\circ]$	panel inclination angle
θ_l	[kgm]	moment of inertia leading-edge flap
θ_f	[kgm]	moment of inertia main wing
θ_t	[kgm]	moment of inertia trailing-edge flap

ω	$[\frac{1}{s}]$	angular velocity

Indices

Subscripts

1, 2, 3	1, 2, 3 direction
A, B, C	body A, B, C
	A $\equiv$ leading-edge flap
	B $\equiv$ main wing
	C $\equiv$ trailing-edge flap
h	panel upstream
i	panel
ind	induced
j	source/vortex
k	time step
kin	kinematic
l	leading edge
m	vortex in wake
p	pitching
S	surface
St	stagnation point
t	trailing edge
w	vortex or wake
x, y, z	x, y, z direction

Superscripts

n	normal direction
t	tangential direction
$*$	leading-edge nose frame of reference
$'$	main wing frame of reference
$''$	leading-edge flap frame of reference
$'''$	trailing-edge flap frame of reference

Abbreviation

DOF	Degree of Freedom

FAST	Fatigue, Aerodynamics, Structures and Turbulence (turbine simulator)
GUM	Guide to the Expression of Uncertainty in Measurement
HSPM	Hess-Smith Panel Method
LR	Load Reduction
MC	Mean Change
RANS	Reynolds averaged Navier Stokes
RHS	Right Hand Side
SMA	Shape Memory Alloy
UHSPM	Unsteady Hess-Smith Panel Method

Chapter 1

Introduction

1.1 Motivation

The most effective way to increase the energy yield of a wind turbine is to increase the rotor diameter. This is clearly demonstrated by the rapid growth of wind turbine size during the last decade. Nevertheless, the power output of conventional wind turbines needs to be limited for reasons of structural strength and maximum generator power. The state of the art load control mechanisms and devices can be found in any standard textbook, e.g. Burton et al. (2001) can be recommended.

The optimal turbine design described by Betz (1926) assumes a constant wind speed over the rotor area. However, the velocity distribution over the rotor plane is inhomogeneous and characterized by random processes. According to IEC Norm 64-100 it can be distinguished between normal and extreme wind conditions. The temporal and spatial velocity at a point in the rotor plane is influenced by the atmospheric boundary layer, small scale turbulent fluctuations, large scale gusts and the interaction with the turbine itself. The associated aerodynamics are unsteady and 3-dimensional and its proper determination is the subject of current research activities.

All of these effects result in a variable inflow velocity and change in angle of attack along the rotor blade; hence changing lift forces. These load fluctuations will contribute to the fatigue loads of the blade and further turbine components, like the drivetrain. Design considerations

for enhancing the harvested power by increasing the rotor diameter lead to the conclusion that current devices, mechanisms and control strategies will reach their limits and/or do not remain to be the most effective and economic solution.

According to these aspects the need for novel wing technologies has increased. Two main areas can be defined. First, the smart wing concept is an attempt to improve performance actively by an integrated device. Second, the wing design process called "Aeroelastic Tailoring" has become common place. The aim of the latter is the controlled deformation of the structure after aerodynamic loads are applied. An active system takes advantage of a feedback control and an enhanced parameter space, whereas a passive concept exhibits advantages in terms of energy consumption and an expected higher system reliability. In addition to the differentiation of active and passive shape change concepts one can further explore whether the whole rotor blade is affected or only a specific section.

A comprehensive review of active flow control technologies and their suitability for wind turbine is given by Johnson, van Dam and Berg (2008). Barlas and van Kuik (2010) give an overview of the challenges in the design of future wind turbines, focusing on smart rotor control and modeling problems. They point out that with increasing blade lengths, the aerodynamics along the span may vary significantly, thus devices which only influence sectional aerodynamics may be appropriate and preferable. Furthermore an increased blade flexibility may lead to the fact that the application of a root pitching moment is not adequate to twist the outer part of the blade. Nevertheless, further research is required to evaluate and compare the performance of various solutions, either passive or active. Especially the fact that the rotor blade pricing in price per kilogram, which is about a magnitude less than of a civil aircraft, determines the evaluation base of any additional component to the rotor blade. Furthermore, maturity and reliability of the devices need to be guaranteed.

In the next paragraphs only shape changing concepts are considered and the various approaches are characterized as follows.

The pitch control system is in this context state of the art and can be classified as an active system which effects the flow along the entire blade.

To avoid pitch actuation and therefore preserving the pitch bearing the bend twist coupled rotor blade concept stipulates to change the blade twist passively, i.e. solely by the fluid forces. An increase in the bending

deflection due to higher aerodynamic loads will induce shear forces which in turn twist the blade since a kinematic coupling is enabled by the fibre directions, see Veers, Bir and Lobitz (1998) and Ferber (2010). This concept has not reached maturity phase.

An active approach for the control of sectional aerodynamics is the change of the camber line by trailing-edge flaps. Flaps are state of the art in aircraft-wing technology and it is known that the influence on the lift is decisive. Significant load reductions have been determined by Buhl, Gaunaa and Bak (2005) and the main contributions derive from research groups at Risø DTU, TU Delft and Sandia National Laboratories. It has been shown by Berg et al. (2009) that active trailing-edge flaps can reduce the fatigue loads of the root bending moment about 24%. However, suitable sensors still seem to be an outstanding challenge, as stated by Behrens and Zhu (2011).

A load-limiting sandwich structure has been developed by VVT (Sippola and Lindroos, 2009) using SMA material. This enabled them to include a degressive stiffness in the trailing-edge part of the airfoil section. A gust load will increase the force on the airfoil which in turn should deflect the trailing edge; hence reducing the camber line. According to the authors knowledge an elastic trailing edge is not very effective as figured out by numerical computations of an elastically mounted trailing-edge flap (Lambie, Krenik and Tropea, 2010). The reason is that by assuming a constant pitch angle and rotor speed a change in the wind speed affects mainly the angle of attack. Hence the load change (pressure difference) appears mainly in the front part of the airfoil. However, these pressure differences would be the actuation forces for a passive concept. At least this is true for spanwise sections were the angular speed of the rotor is significantly higher (near the tip speed ratio) than the wind speed. These are the outboard parts of the rotor where a camber change device (either active of passive) would be implemented since these parts have the most impact on the integral load of the rotor, see Andersen et al. (2006).

But then an elastically mounted trailing-edge flap might be an effective concept for aircraft wings when it is designed for different flight speeds. One concept for example has been pended as a patent by Messerschmidt in 1933, see Figure 1.1. Since the dynamic pressure is a function of velocity the actuating forces at the trailing edge change. Modern wind turbines also adjust the angular rotor speed to increase the rotor efficiency at certain wind speeds, which results in different inflow velocities; hence

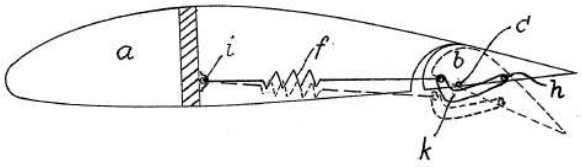

Figure 1.1: Willy Messerschmidts patent of an airfoil with flap for self-adaptive lift control; patent number: 639 329 (28 June 1933).

dynamic pressure.

The above mentioned aspects show that an airfoil with a self-adaptive camber line combines the advantages of a sectional device for lift control with the robustness of a passive approach. The development and investigation of such a concept is the primary goal of the present study. The invention will overcome the drawback experienced by the concepts utilizing only a flexible trailing edge. This study fills the gap of a missing concept for passive camber change and to the author's knowledge such a device is not under investigation in the wind turbine research community.

1.2 Concept and Objectives

The novel concept uses the pressure changes to adjust the airfoil camber through kinematically coupled leading and trailing-edge flaps. The concept is pictured in Figure 1.2. The leading-edge flap is actuated by the increased pressure forces due to the change in angle of attack. The trailing-edge flap is kinematically coupled to the rotation of the leading-edge flap. This combined motion results in an increase or decrease in airfoil camber dependent of the pressure difference along the airfoil. The linkage of the aerodynamic forces and structural deflections via the leading and the trailing edge of the airfoil is the key feature of the concept. The leading-edge flap is pretensioned by a spring, providing a restoring force. The restoring force is a function of the design point. A damper at the trailing-edge flap stabilizes the system. Mechanical stoppers offer the possibility to restrict the total change of the flap angles to a certain range. This concept works fully passive, i.e. its characteristics are determined solely by the fluid-structure interaction.

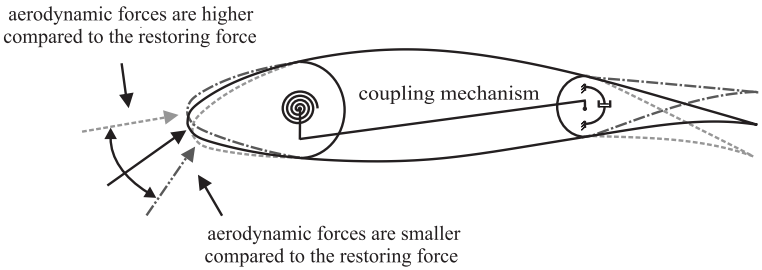

Figure 1.2: Novel concept: airfoil with kinematically coupled leading and trailing-edge flaps; pended as a patent by TU Darmstadt, Klaus Hufnagel and Benjamin Lambie on 11 May 2010 (EP10162448.4)

The main objectives of the investigation of the novel concept may be summarized as follows:

- Exploration of the characteristics of the novel concept and discussion of how the fluid-structure interaction can be used for flow control purposes
- Identification of the critical structural parameters, such as geometric shape and structural properties
- Experimental Proof of Concept under quasi-steady conditions
- Determination of the interaction between the flap motion and the wing motion
- Determination and exploration of the concept in conjunction with the conditions encountered by a wind turbine
- Estimation and discussion of the obtained load reduction

Some research groups in the past have designed and computed airfoils with a flexible camber line, motivated largely by aeroelastic stability problems and the design of Micro Air Vehicles (MAV), where wing flexibility provides some benefits. Especially in the design activities for smart wing developments it is often stated that the main goal is to develop a wing or airfoil without any gaps and where the flexibility is incorporated in the structural design.

However, regarding to the author's opinion the best approach is to consider the variable camber concept by means of elastically coupled rigid bodies. This ensures that from both the aerodynamic point of view and the structural point of view, the most penetrating insight into the interaction can be obtained. The reduction of structural degrees of freedom allows a very efficient description of the structural model. Furthermore it allows to adjust the structural properties by single parameters like spring stiffness, preload moment or coupling ratio. The same holds for the aerodynamics when keeping in mind that the surface change needs to be computed and measured in the experiment. These are essential arguments for the decision to use rigid bodies.

1.3 Thesis Outline

The thesis will address the above mentioned questions and objectives in the following chapters:

Chapter 2 will introduce the developed numerical models used to describe the fluid-structure interaction. A method is introduced to describe the kinematic boundary condition for the airfoil motion, including pitching, heaving and flap motions. The flow field is obtained from the Hess-Smith panel method based on potential theory. The structural equation of motion for the respective degrees of freedom are derived. The aeroelastic model assumes attached flow. In addition to XFoil computations RANS simulations were performed for the investigation of Reynolds number effects.

Chapter 3 describes the experimental setup and measurement techniques. The post-processing methods and measurement uncertainties are introduced.

Chapter 4 presents the results of the aeroelastic investigation of the flapped airfoil. Only the flap motion is considered. The aerodynamics are steady. The results determine the design of the experimental wing.

Chapter 5 contains the results of the wind tunnel investigation. These results confirm the success of the concept under quasi-steady conditions. The influence of flow velocity, angle of attack, preload moment, spring stiffness and coupling ratio are characterized and quantified. A comparison to theoretical results will be given.

Chapter 6 presents the results for the structural behavior when the

pitching and heaving motion of the airfoil is considered in the aeroelastic model. An outlook about the difference between the assumption of steady aerodynamics and unsteady computations is presented.

Chapter 7 exhibits results obtained with the turbine simulator FAST. The underlying look-up tables are modified to incorporate the flapped airfoil characteristics. The results provide a baseline to which the influence of the concept in conjunction with the aerodynamics of wind turbines can be evaluated.

Chapter 2

Numerical Models

In the following chapter numerical models will be developed to simulate the aerodynamic performance of the flapped airfoil under various boundary conditions. Such simulations are essential in the design process for two reasons. First, they complement experimental investigations, where not all parameter variations can be explored. Second, not all necessary quantities can be measured during the experiment, but are available from the associated simulations. The results will provide along with the experimental observation the necessary insight to evaluate the novel concept. However, some assumption have to be made in the numerical model to allow an efficient implementation. The mathematical description and the underlying assumptions are object of the present chapter.

2.1 Potential Flow Model

The following sections describe the Hess-Smith panel method to determine the potential flow field of a pitching and plunging airfoil with flaps. More general formulations can be found in the textbooks of Katz and Plotkin (2001) and Cebeci et al. (2005).

2.1.1 Basic Formulation

The solution of the flow field is restricted to the determination of the velocity and pressure distribution around the airfoil. Consider the airfoil of Figure 2.1 in the fluid domain V with boundaries at infinity to designate free flow condition. The airfoil surface S_B is known in the body-fixed reference system B^*. The wake S_w behind the airfoil is given by the path of the trailing edge. The problem is assumed to be two-dimensional. To obtain the velocity and pressure field around the airfoil the following assumptions are made to fulfill *Newton's* second law of motion and the law of conversation of mass and energy.

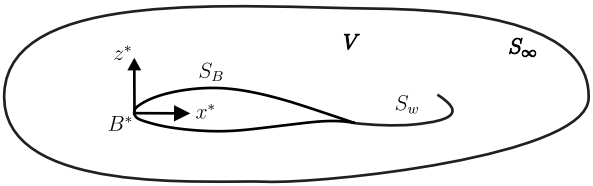

Figure 2.1: Airfoil surface and flow field: Definition of the potential flow problem

The fluid is assumed to be ideal, i.e. it is incompressible and inviscid. For an incompressible fluid the continuity equation reduces to

$$\nabla \cdot \vec{v} = 0 \tag{2.1}$$

where v is the velocity. This is valid for the present study since the flow velocities on a wind turbine are below 0.3 Ma. If the Reynolds number is high the viscous term in the *Navier-Stokes* equations becomes small, see Katz and Plotkin (2001, p. 17), and can be disregarded in the outer flow region. The *Navier-Stokes* equations reduce then to the *Euler* equation:

$$\frac{\partial \vec{v}}{\partial t} + \vec{v} \cdot \nabla \vec{v} = f - \frac{\nabla p}{\rho} \tag{2.2}$$

where ρ is the density and f the contribution of volume forces. Since incompressibility is assumed ($D\rho/Dt = 0$), the velocity and pressure can be solved using the *Euler* equation; further no thermodynamic considerations are required. The internal energy of an incompressible flow is

constant for all times (Karamcheti, 1980, pp. 188-189); hence an energy equation is not required.

The velocity field v is the sum of two velocities

$$\vec{v} = \vec{v}_{ind} + \vec{v}_{kin} \tag{2.3}$$

where v_{kin} is the kinematic velocity, being the vector sum of the freestream velocity and the motion of the airfoil. This velocity is known and its determination for the present case is given in section 2.1.2. The induced velocity v_{ind} is the disturbance due to the presence of the airfoil in the domain and it is the task of the presented method to calculate this velocity. Hence, in addition to the above two assumptions, a third is introduced: the condition of irrotationality of the velocity field, $\nabla \times v = 0$, allowing the problem to be treated as a potential flow. From a physical point of view this may be assumed since shear forces between fluid elements can be neglected and the flow is subsonic. This allows the introduction of a scalar velocity potential $v = \nabla\phi$. Inserting this expression into the continuity equation (2.1) yields:

$$\nabla^2\phi = 0 \tag{2.4}$$

which reduces the equations of motion to the *Laplace* equation. The *Laplace* equation is a linear, second-order partial differential equation and solutions can be obtained by the principle of superposition. Within the framework of potential theory the solution can be generated from a distribution of elementary flows. It can be shown, using Green's theorem, that the solution of the entire flow field V can be determined by finding a singularity distribution of sources and doublets placed on the surface S_B and the wake S_W. These distributions all fulfill the *Laplace* equation and the requirement that the disturbance due to the body vanishes at infinity. The reader is referred to the textbooks of Karamcheti (1980, pp. 344-348) or Katz and Plotkin (2001, pp. 44-48) for a more comprehensive treatment of potential flow. The surface is discretized in so-called panels on which the singularities are placed. Since the present case considers only an airfoil section these panels resemble straight lines on the surface of the airfoil. Since no discretization of the flow field is required the panel method is computationally efficient. For the present investigation the major limiting factor is computationally the coupling to an associated structural model.

The panel method implemented in the present study uses the formulation of Hess and Smith (1967). Their formulation places a constant source

strength and a constant vortex strength at each panel. Furthermore, the vortex strength is equal at each panel. The induced velocity is then

$$\vec{v}_{ind} = \int_{S_B} (\vec{v}_s \sigma_j + \vec{v}_v \tau) dS + \int_{S_w} \vec{v}_w \Gamma_m dS \tag{2.5}$$

where σ is the unknown source strength and τ the unknown vortex strength. The last term is the contribution of the shed wake. A distinction is made between a steady and an unsteady formulation of the induced velocity which will be clarified in section 2.1.3.

Both contributions of the velocity field will be deduced in the following sections. However, the solution of the unknown singularities is not yet unique. In the real flow the no-slip condition on the solid airfoil surface, must be imposed due to viscosity ($v = 0$ at the surface). However, since the viscosity has been neglected, this does not hold. Flow tangency at the surface must be maintained, i.e. $\vec{v} \cdot \vec{n} = 0$, which is known as the kinematic boundary condition. Finally, the empirical boundary condition known as the Kutta condition is incorporated in order to introduce lift effects into the model. Together, these boundary conditions allow the formulation of a system of equations which lead to a unique solution for the unknown singularities, as will be shown in section 2.1.4. In this context it should be mentioned that flow separation cannot be captured with this solution. Such effects are only accessible in the experimental investigation.

After the determination of the velocity at the airfoil surface the pressure distribution can be obtained via Bernoulli's equation (inviscid flow is assumed) and is presented in section 2.1.5.

2.1.2 Kinematic Velocity Field

The determination of v_{kin} follows an approach explained by Send (1992, 1995). The kinematic velocity is physically the fluid velocity which is encountered by the airfoil seen from the body-fixed frame of reference. A description in body coordinates has the advantage of independence of time for the normal vector of the surface and a uniform motion becomes stationary.

For the derivation of the velocity including the heaving and pitching motion the airfoil in Figure 2.2 is considered. The airfoil moves in an inertial frame of reference with basis N. The body-fixed frame of reference

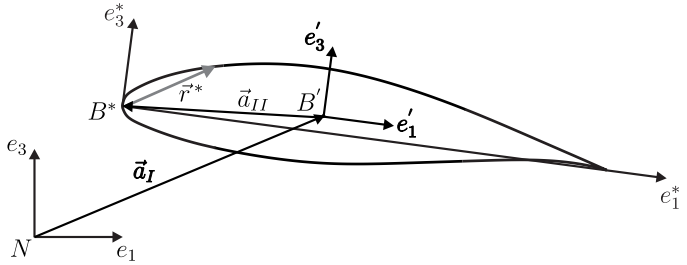

Figure 2.2: Inertial frame of reference N and body-fixed frames $B^*(\equiv$ leading-edge) and $B^{'}(\equiv$ main wing) for the definition of the relative heaving and pitching motion

$B^{'}$ designates the origin of the pitching motion. The motion of $B^{'}$ with respect to N is given by the vector $\vec{a}_I(t)$, including the translatory motion $g(t) = v_x t$ and the heaving motion $h(t)$:

$$\vec{a}_I(t) = (-g(t), 0, h(t)) \tag{2.6}$$

The minus sign indicates that the airfoil moves from right to left. The main body-fixed frame of the airfoil is the leading-edge frame B^* in which the airfoil coordinates are known. The vector $\vec{a}_{II}$ relates $B^{'}$ with respect to B^* and defines in this way the location of the pitch axes:

$$\vec{a}_{II} = \left(-x_p^*, 0, -z_p^*\right) \tag{2.7}$$

The motion of an arbitrary point on the airfoil surface can be described by the vector $\vec{r}^*(t) = (x^*, y^*, z^*)$ in terms of the leading-edge frame B^* or by $\vec{r}(t) = (x, y, z)$ with respect to N. Using the above relations the transformation, including a translation and rotation, between these frames is given by

$$\vec{r}(t) = \vec{a}_I(t) + (\vec{a}_{II} + \vec{r}^*(t) \cdot \mathbf{E}_E) \cdot \mathbf{E}_R\left(\alpha(t)\right) \tag{2.8}$$

and rearranging yields

$$\vec{r}^*(t) = \Big((\vec{r}(t) - \vec{a}_I(t)) \cdot \mathbf{E}_R^T(\alpha(t)) - \vec{a}_{II}\Big) \cdot \mathbf{E}_E^T \tag{2.9}$$

The matrix $\mathbf{E}_R$ defines the rotation about the pitch axes as a function of $\alpha(t)$:

$$\mathbf{E}_R(\alpha(t)) = \begin{pmatrix} \cos(\alpha(t)) & 0 & -\sin(\alpha(t)) \\ 0 & 1 & 0 \\ \sin(\alpha(t)) & 0 & \cos(\alpha(t)) \end{pmatrix} \tag{2.10}$$

The matrix $\mathbf{E}_E$ is the unit matrix since no rotation is carried out about the leading edge. Finally, the kinematic velocity can be obtained by differentiating Eq. 2.9 with respect to time

$$\frac{d\vec{r}^{\,*}}{dt} = \vec{v}^{\,*}_{kin}(t) = (\vec{r}(t) - \vec{a}_I(t)) \cdot \dot{\mathbf{E}}^T_R(\alpha(t)) - \dot{\vec{a}}_I(t) \cdot \mathbf{E}^T_R(\alpha(t)) \tag{2.11}$$

Further $\vec{r}(t)$ is substituted by Eq. 2.8 and one yields the kinematic velocity seen from the body-fixed frame of reference and in coordinates of the body-fixed frame of reference B^*. The complete differentiation is not given here as it was carried out with an algebraic computer tool.

The motion of the leading and trailing-edge flap is superimposed to the pitching and heaving motion of the airfoil. Therefore, two additional coordinate systems $B^{''}$ and $B^{'''}$ are introduced, see Figure 2.3. The origins are located at the flap hinge points. The position of the hinge points with respect to B^* are given by the vector

$$\vec{a}_{III} = (x^*_l, 0, z^*_l) \tag{2.12}$$

for the leading-edge flap and by the vector

$$\vec{a}_{IV} = (x^*_t, 0, z^*_t) \tag{2.13}$$

for the trailing-edge flap. The complete transformation from the inertial coordinate system via the system $B^{'}$ and B^* to the flap coordinate system $B^{''}$ is given by

$$\vec{r}(t) = \vec{a}_I(t) + \left(\vec{a}_{II} + \left(\vec{a}_{III} + \vec{r}^{\,''}(t) \cdot \mathbf{E}_R(\gamma(t))\right) \cdot \mathbf{E}_E\right) \cdot \mathbf{E}_R(\alpha(t)) \tag{2.14}$$

and rearranging yields

$$\vec{r}^{\,''}(t) = \left(\left((\vec{r}(t) - \vec{a}_I(t)) \cdot \mathbf{E}^T_R(\alpha(t)) - \vec{a}_{II}\right) \cdot \mathbf{E}^T_E - \vec{a}_{III}\right) \cdot \mathbf{E}^T_R(\gamma(t)) \tag{2.15}$$

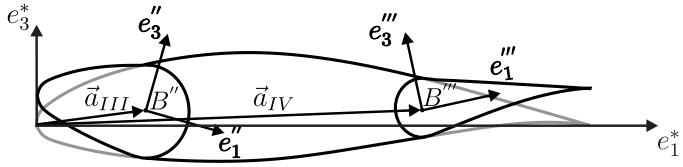

Figure 2.3: Body-fixed frames of reference B'' ($\equiv$ leading-edge flap) and B''' ($\equiv$ trailing-edge flap)for the definition of the flap motion

The angle $\gamma(t)$ describes the motion of the leading-edge flap. The above equations hold for the trailing-edge flap when the vector $\vec{a}_{III}$ is replaced by $\vec{a}_{IV}$ and the angle $\gamma(t)$ by the trailing-edge flap angle $\beta(t)$. The coupling between the leading and trailing-edge flap is given by $\beta(t) = -n\gamma(t)$. Kinematic nonlinearities are not considered since the examined flap angles are small. The kinematic velocity including the flap motion is again obtained by differentiation of Eq. 2.15 with respect to time, which is not given here explicitly. The coordinates of the airfoil surface seen from B'' are given by: $\vec{r}''(t) = \vec{r}^*(t) - \vec{a}_{III}$.

2.1.3 Induced Velocity Field

In this section the discretization of the surface integrals of Eq. 2.5 is presented. It is not the intention of this chapter to provide all equations necessary to implement the method. The current work uses the description of Cebeci et al. (2005) of the Hess-Smith panel method. They also provide an extension to the method to capture a time varying wake strength. Both methods are used in the present work. A further presentation of the panel method can be found in Moran (1984).

For the evaluation of the surface integral consider Figure. 2.4. The surface is discretized into n panels designated by a total of $n+1$ boundary points. The distribution is based on a cosine-transformation which ensures a higher resolution of the surface at the leading and trailing edge. In the center of each panel is the control point i. The counting of the coordinate points starts at the trailing edge, moves to the leading edge on the lower side and returns back to the trailing edge on the upper side. This order allows an efficient implementation and defines the body always to be on the right-hand side. In this sense the unit vector normal to the

surface, superscript n, points outwards of the airfoil. The tangential unit vector has superscript t. The inclination of the panel frame of reference to the x-axes is given by θ_i.

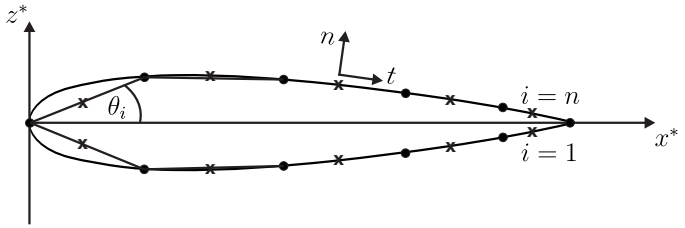

Figure 2.4: Discretization of airfoil surface S_B into a finite number of n panels with control points ($\equiv \times$) in the middle and $n+1$ panel borders ($\equiv \bullet$)

Contribution of airfoil

The presence of the airfoil can be considered as a disturbance which induces a velocity to the flow field. This induced velocity can be modeled by singularities. The Hess-Smith formulation places a potential source with constant strength and a potential vortex at each panel. At an arbitrary point P in space the induced velocity is calculated by the summation of all singularities:

$$v^n_{ind,i} = \sum_{j=1}^{n} A^n_{ij}\sigma_j + \tau \sum_{j=1}^{n} B^n_{ij} \tag{2.16}$$

$$v^t_{ind,i} = \sum_{j=1}^{n} A^t_{ij}\sigma_j + \tau \sum_{j=1}^{n} B^t_{ij} \tag{2.17}$$

where A^n_{ij}, A^t_{ij}, B^n_{ij} and B^t_{ij} are called the influence coefficients. The above equations state that at each control point i the induced velocity is the sum of the potentials placed at the panels j and itself ($i = j$). The velocities are evaluated in the panel coordinates in the normal and tangential direction separately. Hence, the influence coefficient include the geometric

relations between the desired control point and the respective singularity:

$$A_{ij}^{n} = \begin{cases} \dfrac{1}{2\pi}\left[\sin(\theta_i - \theta_j)\ln\dfrac{r_{i,j+1}}{r_{i,j}} + \cos(\theta_i - \theta_j)\beta_{i,j}\right] & i \neq j \\ \dfrac{1}{2} & i = j \end{cases} \tag{2.18}$$

$$A_{ij}^{t} = \begin{cases} \dfrac{1}{2\pi}\left[\sin(\theta_i - \theta_j)\beta_{i,j} - \cos(\theta_i - \theta_j)\ln\dfrac{r_{i,j+1}}{r_{i,j}}\right] & i \neq j \\ 0 & i = j \end{cases} \tag{2.19}$$

$$B_{ij}^{n} = -A_{ij}^{t} \tag{2.20}$$

$$B_{ij}^{t} = A_{ij}^{n} \tag{2.21}$$

where r is the distance between the points. All other geometric relations can be found in the aforementioned textbooks, but the underlying principle is the application of the Biot-Savart relation.

Contribution of wake

In a steady formulation the bound circulation around the airfoil is fixed by the Kutta condition. To satisfy Kelvin's theorem a starting vortex of opposite sign is shed into the wake but its influence is negligible since it is far downstream. If the circulation around the airfoil changes with time, vorticity is permanently shed into the wake. The sum of circulation in the wake is equal to the bound circulation. Furthermore, the shed vorticity induces velocities on the airfoil and effects the load on the airfoil. The wake can be represented by discrete vortices placed along the path of the trailing edge, see Figure 2.5. For a time stepping method this means in each time step a discrete vortex is shed into the wake. The currently shed vortex at the trailing edge has the strength Γ_w. This strength can be determined using Kelvin's theorem ($D\Gamma/Dt = 0$) and is equal to the difference between the bound circulation of the previous and the current time step: $\Gamma_w = \Gamma_{k-1} - \Gamma_k$. Including the contribution of the wake the

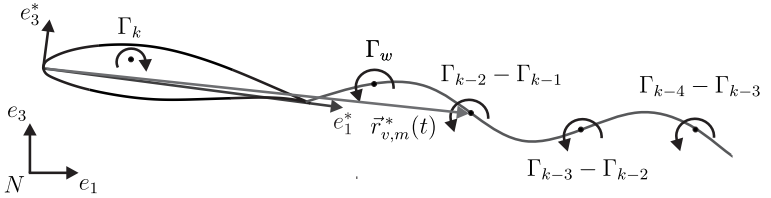

Figure 2.5: Discretization of wake behind airfoil with discrete vortex elements; the vortices are placed on the known trailing-edge path and are fixed with respect to the inertial frame of reference N;

induced velocity takes the following form:

$$\begin{aligned}(v^n_{ind,i})_k = &\sum_{j=1}^{n}(A^n_{ij})_k(\sigma_j)_k + \tau_k\sum_{j=1}^{n}(B^n_{ij})_k \\ &+ \sum_{m=1}^{k-1}(C^n_{im})_k(\Gamma_{m-1} - \Gamma_m) + (D^n_i)_k\Gamma_w\end{aligned} \tag{2.22}$$

$$\begin{aligned}(v^t_{ind,i})_k = &\underbrace{\sum_{j=1}^{n}(A^t_{ij})_k(\sigma_j)_k + \tau_k\sum_{j=1}^{n}(B^t_{ij})_k}_{airfoil} \\ &\underbrace{+ \sum_{m=1}^{k-1}(C^t_{im})_k(\Gamma_{m-1} - \Gamma_m) + (D^t_i)_k\Gamma_w}_{wake}\end{aligned} \tag{2.23}$$

The subscript k indicates the time step ($t_k(k = 1, 2, ...)$). However, the influence coefficients $(A^n_{ij})_k, (A^t_{ij})_k, (B^n_{ij})_k$ and $(B^t_{ij})_k$ are the same as in the steady case. The above equations demonstrate that the influence of the wake is divided into two parts. That is the contribution of the unknown vortex Γ_w incorporated by the influence coefficient $(D_{ij})_k$ and the known vortices Γ_m (subscript m) incorporated by the influence coefficient $(C_{im})_k$. Following Send (1995, p. 63) the wake is assumed to be fixed in the inertial frame of reference. Hence, no diffusion or distribution of vortices is considered. Nevertheless, since the panel method is formulated in the body frame of reference B^* the location of each shed vortex is

changing every time step with respect to B^*. The position vector of each known vortex is given by

$$\vec{r}^*_{v,m}(t) = (\vec{r}_{TE}(\Delta t \cdot m) - \vec{a}_I(t)) \cdot \mathbf{E}_I^T(\alpha(t)) + \vec{a}_{II} \tag{2.24}$$

where $\vec{r}_{TE}(t)$ is the path of the trailing edge in the inertial frame of reference (see Eq. 2.8 and 2.14) and $\vec{r}_{TE}(\Delta t \cdot m)$ the corresponding position of each vortex. The position of the currently shed vortex $\vec{r}^*_w(t)$ is also given by Eq. 2.24 when $\vec{r}_{TE}(\Delta t \cdot m)$ is substituted by $\vec{r}_{TE}(\Delta t \cdot k)$.

The influence coefficients for the known vortices inducing velocities perpendicular to the distance r between the vortex position (index v) and the collocation point (index c) can be written as

$$(C^n_{im})_k = -\frac{(z^*_{v,m})_k - z^*_{c,i}}{2\pi r^2} \cos\theta_i \tag{2.25}$$

$$(C^t_{im})_k = \frac{(x^*_{v,m})_k - x^*_{c,i}}{2\pi r^2} \sin\theta_i \tag{2.26}$$

and for the currently shed vortex

$$(D^n_i)_k = -\frac{(z^*_w)_k - z^*_{c,i}}{2\pi r^2} \cos\theta_i \tag{2.27}$$

$$(D^t_i)_k = \frac{(x^*_w)_k - x^*_{c,i}}{2\pi r^2} \sin\theta_i \tag{2.28}$$

The above equations state furthermore that the wake discretization is a function of the trailing edge velocity and the time step. This results in a discretization error, see Katz and Plotkin (2001, p. 390).

2.1.4 Boundary Conditions

The previous two chapters have shown how the kinematic and induced velocities can be determined. Now the aforementioned boundary conditions are used to derive a system of equation which solves the flow problem uniquely, i.e. to calculate the unknown velocity potentials. Since the normal velocity on the airfoil surface has to vanish, Eq. 2.3 becomes

$$\vec{v}_{ind,i} \cdot \vec{n} = -\vec{v}_{kin,i} \cdot \vec{n} \tag{2.29}$$

which leads to the following equation after inserting Eq. 2.16

$$\sum_{j=1}^{n} A_{ij}^{n} \sigma_j + \sum_{j=1}^{n} B_{ij}^{n} \tau_j = -v_{kin,i}^{n} \tag{2.30}$$

Eq. 2.30 provides n equations. The $n+1th$ equation is given by the Kutta condition. In the present work this is simply ensured by assuming that the tangential velocities at the first and last panel (i.e. the trailing edge) are identical:

$$-v_1^t = v_n^t \tag{2.31}$$

The minus sign is related to the formulation in the panel coordinate system. Similarly, inserting the formulation of the induced velocity Eq. 2.17 yields

$$\sum_{j=1}^{n} \left(A_{1j}^{t} + A_{nj}^{t}\right) \cdot \sigma_j + \tau \sum_{j=1}^{n} \left(B_{1j}^{t} + B_{nj}^{t}\right) = -v_{kin,1}^{t} - v_{kin,n}^{t} \tag{2.32}$$

Eq. 2.30 and 2.32 can be written in matrix form to

$$\begin{pmatrix} a_{11} & a_{12} & \cdots & a_{1n} & b_{1,n+1} \\ a_{21} & a_{22} & \cdots & a_{2n} & b_{2,n+1} \\ \vdots & \vdots & \ddots & \vdots & \vdots \\ a_{n1} & a_{n2} & \cdots & a_{nn} & b_{n,n+1} \\ a_{n+1,1} & a_{n+1,2} & \cdots & a_{n+1,n} & b_{n+1,n+1} \end{pmatrix} \begin{pmatrix} \sigma_1 \\ \sigma_2 \\ \vdots \\ \sigma_n \\ \tau \end{pmatrix} = \begin{pmatrix} \mathrm{RHS}_1 \\ \mathrm{RHS}_2 \\ \vdots \\ \mathrm{RHS}_n \\ \mathrm{RHS}_{n+1} \end{pmatrix}$$

where the entries are given by:

$$a_{ij} = A_{ij}^{n} \tag{2.33}$$

$$b_{i,n+1} = \sum_{j=1}^{n} B_{ij}^{n} \tag{2.34}$$

$$a_{n+1,j} = A_{1j}^{t} + A_{nj}^{t} \tag{2.35}$$

$$b_{n+1,n+1} = \sum_{j=1}^{n} \left(B_{1j}^{t} + B_{nj}^{t}\right) \tag{2.36}$$

$$\mathrm{RHS}_i = -v_{kin,i}^{n} \tag{2.37}$$

$$\mathrm{RHS}_{n+1} = -v_{kin,i}^{t} - v_{kin,n}^{t} \tag{2.38}$$

In the unsteady case two things change. Due to the additional unknown vortex strength Γ_W a $n+2th$ equation is needed to solve the problem. This equation is provided by the Kelvin theorem in the form

$$\Gamma_w = \Gamma_{k-1} - \Gamma_k \tag{2.39}$$

Furthermore, an unsteady Kutta condition is introduced, by equalizing the pressure at the trailing edge. According to the unsteady Bernoulli equation which includes the change of the velocity potential one obtaines:

$$(v_1^t)_k^2 - (v_n^t)_k^2 = 2\left[\frac{\delta(\Phi_n - \Phi_1)}{\delta t}\right]_k = 2\left(\frac{\delta\Gamma}{\delta t}\right)_k \tag{2.40}$$

which can be approximated by finite differences

$$(v_1^t)_k^2 - (v_n^t)_k^2 = 2\frac{\Gamma_k - \Gamma_{k-1}}{t_k - t_{k-1}} = 2s\frac{\tau_k - \tau_{k-1}}{t_k - t_{k-1}} \tag{2.41}$$

where s is the surface length of the airfoil. The system of equations turns into the following matrix form. The $n+1th$ row is due to the unsteady Kutta condition inversely dependent on the vortex strength, which requires an implicit solution scheme.

$$\begin{pmatrix} a_{11} & a_{12} & \cdots & a_{1n} & b_{1,n+1} & d_1 \\ a_{21} & a_{22} & \cdots & a_{2n} & b_{2,n+1} & d_2 \\ \vdots & \vdots & \ddots & \vdots & \vdots & \vdots \\ a_{n1} & a_{n2} & \cdots & a_{nn} & b_{n,n+1} & d_n \\ 0 & 0 & \cdots & 0 & 0 & 0 \\ 0 & 0 & \cdots & 0 & s & 1 \end{pmatrix} \begin{pmatrix} (\sigma_1)_k \\ (\sigma_2)_k \\ \vdots \\ (\sigma_n)_k \\ \tau_k \\ (\Gamma_w)_k \end{pmatrix} = \begin{pmatrix} \mathrm{RHS}_1 \\ \mathrm{RHS}_2 \\ \vdots \\ \mathrm{RHS}_n \\ \mathrm{RHS}_{n+1} \\ \mathrm{RHS}_{n+2} \end{pmatrix}$$

The right-hand side is given by:

$$\mathrm{RHS_i} \quad = (-v_{kin,i}^n)_k - \sum_{m=1}^{k-1} (C_{im})_k (\Gamma_{m-1} - \Gamma_m) \tag{2.42}$$

$$\mathrm{RHS_{n+2}} = \Gamma_{k-1} \tag{2.43}$$

$$\mathrm{RHS_{n+1}} = \left[\sum_{j=1}^{n}(A^t_{1j})_k(\sigma_j)_k + \tau_k\sum_{j=1}^{n}(B^t_{1j})_k + \right.$$
$$\left.\sum_{m=1}^{k-1}(C^t_{1,m})_k(\Gamma_{m-1}-\Gamma_m) + (D^t_1)_k(\Gamma_w)_k + v^t_{kin,1}\right]^2$$
$$-\left[\sum_{j=1}^{n}(A^t_{nj})_k(\sigma_j)_k + \tau_k\sum_{j=1}^{n}(B^t_{nj})_k + \right.$$
$$\left.\sum_{m=1}^{k-1}(C^t_{n,m})_k(\Gamma_{m-1}-\Gamma_m) + (D^t_n)_k(\Gamma_w)_k + v^t_{kin,n}\right]^2$$
$$-2s\frac{\tau_k-\tau_{k-1}}{t_k-t_{k-1}} \quad (2.44)$$

2.1.5 Computation of Pressure

After the unknown singularities are determined via the panel method the velocity field, especially at the airfoil surface, can be calculated by Eq. 2.3. To obtain the pressure field the *Euler* equation is integrated, leading to the Bernoulli equation. In a potential flow field the Bernoulli constant has the same value in the entire field and between any two points, except for singularity points. The reader is referred to the corresponding literature for a comprehensive derivation, e.g. Spurk and Aksel (2006, pp. 116-119).

In the steady case the pressure coefficient at each panel reduces to

$$c_{p,i} = 1 - \left(\frac{v_i^t}{v_\infty} \right)^2 \tag{2.45}$$

The force coefficients are calculated by integrating the pressure over the airfoil surface. For the unsteady case one needs to consider the temporal derivative of the velocity potential. The unsteady Bernoulli equation yields:

$$(c_{p,i})_k = \left(\frac{v_{kin,i}}{v_\infty} \right)^2 - \left(\frac{(v_i^t)_k}{v_\infty} \right)^2 - 2\frac{(\Phi_i)_k - (\Phi_i)_{k-1}}{t_k - t_{k-1}} \tag{2.46}$$

The velocity potential is determined via an integration of the velocity along a streamline, see Figure 2.6. Since the airfoil surface is considered to be a streamline the integration starts upstream at infinity to the stagnation point. Because the differences of the potential are needed it is

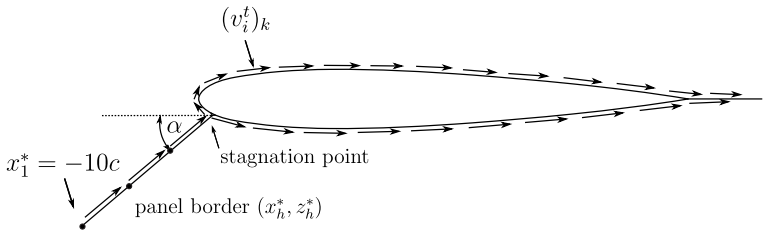

Figure 2.6: Tangential velocity along stream line

sufficient to use the velocity potentials of the disturbance. The strength of the disturbance decays at $1/r$ from the airfoil. Cebeci et al. (2005)

suggest to start the integration $10c/\cos(\alpha)$ upstream. This procedure requires again a discretization of the streamline into z panels, indicated by the index h. Hence, the potential at the stagnation point (index St) is

$$(\Phi_{St})_k = \sum_{h=1}^{z} (v_h^t)_k \left[(x_{h+1}^* - x_h^*)^2 + (z_{h+1}^* - z_h^*)^2 \right]^{\frac{1}{2}} \tag{2.47}$$

To obtain the total potential one needs to distinguish between the upper and lower side of the airfoil as all velocities have to be summed up by their positive values. The velocities change their sign at the stagnation point due to the direction of the tangential unit vector of the panel coordinate system. Incorporating this distinction of cases one yields:

$$(\Phi_i)_k = \begin{cases} (\Phi_{St})_k + \sum_{j=i_{St}}^{i-1} (v_j)_k \left[(x_{j+1}^* - x_j^*)^2 + (z_{j+1}^* - z_j^*)^2 \right]^{\frac{1}{2}} \\ \qquad\qquad\qquad\qquad \text{for} \quad i_{St} \leq i \leq n \\ (\Phi_{St})_k + \sum_{j=i}^{i_{St}-1} \|(v_j)_k\| \left[(x_{j+1}^* - x_j^*)^2 + (z_{j+1}^* - z_j^*)^2 \right]^{\frac{1}{2}} \\ \qquad\qquad\qquad\qquad \text{for} \quad 1 \leq i < i_{St} \end{cases} \tag{2.48}$$

2.2 Structural Model

This section describes the structural model to investigate the concept of an airfoil with adaptive camber. It was stated in the introduction that one of the key criteria for this study is to limit the number of structural degrees of freedom. Therefore, the airfoil with flaps is composed of rigid bodies which are elastically coupled to each other. Several cases can now be defined which lead to a certain number of degrees of freedom. The airfoil with flaps comprises of three bodies, see Figure 2.7: the main wing ($\equiv$ body C), the leading-edge flap ($\equiv$ body B) and the trailing-edge flap ($\equiv$ body D). The first case considers only the flap motion. The rotation of both flaps around a hinge point at the main wing is reduced to one generalized coordinate q_3. The main wing is fixed with respect to the

inertial frame of reference. This motion is called the 1DOF case. The counterpart of this case is the rigid wing. The experimental investigation considers also this case. The main goal of the concept is to reduce the fatigue loads of the rotor blade. This requires that the bending flexibility of the wing is also captured. This is introduced by the suspension of the main wing to a translatory spring with the corresponding degree of freedom q_1. Additionally a torsional spring represents the torsional stiffness of the main wing and is related to q_2. The case including the elastically mounted wing with flap motion is called the 3DOF case. For a later comparison, and for estimating the overall benefit in terms of load alleviation this case is compared to the so-called 2DOF case, wich includes solely the bending and torsional degrees of freedom of the main wing. Further, the consideration of both the bending and torsional flexibility is unavoidable when one wants to perform a stability analysis, see Försching (1974, pp. 482-490). An edgewise degree of freedom (translatory oscillation in chord direction) is not considered at the present stage, since Bergami and Gaunaa (2010) have investigated the influence of this degree of freedom on the flutter limit for a symmetric airfoil and found that it has no influence. Even for cambered airfoils this degree of freedom has no influence if a realistic amount of structural damping is applied. However, edgewise oscillations of the blades have a significant contribution to the fatigue loads but are due to gravitation.

The equations of motion are obtained from the principle of virtual work using the code AUTOLEV based on Kane's algorithm, see Kane and Levinson (1985). The advantage of the algorithm is that constraint forces do not have to be considered in the derivation of the equations of motion. Furthermore, the method is more effective than the use of Lagrange's equations of second kind since less symbolic differentiations have to be carried out.

For the convenience of the reader the linearized equations of motion are given in the form

$$\mathbf{M}\,\ddot{\vec{\mathbf{q}}}(t) + \mathbf{D}\,\dot{\vec{\mathbf{q}}}(t) + \mathbf{K}\,\vec{\mathbf{q}}(t) = \mathbf{F}(t, q, \dot{q}) \tag{2.49}$$

for the above three cases in the next sections. Since the equations of motion for the 1 and 2 DOF case are obtained by constraining respective degrees of freedom, the description begins with the most general 3 DOF case.

2.2.1 3DOF - Heaving, Pitching and Flap Motion

According to Figure 2.7 the main wing (≡ body C) has a mass m_f and a moment of inertia θ_f. The bending stiffness k_h corresponds to q_1. The torsional stiffness k_θ corresponds to q_2. The leading and the trailing-edge flap are modeled by bodies B and D which have been tilted with respect to C. The tilting angles are coupled through a mechanism which is represented by the constraint n. Between body B and C there is a torsional spring (stiffness k_γ) and between C and D there is a torsional damper (constant d_γ). The mass and moment of inertia of the flaps are m_l, θ_l, m_t and θ_t. On each body the resultant aerodynamic forces and moment obtained from the panel method are applied at the center of gravity.

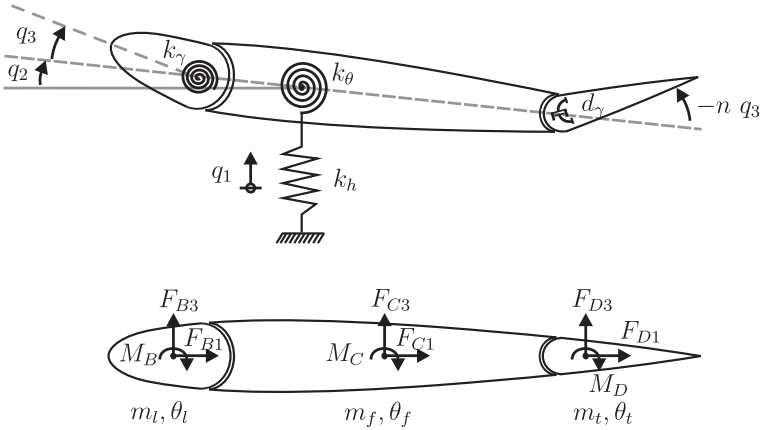

Figure 2.7: Structural model of the 3DOF case; aerodynamic moments and forces applied at the center of gravity of each body

In contradiction to the aerodynamic model the structural model is formulated with respect to the elastic axis. The rotation points of the flaps are defined by x_l, z_l and x_t, z_t, see Figure 2.8. The location of the center of gravity is given by the distance s in the x and z-direction for each

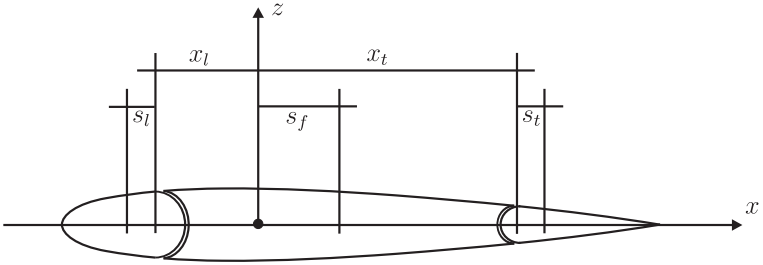

Figure 2.8: Location of the flap hinge points and center of gravities of each body with respect to the elastic axes exemplarily for a symmetric airfoil; For unsymmetric airfoils a z-component is present, which requires an additional subscript, see equations of motion;

body. In accordance to Eq. 2.49 the mass matrix reads

$$\begin{bmatrix} m_f + m_l \\ +m_t \end{bmatrix} \quad \begin{bmatrix} m_l(s_{lx} + x_l) - m_f s_{fx} \\ -m_t(s_{tx} + x_t) \end{bmatrix} \quad \begin{bmatrix} m_l s_{lx} \\ +n m_t s_{tx} \end{bmatrix}$$

$$\begin{bmatrix} m_l(s_{lx} + x_l) \\ -m_f s_{fx} \\ -m_t(s_{tx} + x_t) \end{bmatrix} \quad \begin{bmatrix} m_l(s_{lx}^2 + s_{lz}^2 + x_l^2 \\ +z_l^2 + 2s_{lx}x_l + 2s_{lz}z_l) \\ +m_t(s_{tx}^2 + s_{tz}^2 + x_t^2 \\ +z_t^2 + 2s_{tx}x_t + 2s_{tz}z_t) \\ m_f(s_{fx}^2 + s_{fz}^2) \\ +\theta_l + \theta_f + \theta_t \end{bmatrix} \quad \begin{bmatrix} +m_l(s_{lx}x_l + s_{lx}^2 \\ +s_{lz}z_l + s_{lz}^2) \\ -n m_t(s_{tx}x_t + s_{tx}^2 \\ +s_{tz}z_t + s_{tz}^2) \\ \theta_l - \theta_t n \end{bmatrix}$$

$$\begin{bmatrix} m_l s_{lx} \\ +n m_t s_{tx} \end{bmatrix} \quad \begin{bmatrix} m_l(s_{lx}x_l + s_{lx}^2 \\ +s_{lz}z_l + s_{lz}^2) \\ -n m_t(s_{tx}x_t + s_{tx}^2 \\ +s_{tz}z_t + s_{tz}^2) \\ \theta_l - \theta_t n \end{bmatrix} \quad \begin{bmatrix} m_l(s_{lx}^2 + s_{lz}^2) \\ +m_t n^2(s_{tx}^2 + s_{tz}^2) \\ +\theta_l + \theta_t n^2 \end{bmatrix}$$

the damping matrix includes

$$\mathbf{D} = \begin{bmatrix} d_h & 0 & 0 \\ 0 & d_\theta & 0 \\ 0 & 0 & d_\beta n^2 \end{bmatrix} \tag{2.50}$$

the stiffness matrix becomes

$$\mathbf{K} = \begin{bmatrix} k_h & 0 & 0 \\ 0 & k_\theta & 0 \\ 0 & 0 & k_\gamma \end{bmatrix} \tag{2.51}$$

and the force vector on the right-hand side is given by

$$\mathbf{F} = \begin{bmatrix} F_{B3} + F_{C3} + F_{D3} \\ M_B + M_C + M_D + (s_{lz} + z_l)F_{B1} + (s_{lx} + x_l)F_{B3} \\ +s_{fz}F_{C1} - s_{fx}F_{C3} + (s_{tz} + z_t)F_{D1} - (s_{tx} + x_t)F_{D3} \\ M_B + s_{lx}F_{B3} + s_{lz}F_{B1} + n(s_{tx}F_{D3} - s_{tz}F_{D1}) - nM_D \end{bmatrix} \tag{2.52}$$

2.2.2 2DOF - Heaving and Pitching Motion

The equation of motion for the heaving and pitching motion of the airfoil without flaps are obtained by constraining the flap degree of freedom, i.e. $q_3 = \dot{q_3} = 0$. The mass matrix reduces to

$$\begin{bmatrix} m_f + m_l + m_t & m_l(s_{lx} + x_l) - m_f s_{fx} \\ & -m_t(s_{tx} + x_t) \\ m_l(s_{lx} + x_l) - m_f s_{fx} & m_l(s_{lx}^2 + s_{lz}^2 + x_l^2 + z_l^2 + 2s_{lx}x_l + 2s_{lz}z_l) \\ -m_t(s_{tx} + x_t) & +m_t(s_{tx}^2 + s_{tz}^2 + x_t^2 + z_t^2 + 2s_{tx}x_t + 2s_{tz}z_t) \\ & m_f(s_{fx}^2 + s_{fz}^2) + \theta_l + \theta_f + \theta_t \end{bmatrix}$$

the damping matrix includes

$$\mathbf{D} = \begin{bmatrix} d_h & 0 \\ 0 & d_\theta \end{bmatrix} \tag{2.53}$$

the stiffness matrix becomes

$$\mathbf{K} = \begin{bmatrix} k_h & 0 \\ 0 & k_\theta \end{bmatrix} \tag{2.54}$$

and the force vector on the right-hand side is given by

$$\mathbf{F} = \begin{bmatrix} F_{B3} + F_{C3} + F_{D3} \\ M_B + M_C + M_D + (s_{lz} + z_l)F_{B1} + (s_{lx} + x_l)F_{B3} \\ +s_{fz}F_{C1} - s_{fx}F_{C3} + (s_{tz} + z_t)F_{D1} - (s_{tx} + x_t)F_{D3} \end{bmatrix} \tag{2.55}$$

2.2.3 1DOF - Flap Motion

A very important degree of freedom in the present study is the flap motion. After constraining the heaving and pitching motion, $q_{1,2} = \dot{q}_{1,2} = 0$, the following equation of motion results:

$$\begin{aligned}(\theta_l + \theta_t n^2 + m_l(s_{lx}^2 + s_{lz}^2) + m_t n^2(s_{tx}^2 + s_{tz}^2))\,\ddot{q_3}(t) \\ + d_\beta n^2\,\dot{q_3}(t) + k_\gamma\,q_3(t) = \\ M_B + s_{lx}F_{B3} + s_{lz}F_{B1} + n(s_{tx}F_{D3} - s_{tz}F_{D1}) - nM_D \end{aligned} \quad (2.56)$$

One significant issue of the present concept can be seen in the last two terms of the right-hand side. The moment and forces on the trailing-edge flap are multiplied by the coupling ratio n. This means a gear box is effectively realized.

2.3 Implementation

All models have been implemented in Matlab. The steady panel method has been verified with XFoil, the unsteady formulation with the model of Gaunaa (2010) which can be found in Appendix A. The derivation of the position vector to deduce the kinematic velocity has been carried out with the algebraic programm REDUCE.

The nonlinear equations of motion are given analytically by AUTOLEV, an ODE-solver provided by Matlab is used to integrate the differential equations. The structural states q_1, q_2, q_3 and the corresponding velocities u_1, u_2, u_3 are passed to the aerodynamic model, where the resulting velocity on the airfoil surface is calculated; the pressure distribution is then available through Bernoulli's equation. This distribution is integrated over the three bodies (flaps and main wing) and the resultant forces and moments are computed. Hence, a two-way fluid-structure interaction is effectively being implemented. It should be noted that $q_1 \equiv h$, $q_2 \equiv \alpha$ and $q_3 \equiv \gamma$. This dual nomenclature is preserved to maintain convention in both the aerodynamical and structural perspective.

2.4 RANS Computations

As stated earlier the potential flow calculation does not consider any viscous effects. To investigate the validity of this assumption additional simulations were performed using a RANS approach implemented in the commercial CFD Sofware ANSYS CFX. This chapter describes the governing equations as well the solver settings and typology of the developed grid. The RANS calculations are used to investigate the effect of the Reynolds number along with XFoil[1] computations. Furthermore, two different domain sizes allow the investigation of blockage effects within the wind tunnel experiment.

The momentum transport is now described by the unsteady Reynolds-Averaged Navier Stokes equation and is given here in differential form:

$$\bar{\rho}\left(\frac{\partial \bar{u}_j}{\partial t} + \bar{u}_i \frac{\partial \bar{u}_j}{\partial x_i}\right) = -\frac{\partial \bar{p}}{\partial \bar{x}_j} + \frac{\partial}{\partial x_i}\left(\mu \frac{\partial \bar{u}_j}{\partial x_i} - \bar{\rho}\overline{u_i' u_j'}\right) \tag{2.57}$$

The Reynolds stress term is given by the *Boussinesq* approximation which assumes that the stresses of the turbulent fluctuations are physically analog to the stresses resulting from the molecular viscosity:

$$\bar{\rho}\overline{u_i' u_j'} = -\bar{\rho}\nu_T\left(\frac{\partial \bar{u}_j}{\partial \bar{x}_i} + \frac{\partial \bar{u}_i}{\partial \bar{x}_j}\right) + \frac{2}{3}\bar{\rho}k\delta_{ij} \tag{2.58}$$

where ν_T is the turbulent viscosity. The turbulent viscosity is obtained using the $k-\omega$ SST Model developed by Menter (1994). This model uses the Wilcox $k-\omega$ model in the logarithmic region of the boundary layer and the $k-\epsilon$ model in a transformed $k-\omega$ formulation in the outer region of the boundary layer and in the freestream. The shift is achieved through a blending function. This model is then extended to account for the shear stress transport (SST) and leads to a better prediction of the onset of separated flow regions. This is realized by introducing a second blending function. Thereby the definition of the eddy-viscosity is changed, dependent on the pressure gradient seen by the boundary layer.

2.4.1 Solver Settings

ANSYS-CFX 12.0 uses a finite-volume discretization of the domain to obtain the flow field. The spatial derivatives are discretized via so-called

[1] XFoil V. 6.96, M. Drela (MIT)

High Resolution Schemes. These are Upwind Difference Schemes with a second-order accuracy. The transient terms are discretized using a Second Order Backward Euler Scheme. These Schemes are well explained in the book of Lecheler (2009). The convergence criteria was set to RMS = 10^{-5}.

2.4.2 Domain and Grid

Two different domains were constructed. One domain (Figure 2.10) with a height corresponding to the width of the low-speed wind tunnel, $h = 2.9\,\text{m}$. The size upstream and downstream of the airfoil were determined by comparisons of the local velocity to the freestream velocity at the inlet and outlet. The size of the domain in terms of the chord length c is plotted. The depth b in spanwise direction is 0.01 m. This direction is discretized by one volume element. The angle of attack is adjusted by a rotation of the airfoil. At the lower and upper walls the free-slip condition is applied. For a quantification of the blockage effect in the tunnel the second domain (Figure 2.9) ensures the freeflow condition. The wall boundaries were treated as openings which allow in and out flows. The height of $30c$ was also determined by a comparison of the velocity difference at the boundaries, see Appendix B.

The meshes were generated with the software ICEM CFD. Block-structured grids were used to increase the mesh quality and to allow a controlled refinement of critical flow regions. Based on a suggestion of Aghajari (2009), a c-grid topology was used around the airfoil, allowing for good resolution of the boundary layer and the near wake. The boundary layer was resolved to have all advantages of the $k-\omega$ SST Model. To ensure a dimensionless wall distance $y^+ \leq 1$, the height of the first grid cell is $\delta = 10^{-5}\,\text{m}$. A reduction of cells is achieved by a second c-grid in the opposite direction, which expands the cell density in the near wake to a lower resolution in the far wake. The mesh resolution around the airfoil is identical for both grids. A total number of 24 blocks (Figure 2.11) for the freeflow and 16 blocks (Figure 2.12) for the tunnel grid were used. A grid-independence study was performed using Richardson extrapolation, see Schäfer (1999). The obtained lift coefficient for the tunnel mesh of 119280 hexaeder elements showed a difference to the extrapolated solution of 1.33%. The lift coefficient for the freeflow mesh with 194544 hexaeder elements differed 0.69% to the extrapolated value. All simulations were performed with these grids.

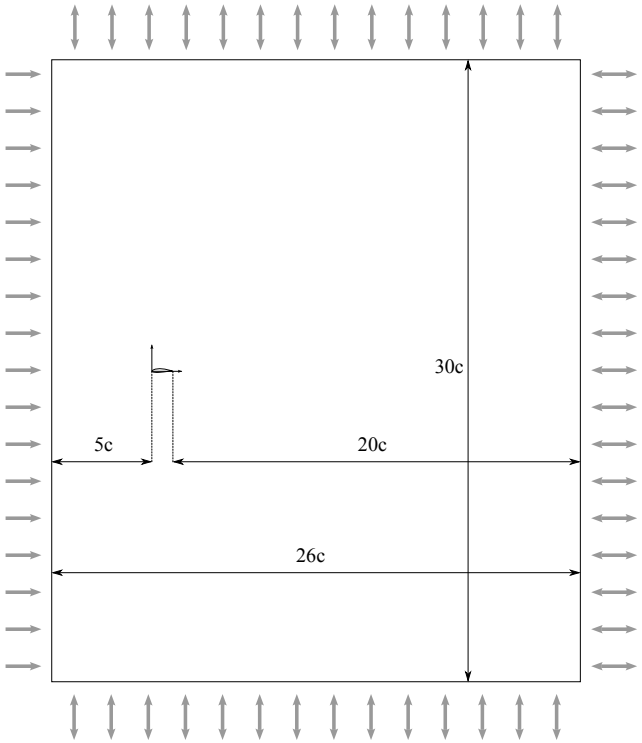

Figure 2.9: Sketch of freeflow domain, boundary conditions and size in terms of the chord length c

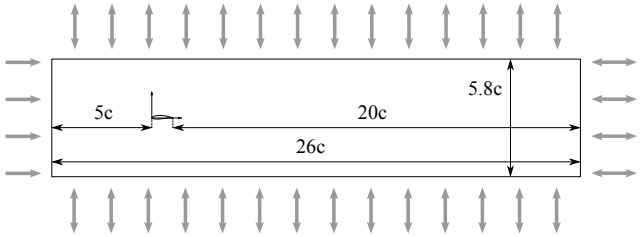

Figure 2.10: Sketch of tunnel flow domain, boundary conditions and size in terms of the chord length c

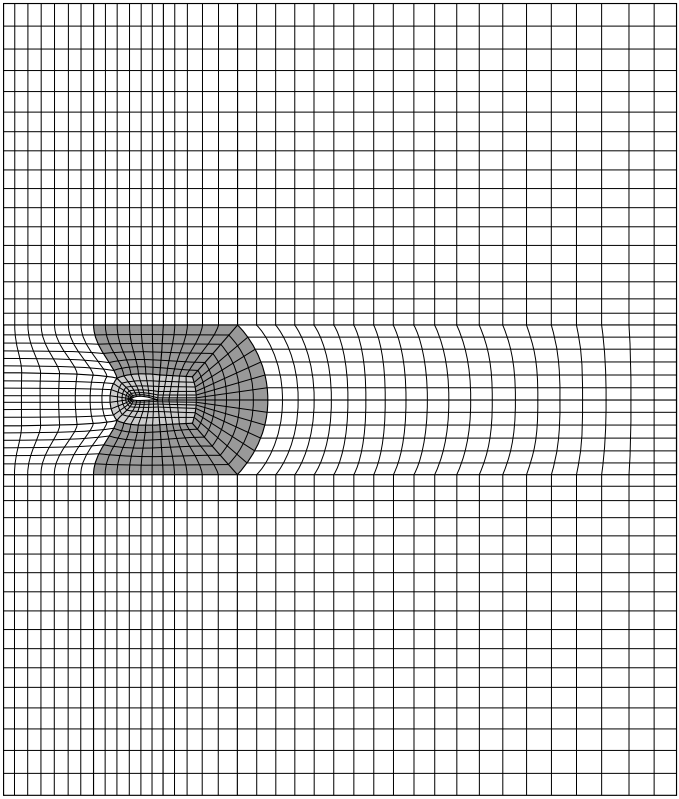

Figure 2.11: Double c-grid with 24 blocks allowing freeflow condition

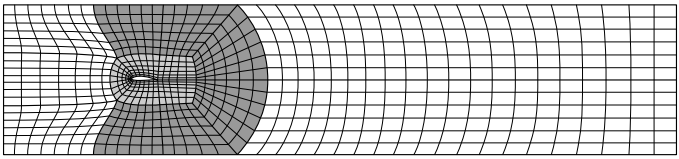

Figure 2.12: Double c-grid with 16 blocks; height of mesh corresponds to the width of the wind tunnel

Chapter 3

Experimental Setup

The concept of a load-dependent airfoil camber was investigated experimentally under quasi-steady conditions. This chapter describes the experimental setup, including the final design and the measurement techniques. The final design of the wing was obtained by a parametric study using the numerical models of the previous chapter. The 1DOF case was realized, which enables only the motion of the flap and keeps the remaining wing rigid. The results of the parametric study will be presented in chapter 4.

This chapter further introduces the measurement techniques, including an estimation of the standard uncertainty of the measured quantities. The post-processing methods are discussed and finally a total standard uncertainty for the respective coefficients is calculated.

3.1 Wind Tunnel

The large scale low-speed wind tunnel at TU Darmstadt is a Göttinger-type tunnel with a vertical arrangement, as pictured in the Figure 3.1. The closed test section has a length of 4.8 m and a cross section of 2.2 m by 2.9 m. The 6-bladed fan is 3.8 m in diameter and is driven by a 300 kW direct-current motor, which allows wind speeds up to 68 m/s. The turbulence level is approximately 0.2% at test speeds above 20 m/s.

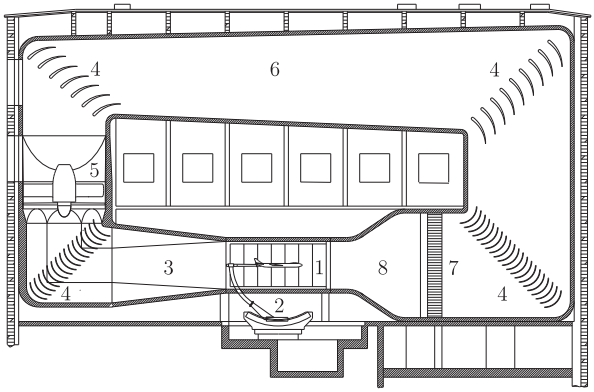

Figure 3.1: Large scale wind tunnel: 1. Test Section 2. Support 3. Diffusor 4. Guide Vane 5. Fan 6. Main Diffusor 7. Screen 8. Nozzle

3.2 Experimental Wing

The complete experimental set up can be seen in Figure 3.2. The wing is placed vertically in the test section, i.e lift is generated in horizontal direction. The air flow is from right to left in this picture. The main wing is mounted via a flange to the external balance that is underneath the test section. The entire balance is linked to a support table which allows rotation of the wing and adjusts the angle of attack. The mechanical construction is displayed in Figure 3.3. The main design criteria was to minimize any unwanted deflections which might influence the measurement. To ensure sufficient high bending stiffness two steel spars form the middle part of the wing. The deflection of these spars was estimated by a simple cantilever beam model. The maximum load of 700 N was assumed, which leads to a maximum tip deflection of 1 mm. The twist of the beams due to torsion was calculated to be 0.03°. The two spars are positioned and fixed with four aluminium fins. The outer contour of the fins is given by the airfoil shape. The holes in the fins are for sensor cables.

The rotational axes of each flap consists of a steel tube. At four discrete points load-bearing supports are installed on the spars. Inside the tube a holder is inserted wich links the tube to the bearing. That means the

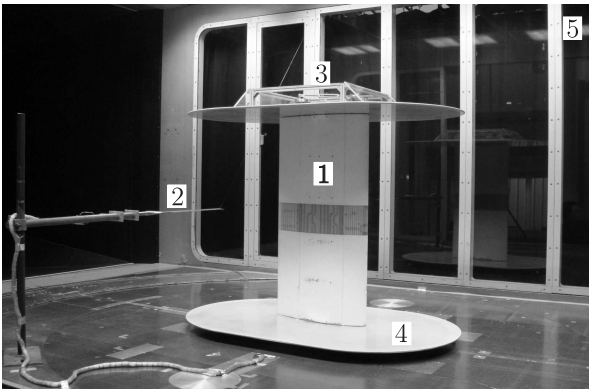

Figure 3.2: Wing in wind tunnel, flow from right to left: 1. Suction side: pressure measurement at half span 2. Wake rake 3. Coupling mechanic 4. Endplates 5. Location of Prandtl tube

flap motion is defined by four rotation points. The flaps and the surface of the middle wing section are made of fiberglass.

The chosen airfoil is a NACA 64_3618. The chord length c is 0.5 m and the span b is 1 m. Since a two-dimensional flow around the airfoil is desired, endplates are mounted on the wing tips. The size of each plate is 1.4 m by 0.9 m, which follows the rule of thumb $3c$ by $2c$. The distance

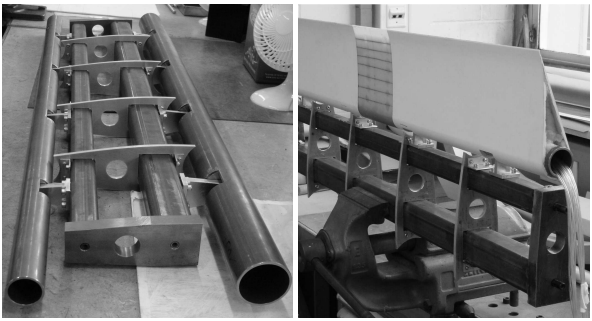

Figure 3.3: Left: Mechanical construction of the main wing; Right: Trailing-edge flap mounted to aft spar;

between the lower endplate and the tunnel floor is 50 mm. This keeps the wing outside the boundary layer of the test section.

The steel tubes of each flap go through the upper endplate, where the entire coupling mechanism is installed, as shown in Figure 3.4. At the end of the tube a circular adapter part is mounted. This part is surrounded by a magnetic strip, which provides an incremental signal for the angular sensor of each flap. The two moment sensors are placed on top of the adapter part. The sensors specification will follow in the next section. The two flaps are coupled through a rod and lever. The rod can be fixed at five positions on the lever, i.e. five coupling ratios n can be adjusted. The deflection of the trailing-edge flap is n times higher than the leading-edge flap. The moment around the trailing-edge hinge point is transferred with a factor of n to the leading-edge hinge point. This is an important factor for the static moment balance as will be discussed in section 5.3.4. The deflection of the leading-edge lever is limited by two stoppers. These stoppers are also used to fix the flaps in the original airfoil position. This case is called the rigid airfoil and defines the baseline measurements. At the end of the lever (r =180 mm) a spring is mounted which applies the preload moment to the leading edge. It was found that the nonlinearities in the angles due to the kinematic in the coupling mechanism can be neglected for the considered angle ranges.

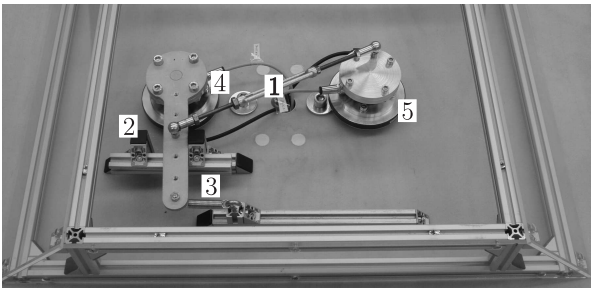

Figure 3.4: Top view on coupling mechanism: 1. Rod and lever 2. Stopper 3. Spring 4. Moment sensor 5. Angle sensor

3.3 Measurement Technique

In this section the measurement techniques are introduced. For all measured quantities the standard uncertainty is calculated according to the rules of GUM Type B. These uncertainties are the baseline for the calculation of the uncertainty of the post-processed quantities introduced in the next section.

The sampling frequency of the measurements is 2 Hz. This is mainly limited by the long pressure tubes. From the sampled values an average value of 10 measurements and the corresponding standard deviation are stored. Since it is intended to characterize the quasi-steady behavior of the airfoil the averaged measurement was taken for each angle of attack when the standard deviation of the surface pressure had stabilized at a low level. This was only possible in the attached flow regime.

3.3.1 Wind Tunnel Data

The wind tunnel provides several data which are measured simultaneously and stored. Some parameters are used later for the calculation of the derivatives. The wind tunnel velocity is adjusted by the nozzle pressure difference. This gives the freestream dynamic pressure q_∞. The standard uncertainty is given by

$$\sigma_{q_\infty} = \pm 5.46\,\mathrm{Pa} \tag{3.1}$$

The standard uncertainty of the angle of attack α corresponding to the angle sensor of the tunnel support is

$$\sigma_\alpha = \pm 0.0013^\circ \tag{3.2}$$

3.3.2 6-Component Balance

The integral forces and moments on the model are measured with the external 6-component balance, located underneath the test section. The model is mounted in the so-called half-model configuration. In this setup the forces and moments are measured in a model fixed axis system, which is shown in Figure 3.5. Balance and model rotate together to change the angle of attack. In the airfoil coordinate system the forces are given by: normal force $F_N = -F_z$, tangential force $F_T = -F_x$ and the pitching

moment $M = M_y$. The uncertainties due to the accuracy of the balance are

$$\sigma_{F_z} = \pm 0.75\,\mathrm{N} \tag{3.3}$$

$$\sigma_{F_x} = \pm 0.3\,\mathrm{N} \tag{3.4}$$

$$\sigma_{M_y} = \pm 0.77\,\mathrm{Nm} \tag{3.5}$$

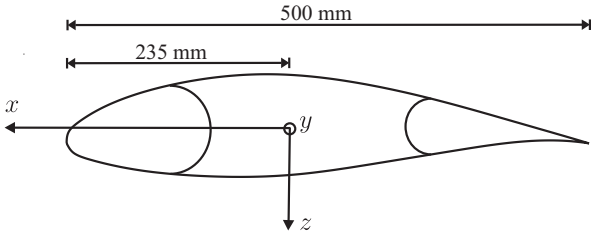

Figure 3.5: Origin of balance coordinate system

3.3.3 Pressure Measurement

The pressure of the Prandtl tube, the static pressure on the airfoil surface and the total pressure in the wake have been measured with the differential pressure scanner ESP DTC 64HD[1]. The reference pressure was the pressure in the plenum outside the wind tunnel. The total accuracy of the scanner is ±0.06% of full scale (FS) 1 PSI.

Additionally to the scanner uncertainty, the error of the probes have to be taken into account. For the pressure tubes of the wake and the Prandtl tube an error occurs due to angular misalignments. According to Nitsche and Brunn (2006, p. 16) the error is negligible for flow inclinations of ±8°. This is true for the Prandtl tube but cannot be guaranteed for the Pitot tubes of the wake rake, although it is located about one chord length behind the airfoil. Following Nitsche and Brunn (2006, p. 16) an error of ±0.4% is applied to the total pressure measurement in the wake.

The pressure taps on the airfoil surface have a diameter of 0.3 mm and due to manufacturing imperfections an uncertainty of ±0.1% is assumed.

[1] www.pressuresystems.com

The standard uncertainty of the total pressure of the Prandtl tube is

$$\sigma_{p_t} = \pm 0.6 \cdot 10^{-3}\,\mathrm{PSI} = \pm 4.14\,\mathrm{Pa} \tag{3.6}$$

The standard uncertainty of the total pressure in the wake is

$$\sigma_{p_{w,Sen}} = \pm 0.6 \cdot 10^{-3}\,\mathrm{PSI} = \pm 4.14\,\mathrm{Pa} \tag{3.7}$$

$$\sigma_{p_{w,Tube}} = \pm 4 \cdot 10^{-3}\,\mathrm{PSI} = \pm 27.58\,\mathrm{Pa} \tag{3.8}$$

$$\sigma_{p_{w,combined}} = \pm 4.1 \cdot 10^{-3}\,\mathrm{PSI} = \pm 27.89\,\mathrm{Pa} \tag{3.9}$$

where Sen ≡ Sensor. Finally, the standard uncertainty for the static pressure on the airfoil is

$$\sigma_{p_{w,Sen}} = \pm 0.6 \cdot 10^{-3}\,\mathrm{PSI} = \pm 4.14\,\mathrm{Pa} \tag{3.10}$$

$$\sigma_{p_{w,Tube}} = \pm 1 \cdot 10^{-3}\,\mathrm{PSI} = \pm 6.9\,\mathrm{Pa} \tag{3.11}$$

$$\sigma_{p_{w,combined}} = \pm 1.2 \cdot 10^{-3}\,\mathrm{PSI} = \pm 8.05\,\mathrm{Pa} \tag{3.12}$$

3.3.4 Flap Moment Sensor

The flap moments were measured with static strain gauge torque sensors: Lorenz Typ D-2553[2]. The nominal torque of the leading-edge flap sensor is ±100 Nm and of the trailing-edge flap ±20 Nm. For signal processing a National Instrument NI 9219 card was used in the four-wire and full-bridge configuration. The standard uncertainty of the moment consists of the standard uncertainty of the sensor and the standard uncertainty of the measurement system. The uncertainty, according to the data sheets, for the trailing-edge sensor is

$$\sigma_{M_{TE,Sen}} = \pm 20 \cdot 10^{-3}\,\mathrm{Nm} \tag{3.13}$$

$$\sigma_{M_{TE,MS}} = \pm 6 \cdot 10^{-3}\,\mathrm{Nm} \tag{3.14}$$

$$\sigma_{M_{TE,combined}} = \pm 21 \cdot 10^{-3}\,\mathrm{Nm} \tag{3.15}$$

where MS ≡ measurement system. The uncertainty for the leading-edge sensor is given by

$$\sigma_{M_{LE,Sen}} = \pm 10 \cdot 10^{-2}\,\mathrm{Nm} \tag{3.16}$$

$$\sigma_{M_{LE,MS}} = \pm 3 \cdot 10^{-2}\,\mathrm{Nm} \tag{3.17}$$

$$\sigma_{M_{LE,combined}} = \pm 10.4 \cdot 10^{-2}\,\mathrm{Nm} \tag{3.18}$$

[2] www.lorenz-messtechnik.de

3.3.5 Flap Angle Sensor

The flap angles are measured with the incremental magnetic senor MSK 5000 in combination with the magnetic band ring MBR 200, by SIKO[3]. The system accuracy of the sensor according to the data sheet is $\pm 0.1°$. The sensor has max. 262500 pulses per revolution. The 32 bit digital counter of the National Instrument acquisition card NI 6210 is sufficiently high to ignore the uncertainty of this measurement. The standard uncertainty of the flap angles reduces to

$$\sigma_{\gamma,\beta} = \pm 0.1° \tag{3.19}$$

3.3.6 Geometric Uncertainties

The static pressure taps on the surface of the airfoil at half span are pictured in Figure 3.6. A total of 56 pressures were measured, 27 on the pressure side and 29 on the suction side. An exact uncertainty of the airfoil shape has not been determined. However, some uncertainties of the geometric properties can be estimated. For the chord length c the standard uncertainty is

$$\sigma_c = \pm 0.5 \cdot 10^{-3}\,\mathrm{m} \tag{3.20}$$

and for the span

$$\sigma_b = \pm 0.5 \cdot 10^{-3}\,\mathrm{m} \tag{3.21}$$

The location of the pressure taps have been measured along the surface contour. Afterwards the x and z coordinates have been calculated by a spline interpolation using the original airfoil coordinates. From the position of the pressure tubes the panel increments are determined which are then used for the integration of the pressure distribution. Hence, the standard uncertainty of the panel lengths needs to be considered:

$$\sigma_x = \pm 0.5 \cdot 10^{-3}\,\mathrm{m} \tag{3.22}$$

$$\sigma_z = \pm 0.5 \cdot 10^{-3}\,\mathrm{m} \tag{3.23}$$

[3] www.siko.de

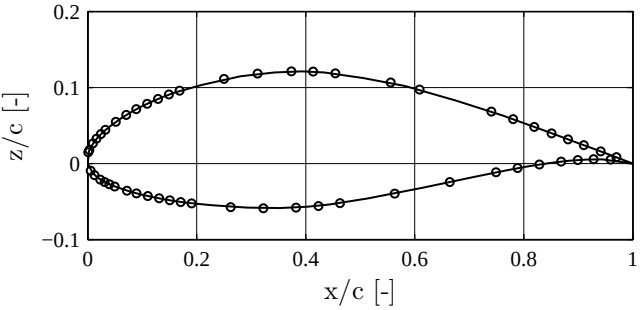

Figure 3.6: NACA 64_3618: Location of pressure taps

3.4 Post-Processing and Uncertainty

From the measured quantities the non-dimensionalized coefficients are calculated.

3.4.1 Coefficients from Balance Measurement

The normal and tangential force coefficients from the balance force in the airfoil reference system B^* are given by

$$c_N = \frac{-F_z}{q_\infty bc} \tag{3.24}$$

$$c_T = \frac{-F_x}{q_\infty bc} \tag{3.25}$$

The forces are non-dimensionalized by the dynamic pressure q_∞ provided by the wind tunnel data. It is assumed that the complete wing area contributes to the lift generation, although a junction flow might be present between the wing and the endplates. It is shown retroactively that the coefficients from the balance and integrated surface pressure measurement agree well in the attached flow regime, which supports the assumption of low endplate influence. To establish the loads in the wind axis system a transformation using the measured angle of attack α from the support

needs to be applied:

$$\begin{pmatrix} c_L \\ c_D \end{pmatrix} = \begin{pmatrix} \cos\alpha(t) & -\sin\alpha(t) \\ \sin\alpha(t) & \cos\alpha(t) \end{pmatrix} \cdot \begin{pmatrix} c_N \\ c_T \end{pmatrix} \tag{3.26}$$

It should be noted that the forces and moments also include the contribution of the endplates and especially the influence of the protective housing on top of the wing. The moment coefficient of the airfoil around the quarter chord point according to Figure 3.5 is given by

$$c_{m,c/4} = \frac{M_y}{q_\infty b c^2} - 0.22 c_N \tag{3.27}$$

The standard uncertainties of the above coefficients can be calculated after GUM Type B using the uncertainties derived in the previous section. The uncertainty is always calculated with respect to the maximum value of each parameter. This is: $q_{\infty,max} = 970\,\text{Pa}$; $F_{z,max} = 800\,\text{N}$; $F_{x,max} = 32\,\text{N}$; $M_{y,max} = 44\,\text{Nm}$; $\alpha_{max} = 20°$; The uncertainties at a confidence level of 2σ are given by:

$$c_N \pm 1.17\%\,(\text{k} = 2) \tag{3.28}$$

$$c_T \pm 0.45\%\,(\text{k} = 2) \tag{3.29}$$

$$c_{m,c/4} \pm 2.74\%\,(\text{k} = 2) \tag{3.30}$$

$$c_L \pm 1.2\%\,(\text{k} = 2) \tag{3.31}$$

$$c_D \pm 0.6\%\,(\text{k} = 2) \tag{3.32}$$

3.4.2 Coefficients from Pressure Measurement

The static pressure on the airfoil surface is non-dimensionalized to obtain the pressure coefficient

$$c_{p,i} = \frac{p_i - (p_t - q_\infty)}{q_\infty} \tag{3.33}$$

where p_i is the static pressure at the respective pressure tap. The total pressure p_t is is taken from the Prandtl tube and the dynamic pressure q_∞ from the wind tunnel nozzle. According to the pressure integration

scheme implemented within the panel method of section 2.1, panel borders can be calculated from the coordinates of the pressure taps. These points are located in the middle of two pressure taps. After the panel borders are calculated the increment of the panels in x^* and z^* direction can be derived: $\Delta x_i^* = x_{i+1}^* - x_i^*$ $\Delta z_i^* = z_{i+1}^* - z_i^*$. The integral coefficients in the normal and tangential direction are then given by summation:

$$c_N = \sum_{i=1}^{56} -c_{p,i} \Delta x_i^* \tag{3.34}$$

$$c_T = \sum_{i=1}^{56} c_{p,i} \Delta z_i^* \tag{3.35}$$

Care needs to be taken about the signs. This procedure begins the panel counting at the trailing edge, moves to the leading edge on the lower side and returns to the trailing edge on the upper side, as described in section 2.1.3.

Due to the fact that the flaps rotate this geometric rotation needs to be incorporated in the calculation of the panel points. This can be done by a translation and rotation using the leading-edge flap angle γ and trailing-edge flap angle β (compare section 2.1.2). The new coordinates, subscript r, are defined in the coordinate system B^* as follows:

$$\begin{pmatrix} x_{r,i}^* \\ z_{r,i}^* \end{pmatrix} = \begin{pmatrix} x_l^* \\ z_l^* \end{pmatrix} + \begin{pmatrix} \cos(\gamma) & \sin(\gamma) \\ -\sin(\gamma) & \cos(\gamma) \end{pmatrix} \begin{pmatrix} x_i^{'} \\ z_i^{'} \end{pmatrix} \qquad x_i^* \leq x_l^* \tag{3.36}$$

$$\begin{pmatrix} x_{r,i}^* \\ z_{r,i}^* \end{pmatrix} = \begin{pmatrix} x_t^* \\ z_t^* \end{pmatrix} + \begin{pmatrix} \cos(-\beta) & \sin(-\beta) \\ -\sin(-\beta) & \cos(-\beta) \end{pmatrix} \begin{pmatrix} x_i^{'} \\ z_i^{'} \end{pmatrix} \qquad x_i^* \geq x_t^* \tag{3.37}$$

The uncertainties at a confidence level of 2σ ($p_{t,max} = 0.15\,\mathrm{PSI}$) are given by:

$$c_p \pm 0.62\% \,(\mathrm{k} = 2) \tag{3.38}$$

$$c_N \pm 1.19\% \,(\mathrm{k} = 2) \tag{3.39}$$

$$c_T \pm 1.19\% \,(\mathrm{k} = 2) \tag{3.40}$$

Considering that the influence of the flap angle uncertainty is small yields the estimated results:

$$c_L \pm 1.25\% \,(\mathrm{k} = 2) \tag{3.41}$$

$$c_D \pm 1.25\% \,(\mathrm{k} = 2) \tag{3.42}$$

3.4.3 Drag from Wake Rake Measurements

The total drag can be calculated by the momentum deficit between a position in the flow ahead and after the airfoil. The following equation is valid when the momentum balance is applied to a control volume around the airfoil:

$$c_D = \frac{2}{c} \int_W \frac{v_w}{v_\infty} \left(1 - \frac{v_w}{v_\infty}\right) dy \tag{3.43}$$

where v_w is the velocity in the wake. If the static pressure cannot be measured in the wake, according to Barlow, Rae and Pope (1999, p. 178) the wake rake needs to be placed at least 0.7 chord length behind the airfoil. Then it can be assumed that the static pressure in the wake is equal to the freestream static pressure. Eq. 3.43 can then be written as

$$c_D = \frac{2}{c} \int_W \sqrt{\frac{p_{tw} - p_\infty}{q_\infty}} \left(1 - \sqrt{\frac{p_{tw} - p_\infty}{q_\infty}}\right) dy \tag{3.44}$$

where p_{tw} is the total pressure in the wake. Barlow, Rae and Pope (1999, p. 178) suggest further to use q_∞ from the wake rake measurements, since the velocity gradient in the wind tunnel might influence the results. In the present investigation the wake rake had no static pressure tube. Therefore, the static pressure variation behind the airfoil is taken from the RANS computations using the tunnel domain of Figure 2.10. The results are shown in Figure 3.7. In the left diagram the static pressure is related to the freestream dynamic pressure at certain positions behind the wake. One can see that at a distance of one chord length behind the airfoil the difference between the static pressure in the wake and the freestream is less than 1.5%. This is in good agreement to the results of Goett (1939, p. 5). Even at higher angles of attack the pressure difference increases only slightly, as can be seen in the right diagram.

Based on an error of 1.5% for the static pressure the total uncertainty with a confidence level of 2σ can be estimated for the drag coefficient:

$$c_D \pm 6.4\% \,(\mathrm{k} = 2) \tag{3.45}$$

Finally, it should be mentioned that the wake survey method cannot be used to measure the drag of stalled airfoils or of airfoils with flaps down, as stated in Barlow, Rae and Pope (1999, p. 178).

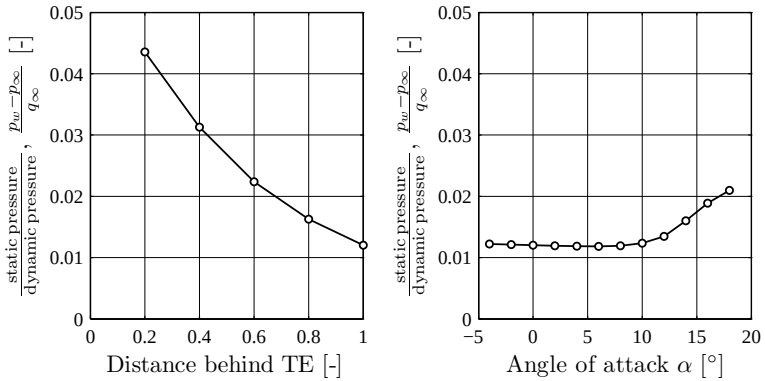

Figure 3.7: CFX RANS computations: Static pressure variation behind airfoil; Left: Different positions behind trailing edge; Right: Different angles of attack at one chord behind trailing edge

Chapter 4

Results - Wing Design

This chapter presents the results of the preliminary design study of the experimental wing. These results indicate the expected aerodynamic behavior of the airfoil for prescribed flow and structural parameters. At this stage only the flap motion is considered, i.e. Eq. 2.56 is used to obtain the flap angle. The aerodynamic pressure is assumed to be steady in each time step; hence the steady Hess-Smith formulation is used for the computation of the flow field.

The camber line of the flapped airfoil is dependent on the angle of attack and the dynamic pressure in relation to the defined design point. The design point specifies the preload moment which needs to be applied to keep the airfoil in the original shape for desired aerodynamic condition. The preload moment M_0 is equal to $M_B - nM_D$. The goal is to alleviate load fluctuations on the airfoil. The loads are given by the dynamic pressure and the lift coefficient. Initially only changes in angle of attack are considered, whereas the dynamic pressure is constant. Therefore, the load reduction LR is defined as the reduction of the standard deviation of the lift coefficient:

$$LR = 1 - \frac{\mathrm{std}\,(c_L)_{\mathrm{flexible}}}{\mathrm{std}\,(c_L)_{\mathrm{rigid}}} \tag{4.1}$$

The flow angle and the relative velocity encountered by a wind turbine airfoil section is defined by the superposition of the rotational speed and the wind speed. This situation is schematically pictured in Figure 4.1.

The velocity $v_z(t)$ is assumed to be the wind velocity and to simulate a wind gust, this velocity component undergoes a sinusoidal change of magnitude in time: $v_z(t) = v_{z0} + v_{z0}\sin(\omega t)$. In the present case v_{z0} was recalculated to provide a flow angle of 4°. It was further assumed that the change in angle of attack is ±4° which explains why the fluctuation velocity is as high as the mean velocity. This velocity is simply applied to the heaving motion of Eq. 2.6. The assumption is that the airfoil experiences the change in the vertical velocity over the entire chord length at once. This is realistic for length scales of the gusts which are in the order of the airfoil chord. Although this might not always be the case, Buhl, Gaunaa and Bak (2005) have discussed this effect for wind turbines and found that the error compared to more realistic assumptions is small. The baseline airfoil is the NACA 64_3618. The chord length c is 0.5 m,

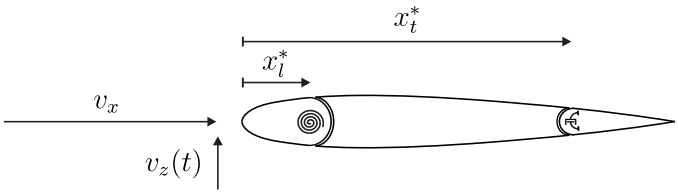

Figure 4.1: 1DOF case: gust applied by time-dependent vertical velocity component $v_z(t)$, v_x = rotational speed, coupling between flaps given by factor n, spring stiffness k_γ, damping constant d_β;

the baseline velocity v_x is 40 m/s. The dynamic pressure is given by $q = \rho/2v_x^2$, where ρ is $1.204\,kg/m^3$. For this preliminary study the frequency ω is chosen to yield a reduced frequency of $k = 0.01$, low enough to satisfy the assumption of steady aerodynamics. The baseline structural parameters are as follows: leading-edge hinge point $x_l^* = 0.2c$, trailing-edge hinge point $x_t^* = 0.7c$, coupling ratio $n = 3$, damping constant $d_\beta = 1$ Nms/rad.

A variety of parameters have been studied and all parameters are given in the caption of the respective Figure. Additionally, the load reductions are summarized in a table, indicating also the minimum and maximum flap angles.

4.1 Structural Parameter

Influence of Stiffness

Figure 4.2 shows the influence of the torsional spring stiffness k_γ. The solid line indicates the rigid airfoil. At time $t = 0$ the wind velocity $v_z(t)$ increases; hence angle of attack. This can be seen by the increasing lift coefficient. Subsequently the lift coefficient follows the prescribed sinusoidal change of the wind velocity.

Considering the lift coefficient of the flapped airfoil the load reduction LR increases as the stiffness decreases, see Table 4.1. It shows that at very small stiffnesses, here $k_\gamma = 10\,\mathrm{Nm/rad}$, the camber change is so large that a sign change occurs in the lift-curve slope $\delta c_L/\delta\alpha$. The lift decreases with increasing angle of attack. Under these conditions no further load reduction can be expected. In the present configuration a maximum load reduction LR of 88.3% is obtained for a stiffness $k_\gamma = 50\,\mathrm{Nm/rad}$.

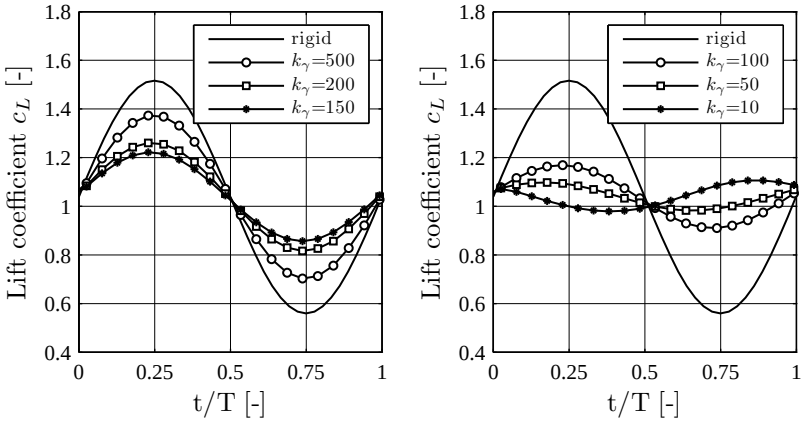

Figure 4.2: Influence of stiffness k_γ on lift coefficient c_L; NACA 64_3618; $v_x = 40\frac{\mathrm{m}}{\mathrm{s}}$; $v_z(t) = v_{z0} + v_{z0}\sin(1.6t)$; $x_l^* = 0.2$ $x_t^* = 0.7$; $d_\beta = 1\frac{\mathrm{Nms}}{\mathrm{rad}}$; $n = 3$

Table 4.1: Reduction of lift coefficient amplitude fluctuation, minimum and maximum flap deflections for different spring stiffnesses

spring stiffness [Nm/rad]	LR [%]	γ_{min} [°]	γ_{max} [°]	β_{min} [°]	β_{max} [°]	γ_0 [°]
10	87.1	-2.31	2.24	-6.94	6.73	105.08
50	88.3	-1.88	1.85	-5.65	5.54	21.02
100	73.8	-1.53	1.51	-4.59	4.54	10.51
150	63.0	-1.29	1.28	-3.87	3.84	7.02
200	55.0	-1.11	1.11	-3.34	3.33	5.25
500	32.0	-0.61	0.62	-1.84	1.85	2.10

Influence of Damping

One can also see from Figure 4.2 that at stiffnesses below $k_\gamma = 50\,\mathrm{Nm/rad}$ a phase shift occurs in the lift coefficient. This is mainly due to the increasing damping force. The damper is installed at the trailing-edge flap which means its contribution to the flap motion is multiplied with the factor n^2, see Eq. 2.56. This is confirmed by the results of Figure 4.3, where the damping constant is varied. If the stiffness is large, the elastic force dominates the camber change.

Influence of Coupling Ratio

Figure 4.4 shows the lift coefficient for different coupling ratios n. The load reduction increases with increasing ratio n up to 4, beyond this value no further influence on the lift coefficient is detected. This might be caused by the gear box which is realized through the coupling mechanism. The deflection of the leading-edge flap are transferred to the trailing-edge flap. Contrary the aerodynamic moment is transferred with the coupling ratio n to the leading-edge. Presumably the moment equilibrium prevents further deflections. The obtained load reductions are summarized in Table 4.2

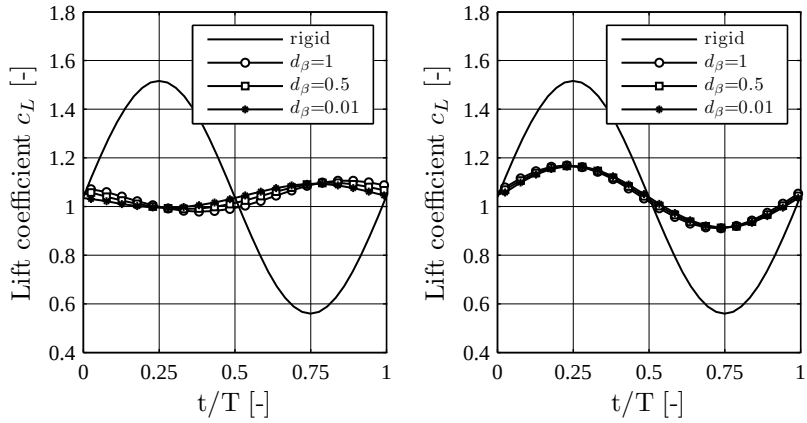

(a) $k_\gamma = 10\frac{\mathrm{Nm}}{\mathrm{rad}}$ **(b)** $k_\gamma = 100\frac{\mathrm{Nm}}{\mathrm{rad}}$

Figure 4.3: Influence of damping d_β on lift coefficient c_L; NACA 64_3618; $v_x = 40\frac{\mathrm{m}}{\mathrm{s}}$; $v_z(t) = v_{z0} + v_{z0}\sin(1.6t)$; $x_l^* = 0.2$; $x_t^* = 0.7$; $n = 3$

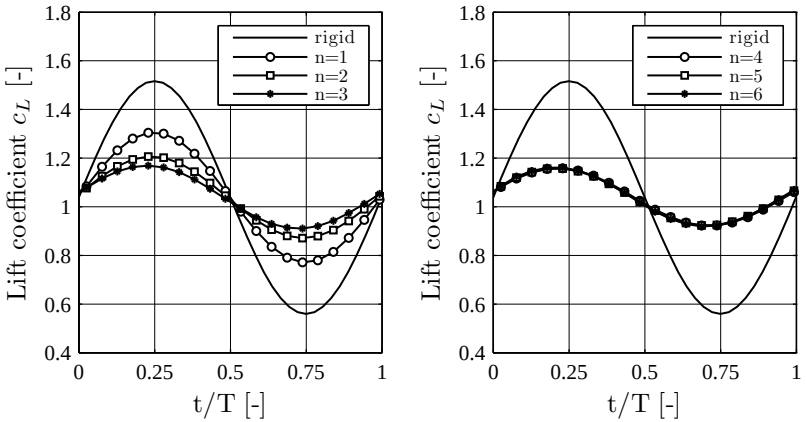

Figure 4.4: Influence of coupling ratio n on lift coefficient c_L; NACA 64_3618; $v_x = 40\frac{\mathrm{m}}{\mathrm{s}}$; $v_z(t) = v_{z0} + v_{z0}\sin(1.6t)$; $x_l^* = 0.2$; $x_t^* = 0.7$; $d_\beta = 1\frac{\mathrm{Nms}}{\mathrm{rad}}$; $k_\gamma = 100\frac{\mathrm{Nm}}{\mathrm{rad}}$

Table 4.2: Reduction of lift coefficient amplitude fluctuation, minimum and maximum flap deflections for different coupling ratios

coupling ratio	LR [%]	γ_{min} [°]	γ_{max} [°]	β_{min} [°]	β_{max} [°]	γ_0 [°]
1	46.0	-2.85	2.84	-2.85	2.84	6.17
2	66.1	-2.05	2.04	-4.10	4.07	8.34
3	73.8	-1.53	1.51	-4.59	4.54	10.51
4	76.1	-1.19	1.17	-4.75	4.69	12.68
5	76.2	-0.95	0.94	-4.77	4.69	14.84
6	75.4	-0.79	0.77	-4.72	4.65	17.01

4.2 Airfoil Shape

Influence of Flap Length

In Figure 4.5 the results for different flap lengths are shown. In each figure the leading-edge flap is constant and the trailing-edge flap length changes. In sum 9 configurations have been studied with flap lengths of 10%, 20% and 30% in terms of the chord. The results are summarized in Table 4.3.

It demonstrates that the largest influence is produced by the leading-edge flap, where a leading-edge flap length of 30% provides load reductions of above 90%. Since this is a quite big flap it was decided to consider a 20% long leading-edge flap as the baseline. As expected, looking at the preload angle γ_0, the required preload is always the highest for a trailing-edge flap length of 30%.

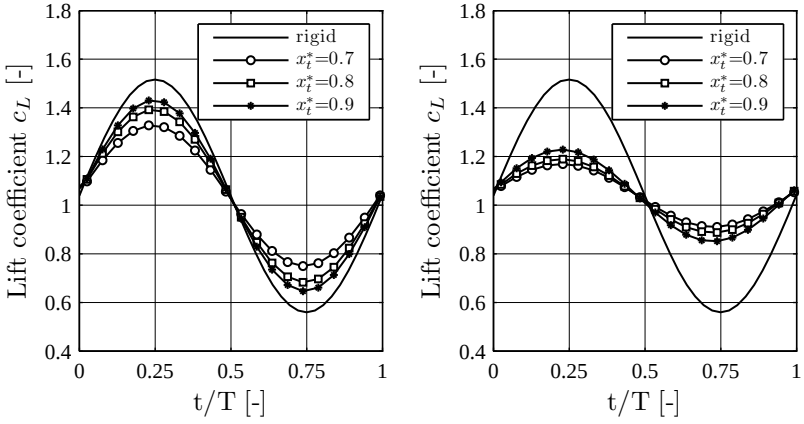

(a) $x_l^* = 0.1$ **(b)** $x_l^* = 0.2$

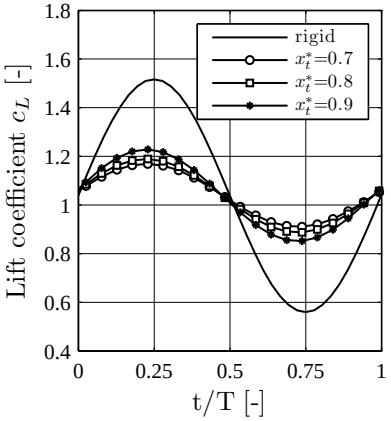

(c) $x_l^* = 0.3$

Figure 4.5: Influence of flap length on lift coefficient c_L; NACA 64_3618; $v_x = 40\frac{\mathrm{m}}{\mathrm{s}}$; $v_z(t) = v_{z0} + v_{z0}\sin(1.6t)$; $n = 3$; $d_\beta = 1\frac{\mathrm{Nms}}{\mathrm{rad}}$; $k_\gamma = 100\frac{\mathrm{Nm}}{\mathrm{rad}}$

Table 4.3: Reduction of lift coefficient amplitude fluctuation, minimum and maximum flap deflections for different flap lengths

flap length	LR [%]	γ_{min} [°]	γ_{max} [°]	β_{min} [°]	β_{max} [°]	γ_0 [°]
$x_l^* = 0.1$						
$x_t^* = 0.7$	41.4	-0.81	0.81	-2.44	2.44	7.31
$x_t^* = 0.8$	28.2	-0.64	0.64	-1.92	1.93	3.02
$x_t^* = 0.9$	20.5	-0.65	0.66	-1.95	1.97	1.13
$x_l^* = 0.2$						
$x_t^* = 0.7$	73.8	-1.53	1.51	-4.59	4.54	10.51
$x_t^* = 0.8$	69.5	-1.74	1.73	-5.22	5.19	6.23
$x_t^* = 0.9$	61.9	-2.27	2.27	-6.81	6.81	4.33
$x_l^* = 0.3$						
$x_t^* = 0.7$	95.2	-2.16	2.13	-6.49	6.38	15.74
$x_t^* = 0.8$	91.5	-2.73	2.70	-8.18	8.09	6.22
$x_t^* = 0.9$	90.2	-3.99	3.95	-11.97	11.84	9.56

Influence of Airfoil Thickness

The influence of airfoil thickness has been studied with the NACA 4 Digit Series. Figure 4.6 shows the results for different symmetric airfoils with thicknesses up to 40%. With increasing thickness the load reduction decreases, see Table 4.4. But the load reduction changes not significantly until a thickness of 30%. For the 40% thick airfoil the load reduction reduces to 68% which is about 10% less compared to the 5% thick airfoil.

Table 4.4: Reduction of lift coefficient amplitude fluctuation, minimum and maximum flap deflections for different airfoil thickness

NACA	LR [%]	γ_{min} [°]	γ_{max} [°]	β_{min} [°]	β_{max} [°]	γ_0 [°]
0005	77.4	-1.61	1.60	-4.84	4.81	5.99
0015	77.6	-1.58	1.57	-4.75	4.72	5.50
0030	74.5	-1.48	1.49	-4.45	4.47	3.95
0040	68.0	-1.31	1.36	-3.93	4.09	2.36

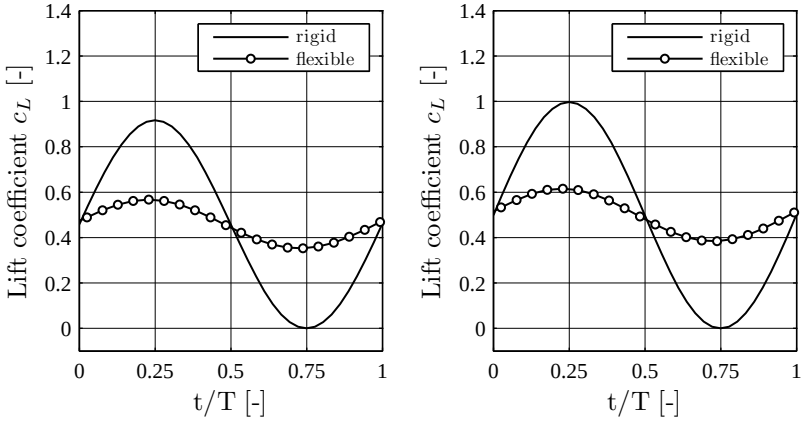

(a) NACA0005 **(b)** NACA0015

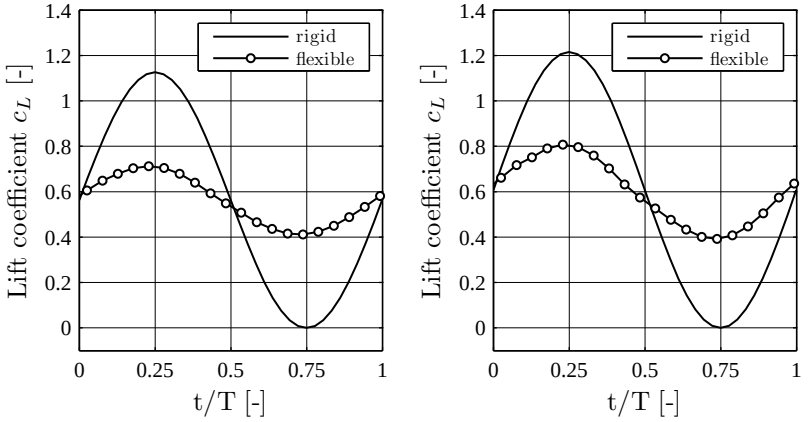

(c) NACA0030 **(d)** NACA0040

Figure 4.6: Influence of airfoil thickness on lift coefficient c_L; $v_x = 40\frac{\mathrm{m}}{\mathrm{s}}$; $v_z(t) = v_{z0} + v_{z0}\sin(1.6t)$; $n = 3$; $x_l^* = 0.2$; $x_t^* = 0.7$; $d_\beta = 1\frac{\mathrm{Nms}}{\mathrm{rad}}$; $k_\gamma = 100\frac{\mathrm{Nm}}{\mathrm{rad}}$

However, more important seems to be that the preload moment decreases (compare γ_0 in Table 4.4) with increasing thickness. This indicates that the contribution of the trailing edge decreases, although the total pressure difference increases. See here for example the pressure distribution of a NACA 0040 and NACA 0060 in Figure 4.7. This demonstrates once more the importance of finding a pressure distribution in conjunction with the coupling ratio for an optimized moment balance.

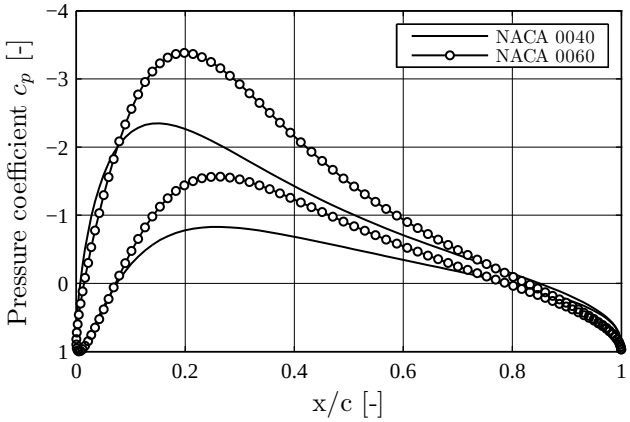

Figure 4.7: HSPM computation: Pressure distribution for NACA 0040 and NACA 0060

Influence of Airfoil Camber

The influence of airfoil camber has also been studied with the NACA 4 Digit Series. A 10% thick airfoil with a maximum camber at 40% chord was used as baseline for the camber change. The results are displayed in Figure 4.8. The obtained load reductions are summarized in Table 4.5. The load reduction increases with increasing camber. However, the influence of the camber line on the load reduction is less than the airfoil thickness.

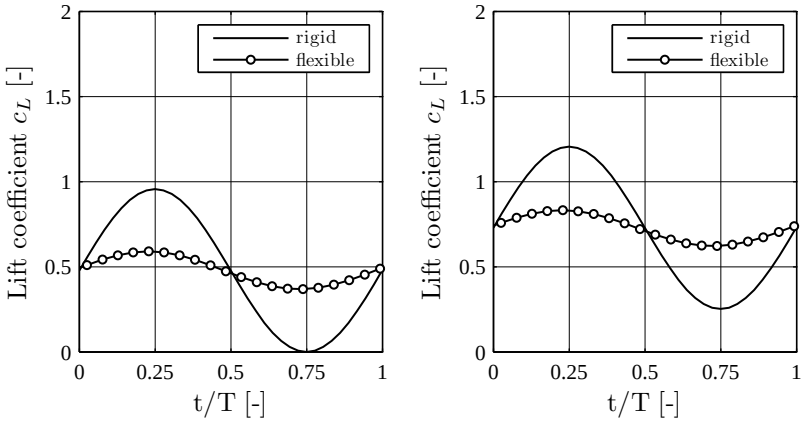

(a) NACA0010 **(b)** NACA2410

(c) NACA4410 **(d)** NACA6410

Figure 4.8: Influence of airfoil camber on lift coefficient c_L; $v_x = 40\frac{\mathrm{m}}{\mathrm{s}}$; $v_z(t) = v_{z0} + v_{z0}\sin(1.6t)$; $x_l^* = 0.2$; $x_t^* = 0.7$; $n = 3$; $d_\beta = 1\frac{\mathrm{Nms}}{\mathrm{rad}}$; $k_\gamma = 100\frac{\mathrm{Nm}}{\mathrm{rad}}$

Table 4.5: Reduction of lift coefficient amplitude fluctuation, minimum and maximum flap deflections for different airfoil camber

NACA	LR [%]	γ_{min} [°]	γ_{max} [°]	β_{min} [°]	β_{max} [°]	γ_0 [°]
0010	77.6	-1.60	1.58	-4.79	4.75	5.80
2410	78.8	-1.61	1.60	-4.83	4.79	8.32
4410	79.8	-1.63	1.62	-4.89	4.85	10.87
6410	81.4	-1.65	1.64	-4.96	4.92	13.44

4.3 Flow Parameters

Influence of Velocity

Until now only changes in the angle of attack have been considered. Keeping the flow velocity constant ($v_x = 40\,\mathrm{m/s}$). Therefore, the load reduction was solely examined on the basis of lift coefficient. However, the forces and moments on the airfoil scale with the square of the velocity, thus, different velocities have a significant influence on the flap deflection and the study of performance at different speeds is critical.

The baseline velocity $v_x = 40\,\mathrm{m/s}$ is used to calculate the preload moment. The velocity was then increased to $v_x = 60\,\mathrm{m/s}$ and decreased to $v_x = 20\,\mathrm{m/s}$. Keeping the preload moment constant. Figure 4.9 shows the results. It reveals that for lower wind speeds the airfoil camber increases and stays cambered over the entire change in the angle of attack. This is demonstrated by the flap angles given in Table 4.6, leading to an increased mean lift. It is apparent that these unrealistic high lift coefficient values arise because flow separation is neglected in the computations (potential flow). In comparison to a higher flow velocity, the airfoil is decambered all the time and consequently the mean lift is lower. The flap angles are not limited in the calculations, as they would be on a physical model.

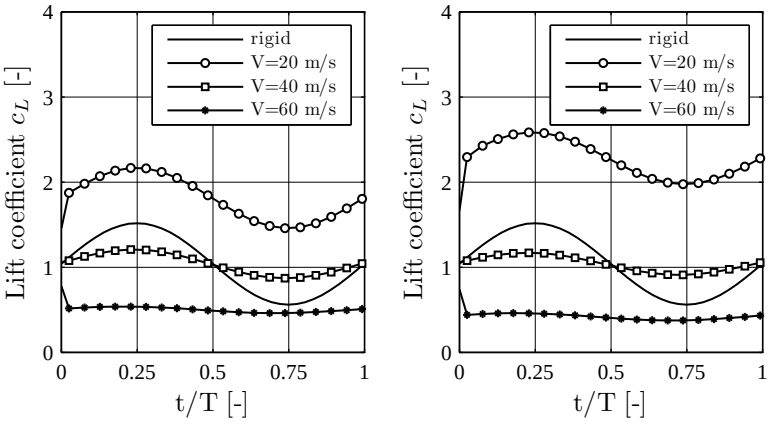

(a) n = 2 **(b)** n = 3

Figure 4.9: Influence of velocity v_x on lift coefficient c_L; preload moment calculated for $v_x = 40\frac{\mathrm{m}}{\mathrm{s}}$; NACA 64_3618; $x_l^* = 0.2$; $x_t^* = 0.7$; $v_z(t) = v_{z0} + v_{z0}\sin(1.6t)$; $d_\beta = 1\frac{\mathrm{Nms}}{\mathrm{rad}}$; $k_\gamma = 100\frac{\mathrm{Nm}}{\mathrm{rad}}$

Table 4.6: Reduction of lift coefficient amplitude fluctuation, minimum and maximum flap deflections for different velocities

	LR [%]	γ_{min} [°]	γ_{max} [°]	β_{min} [°]	β_{max} [°]	γ_0 [°]
n = 2						
V = 20	27.6	-5.97	-4.40	-11.95	-8.79	8.34
V = 40	66.1	-2.05	2.04	-4.10	4.07	8.34
V = 60	92.0	0.64	6.35	1.29	12.70	8.34
n = 3						
V = 20	37.7	-6.39	-4.07	-19.18	-12.22	10.51
V = 40	73.8	-1.53	1.51	-4.54	4.59	10.51
V = 60	91.1	0.79	4.53	2.38	13.60	10.51

Influence of Reynolds Number

The previous results indicate the behavior of the flapped airfoil. The flow is assumed to be inviscid. For the design of the experimental wing, Reynolds number effects can occur and are therefore estimated with viscous XFoil computations. The wind tunnel has a velocity range up to 68 m/s. Relative velocities in the outer part of large wind turbines can be as large as 60 m/s. Since the chord length of those turbines are at least 1.5 m, it is apparent that Reynolds numbers in the range encountered by MW turbines cannot be achieved in the experiment.

The wind tunnel test speed is limited to 40 m/s, mainly because of structural loads. The wing is placed vertically in the test section and is only fixed at one end. If a chord length of 0.5 m is assumed, this yields a Reynolds number of 1.35 E6. From the calculated polars in Figure 4.10 one can see that the chosen airfoil is sensitive to the Reynolds number when the free transition mode is chosen in XFoil. It seems that a laminar separation bubble occurs also for a Reynolds number of 1.5 E6. A N_{crit} factor of 7 is used. Since XFoil is known to overpredict the lift in the nonlinear regime these results were only taken as a guide. Additionally, the lift is calculated for a fixed transition at 5% chord length. As expected the separation bubble disappears, but the regime where the lift-curve slope becomes nonlinear starts earlier. For clarity the lift coefficient for a Reynolds number of 10 E6 is plotted. Based on these results it is necessary to realize the highest Reynolds number possible. From this view point and considering that a larger chord length provides more space for a stiffer wing construction, a chord length of 0.5 m has been chosen for the wind tunnel model.

Influence of Tunnel Blockage

The higher chord length will then increase the blockage of the wind tunnel. To estimate the influence of the wind tunnel walls RANS computations were carried out. Figure 4.11 shows the polars obtained with settings described in section 2.4. The lift-curve slope computed including the tunnel is sightly higher compared to the freeflow condition. This is due to an additional acceleration of the flow between the walls and the wing. The maximum lift coefficient does not increase.

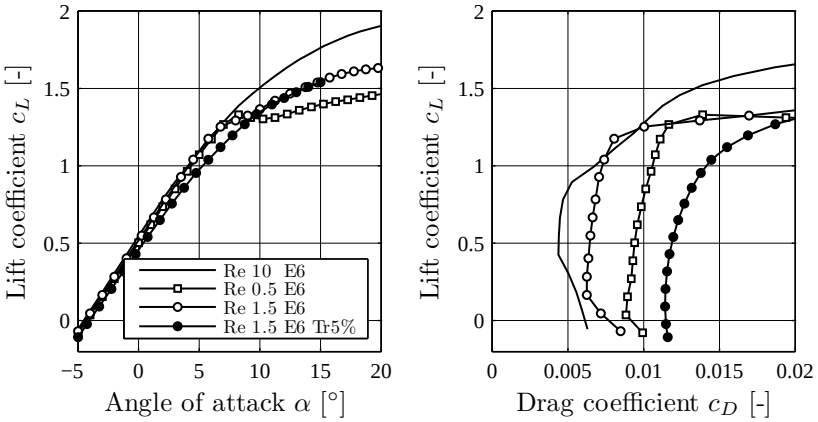

Figure 4.10: XFoil computations: Influence of Re Number and transition point on lift and drag coefficient of NACA 64_3618;

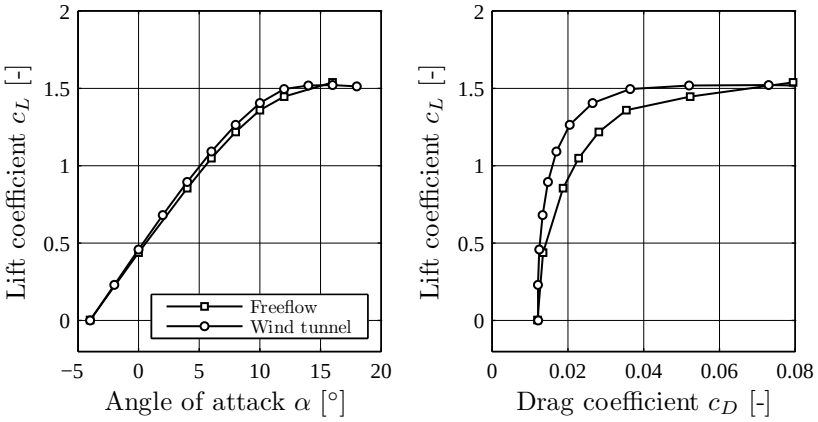

Figure 4.11: CFX RANS computations: Comparison of wall effects on lift and drag coefficient; NACA 64_3618, $c = 0.5\,\mathrm{m}$, $V_\infty = 40\,\mathrm{m/s}$, $Re = 1.36\,\mathrm{E6}$;

If one considers the drag polar on the right of Figure 4.11 one sees that the drag coefficient is lower for the tunnel flow condition, presumably due to the fact that the flow remains attached longer. Finally, it can be said that the blockage effects are present but are not significant on the lift.

4.4 Final Design

Based on these results the final wing design of the wind tunnel model is defined as follows:

- The airfoil is the NACA 64_3618
- The airfoil chord c is 0.5 m
- The wing span b is 1 m
- The leading-edge flap is 20% of the chord
- The trailing-edge flap is 30% of the chord
- It is sufficient to realize coupling ratios up to 5
- It is sufficient when the flap angles are limited to $\pm 18°$

Chapter 5

Results - Experiments

The main objective of the experimental investigation is to study the performance of the novel concept under steady conditions. The design process has determined the geometrical properties like chord and flap length. The wind tunnel measurement will confirm the intended behavior of the flapped airfoil, especially in terms of the variable lift force and lift coefficient. The influence of the following parameters have been systematically investigated: coupling ratio n, spring stiffness k_γ and preload moment M_0. Not all parameters have been combined, but for each setup three polars were measured. One polar for a respective velocity. For every polar the angle of attack was changed from $-5°$ to $+20°$ in $1°$ steps. The parameters are summarized in Table 5.1. The convention for the flap moment and angle follows the rule:

> Aerodynamic moments and flap angles which cause a decrease in camber line are positive (flaps up), those that increase the camber line are negative (flaps down).

Before the results for the flexible airfoil are shown, the airfoil characteristics for the rigid airfoil have been determined. These results have been further qualified in comparison with theory and using different measurement techniques. The rigid airfoil (also called the original shape) is the airfoil for which the flaps have been fixed with the stoppers. The flaps were adjusted with the help of a positioning device, which has the contour of the NACA 64_3618 airfoil. This device also locks the flaps. The preload moment can then be applied with the help of the moment sensor.

Table 5.1: Parameter Space Experimental Investigation

Description	Parameter	Value
coupling ratio	n	1, 2, 3, 4, 5
spring stiffness	k_γ	10 Nm/rad, 30 Nm/rad
preload moment	M_0	2, 4, 6, 8, 10 Nm
freestream velocity	V_∞	20, 30, 40 m/s
angle of attack	α	$-5^\circ \rightarrow 20^\circ$

5.1 Qualification of Measurements

Influence of Flap Gap

Prior to all measurements the influence of the gaps between the main wing and the flaps has been studied. The pressure distribution at angle of attack $\alpha = 5^\circ$ is shown in Figure 5.1. Measurements without gap tape are compared to measurements where the gap is covered with tape commonly used on sail planes. It can be concluded from these data that the gaps have an insignificant influence on the qualitative distribution. A slightly higher pressure difference can be achieved when the gaps are covered. Except for the suction side pressure values near the leading-edge flap. One can see that without gap tape the pressure value on the flap increases. On the other hand covering this gap with tape, the first pressure value on the main wing decreases. Based on these results it was decided to cover all gaps with exception of the gap at the leading-edge flap on the suction side. This configuration is the reference for all further measurements. The tape produces a significant friction force. This force has no influence on the overall conclusions of this investigation but has to be considered when calculating the static force balance of the flap motion.

Repeatability of Surface Pressure Measurements

It is important that the repeatability of the measured data is guaranteed in this investigation. The pressure scanner has been calibrated and set to zero at the beginning of the measurement campaign. Figure 5.2 shows the pressure coefficients obtained from a measurement at the beginning

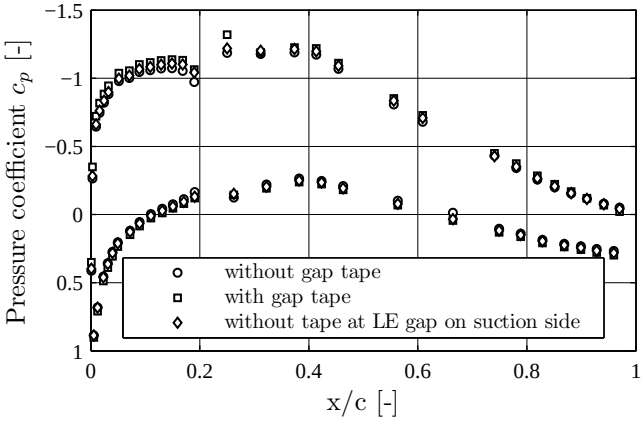

Figure 5.1: Influence of flap gap: Comparison of pressure distribution; NACA 64_3618 rigid, $\alpha = 5°$, $c = 0.5\,\mathrm{m}$, $V_\infty = 40\,\mathrm{m/s}$, $Re = 1.36\,\mathrm{E6}$;

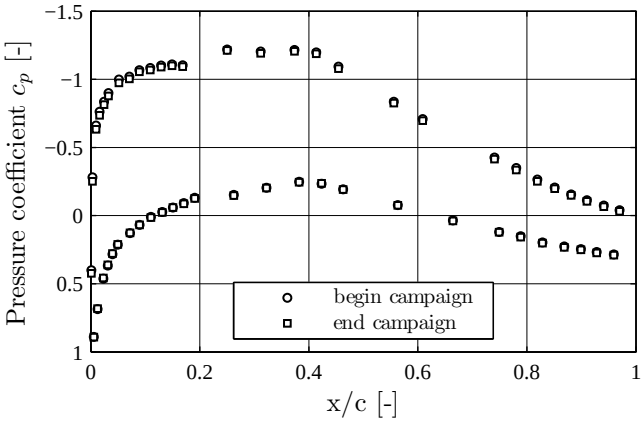

Figure 5.2: Repeatability: Comparison of pressure distribution at begin and end of measurement campaign; NACA 64_3618 rigid, $\alpha = 5°$, $c = 0.5\,\mathrm{m}$, $V_\infty = 40\,\mathrm{m/s}$, $Re = 1.36\,\mathrm{E6}$;

and after the end of the first campaign. The values are nearly identical. The pressure coefficient c_P are calculated from the averaged static pressure of 10 measurement points.

Three Dimensionality

The numerical simulations have treated the flow around the airfoil to be two-dimensional. However, the experimental setup shows that although endplates are installed, three-dimensional effects occur. A first comparison of the measured pressure distributions with XFoil and RANS computations showed a significant discrepancy. Figure 5.3 shows the lift coefficient versus angle of attack. The lift coefficient is obtained from the integration of the pressure distribution. Additionally, the coefficients from viscous and inviscid XFoil computations are plotted. One can see that the measured lift-curve slope is smaller compared to the two-dimensional computations. This is due to an induced angle of attack. To prove this conclusion the induced angle of attack was estimated with formulas for a wing with endplates presented by Prandtl and Betz (1927, pp. 17-18). The induced drag coefficient can be expressed by

$$c_{Di} = \frac{c_L^2 A}{4F'} \tag{5.1}$$

where F' is a reference area dependent on the size of the endplates:

$$F' = b^2 \left(\sqrt{13.49\frac{h}{b} + 18.83} - 3.554 \right) \tag{5.2}$$

where b is the span and h is the height of the endplates. From the induced drag the induced angle of attack can be calculated by

$$\alpha_i = \frac{c_{Di}}{c_L} \tag{5.3}$$

Subtracting the induced angle of attack from the measured angle yields the effective angle of attack:

$$\alpha_{eff} = \alpha_0 - \alpha_i \tag{5.4}$$

The corrected lift curve is given in Figure 5.3 (open circle). This curve lies between the inviscid and viscous curve. Assuming that a 3D correction should not overcorrect the measured values, these results seem to be implausible. Yet, there are still some unknowns and differences in the experimental setup which explain these circumstances. First, Eq. 5.2 is derived for a wing where the flow passes the endplates at each side symmetrically. This is not the situation in the present case since the lower endplate is near the wind tunnel floor. Second, the wind tunnel walls effect the flow around the airfoil, which was already seen in the RANS computations presented in section 4.3. Here it was seen that the lift-curve slope was higher for the tunnel flow computation. However,

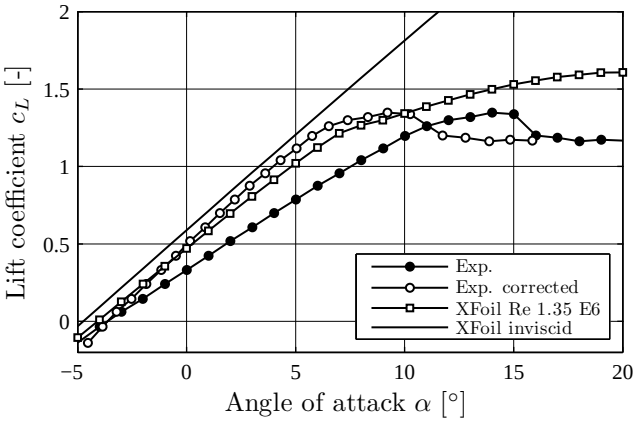

Figure 5.3: Three Dimensionality: Comparison of measured and corrected lift coefficient with 2D computations; NACA 64_3618 rigid, $c = 0.5\,\mathrm{m}$, $V_\infty = 40\,\mathrm{m/s}$, $Re = 1.36\,\mathrm{E6}$;

applying this correction reduces the angle of attack at c_{Lmax}, i.e. the airfoil stalls earlier. This is somewhat inexplicable. The stall characteristics are presumably different compared to an airfoil without flaps. Furthermore, the airfoil polars of the NACA 64_3618 given by Abbott and Doenhoff (1959) indicate that the maxium lift coefficient is highly dependent on the Reynolds number and surface roughness.

Finally, it can be concluded that three-dimensional effects are signif-

icant in the present set up, but the goal is to measure differences to a reference case and for this purpose the tree-dimensional effects become less important. Therefore, no corrections have been applied when experimental results are compared to one other. The mismatch in c_{Lmax} is ignored because the present investigation focuses mainly on the characteristics in the linear, i.e. attached flow, regime.

Comparison Balance and Surface Pressure

Additionally, to the integration of the pressure distribution the lift coefficient can be derived from the balance measurement. A comparison of the obtained values is shown in Figure 5.4. The left figure presents the

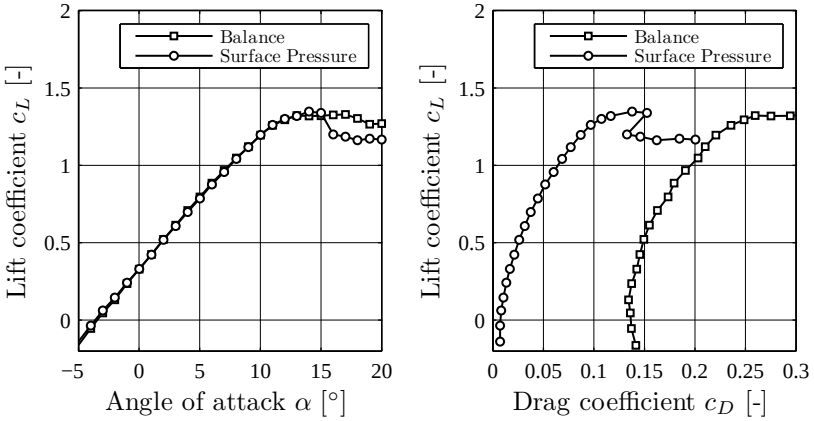

Figure 5.4: Lift and drag coefficients: Comparison of pressure and balance measurements; NACA 64_3618 rigid, $c = 0.5\,\mathrm{m}$, $V_\infty = 40\,\mathrm{m/s}$, $Re = 1.36\,\mathrm{E6}$;

lift coefficient. The agreement is perfect over the entire angle of attack range. A difference occurs in the values where the flow is separated. The balance predicts higher lift coefficients compared to the pressure integration. This confirms the correctness of the pressure measurement and the implemented integration scheme. Since the balance also measures the

influence of the endplates and the housing, it is assumed that the higher force coefficient is related to this effect.

On the right of Figure 5.4 the drag coefficients obtained from the balance and the surface pressure integration are compared. One can see a large discrepancy between the pressure integration and balance measurement. The drag force from the balance is far to high for typical drag values of an airfoil. This is also related to the endplates and the housing, which have a high contribution to the force in x-direction.

Moment Coefficient

The moment coefficient about the quarter-chord point is given in Figure 5.5. The coefficient is obtained from pressure integration along the airfoil surface and from the balance measurement. Additionally, the coefficient from XFoil is shown. The agreement between the values is good. The results indicate that the aerodynamic center of the NACA 64_3618 is close to the quarter-chord point, because the moment coefficient remains constant over the entire angle of attack range.

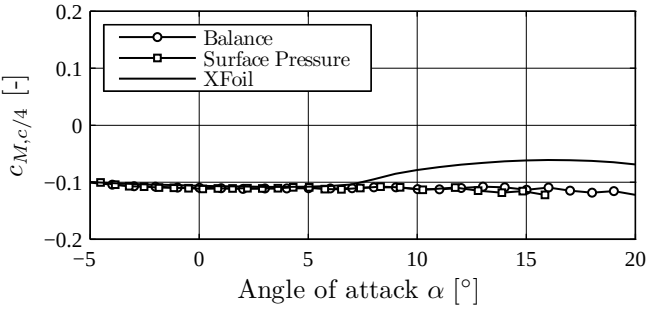

Figure 5.5: Moment coefficient: Comparison of pressure and balance measurements; NACA 64_3618 rigid, $c = 0.5\,\text{m}$, $V_\infty = 40\,\text{m/s}$, $Re = 1.36\,\text{E6}$;

Drag from Wake Rake

Figure 5.6 compares the drag coefficient obtained from the pressure integration of the wake rake to a drag coefficient calculated by XFoil. The XFoil computation is carried out with a fixed transition at 20% chord. The results agree well in the attached flow regime and the drag coefficient remains constant. At an angle of attack at about 8° the XFoil result predicts an increase in drag. The wake rake measurements indicate lower drag up to 12°. This coincides with the lift coefficient from Figure 5.4. Above 12° the drag increases. The flow in this region is highly separated, and both the computation and the measurement are no longer reliable. The dynamic of the flow separation can not be captured by the wake rake as the sampling frequency of the pressure measurements is too low. Furthermore, the angular misalignment of the flow to the Pitot tubes is too large.

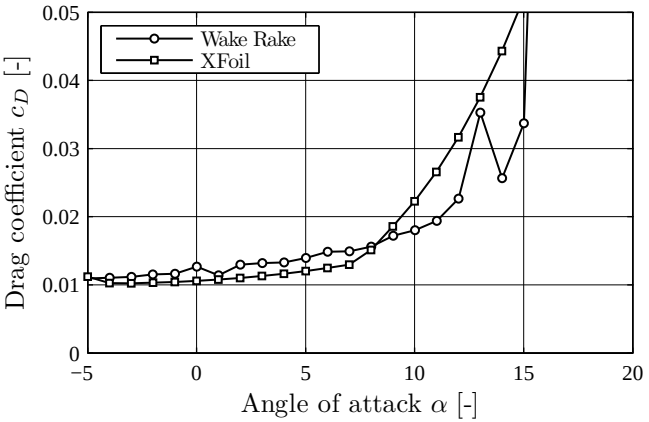

Figure 5.6: Drag coefficient from wake rake measurement; NACA 64_3618 rigid, $c = 0.5\,\mathrm{m}$, $V_\infty = 40\,\mathrm{m/s}$, $Re = 1.36\,\mathrm{E6}$;

Conclusion

The above described results indicate that the measurements predict correct and plausible values. The effect of induced drag is significant and needs to be considered in the comparison of the measurements and the two-dimensional computations. These results were mainly presented to demonstrate the quality and reliability of the measurement technique. The major goal is to illustrate the difference between the rigid airfoil configuration and the influence on the loads of the flapped airfoil.

In the following sections the lift coefficients are obtained from the surface pressure integration, the moment coefficients are calculated from the balance measurement and drag coefficients are always obtained from the wake survey. Again, the drag coefficients are only valid in the attached flow regime.

5.2 Rigid Airfoil

5.2.1 Reynolds Number Effects

From the design study of the wing it was found that Reynolds number effects are significant for NACA 64_3618. Therefore, it is important to know if Reynolds number effects are dominant in the experimental setup. Three freestream velocities were tested in the wind tunnel: 20, 30, 40 m/s. These correspond to Reynolds numbers of 0.68 E6, 1.02 E6 and 1.36 E6. Figure 5.7 and 5.8 show the polars for all three test speeds. It can be seen that in contradiction to the XFoil predictions of section 4.3 the Reynolds number has no influence on the airfoil characteristics. The transition of the boundary layer has not been determined in the experiment. It can be assumed that the boundary layer becomes turbulent when it passes the flap gap. This takes place at 20% chord length. A transition trip is effectively implemented.

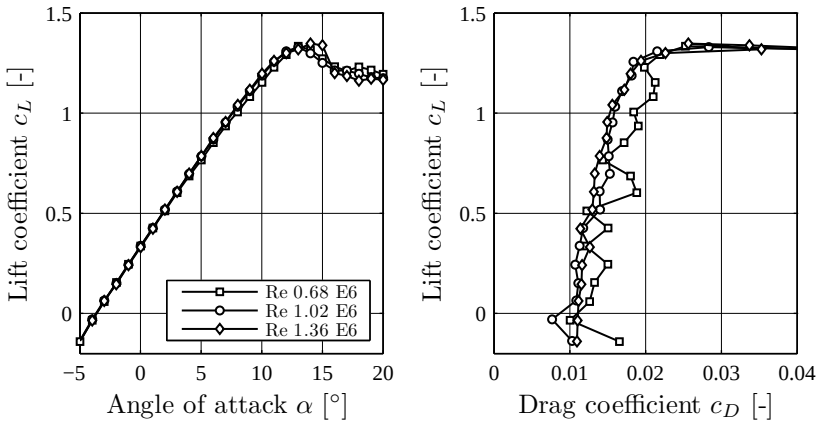

Figure 5.7: Influence of Reynolds number on force coefficient; NACA 64_3618 rigid, $c = 0.5\,\mathrm{m}$, $V_\infty = 20\,\mathrm{m/s}$, $V_\infty = 30\,\mathrm{m/s}$, $V_\infty = 40\,\mathrm{m/s}$;

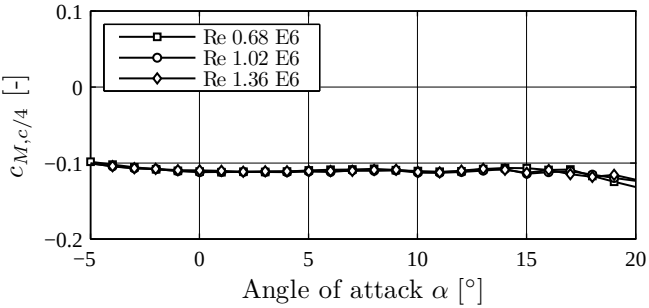

Figure 5.8: Influence of Reynolds number on moment coefficient; NACA 64_3618 rigid, $c = 0.5\,\mathrm{m}$, $V_\infty = 20\,\mathrm{m/s}$, $V_\infty = 30\,\mathrm{m/s}$, $V_\infty = 40\,\mathrm{m/s}$;

5.2.2 Flap Characteristics

Prior to introducing the effects of the passive camber change, the airfoil characteristics with fixed flap deflection were measured, because it is essential to define the contribution of each device. Three configurations are tested: pure leading-edge flap deflections, pure trailing-edge flap deflections and combined flap deflections.

Leading-Edge Flap

Figure 5.9 shows the influence of a $\pm 5°$ deflected leading-edge flap on the force and moment coefficients. The lift coefficient for an airfoil with leading-edge flap deflection of $-5°$ is lower in the attached flow region as compared to the original airfoil. Before the flow starts to separate, the lift coefficient of the $-5°$ flap deflection crosses the curves of the other two and reaches the highest lift coefficient. This is a typical characteristic for leading-edge devices as one can see in the diagrams presented by Hoerner and Borst (1985) in chapter VI. It is interesting to see in Figure 5.10 that the levels of the moment coefficients change slightly but still remain more or less constant over the entire angle of attack range.

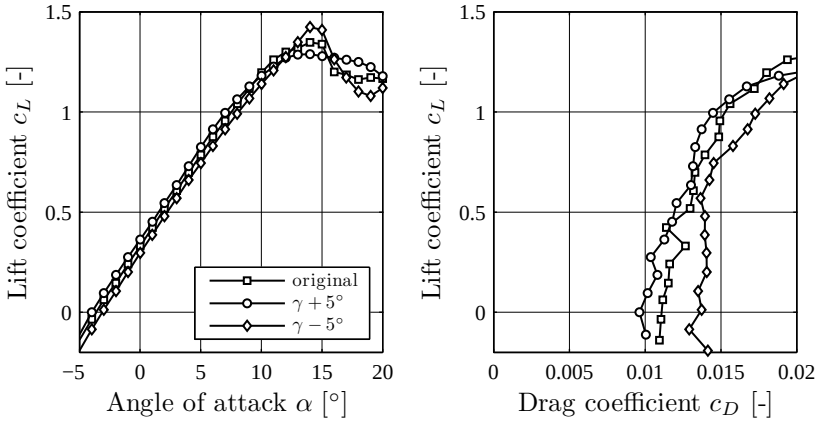

Figure 5.9: Influence of fixed leading-edge flap deflection on force coefficient; NACA 64_3618 rigid, $c = 0.5\,\text{m}$, $V_\infty = 40\,\text{m/s}$, $Re = 1.36\,\text{E6}$;

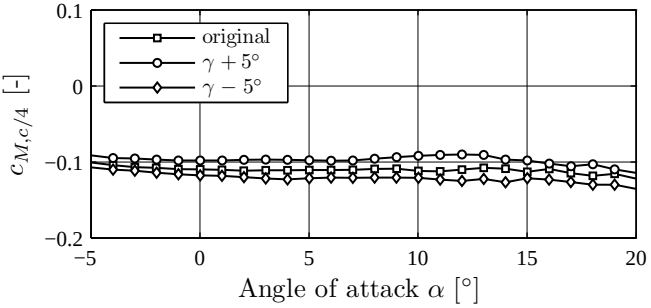

Figure 5.10: Influence of fixed leading-edge flap deflection on moment coefficient; NACA 64_3618 rigid, $c = 0.5\,\mathrm{m}$, $V_\infty = 40\,\mathrm{m/s}$, $Re = 1.36\,\mathrm{E6}$;

Trailing-Edge Flap

The influence of a $\pm 10°$ deflected trailing-edge flap is shown in Figure 5.11. As expected the influence is significant on the aerodynamic characteristics. For the decambered airfoil the lift slope is shifted vertically parallel to the original curve, this being characteristic for a trailing-edge flap. The difference in the lift coefficient is about $\Delta c_L = 0.6$. In contrast, when the flap is deflected downwards the lift increases, but the slope of the lift curve decreases. This is due to flow separation on the trailing-edge flap which can be seen from the pressure distribution and explains the drag increase. The moment around the airfoil changes magnitude, see Figure 5.12. The nose-down pitching moment for the decambered airfoil increases over the angle of attack, whereas the cambered airfoil moment decreases. This is in agreement with the decreasing lift curve slope.

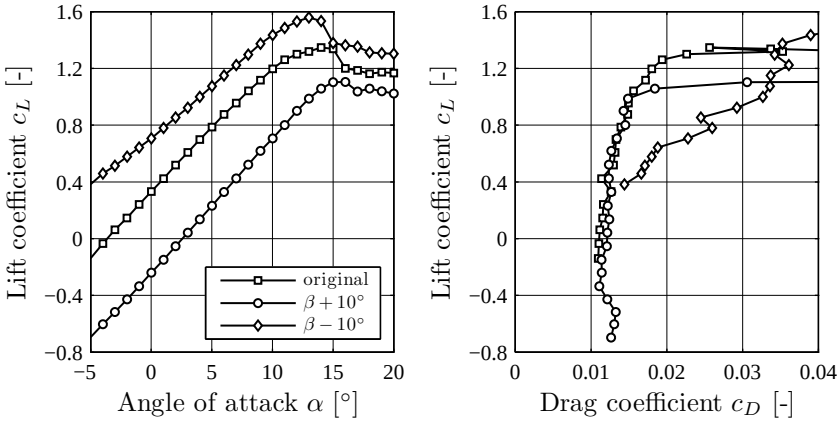

Figure 5.11: Influence of fixed trailing-edge flap deflection on force coefficient; NACA 64_3618 rigid, $c = 0.5\,\mathrm{m}$, $V_\infty = 40\,\mathrm{m/s}$, $Re = 1.36\,\mathrm{E6}$;

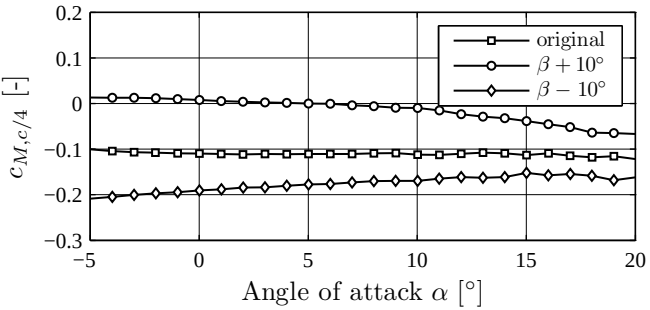

Figure 5.12: Influence of fixed trailing-edge flap deflection on moment coefficient; NACA 64_3618 rigid, $c = 0.5\,\mathrm{m}$, $V_\infty = 40\,\mathrm{m/s}$, $Re = 1.36\,\mathrm{E6}$;

Leading and Trailing-Edge Flap

The results for the configuration of deflected leading and trailing-edge flaps are displayed in Figure 5.13 and Figure 5.14. The lift slopes are nearly identical to those obtained for pure trailing-edge flap deflections. A difference is apparent in the drag coefficient, which is now increased over the entire range.

From these results it can be concluded that the trailing-edge flap has a significant impact on the lift. This was expected and is a well-known effect. For the present study it is important to know how the leading-edge flap influences the lift. It can be concluded that the leading-edge flap does not contribute significantly to the force change if flap angles less than $\pm 5°$ are considered. The main idea of the present concept is to transfer the pressure forces from the leading edge to the trailing edge. The leading-edge flap can therefore be seen as an actuator for the trailing-edge flap. Consequently, it is beneficial that the presence of the actuator does not cause any aerodynamic disadvantages.

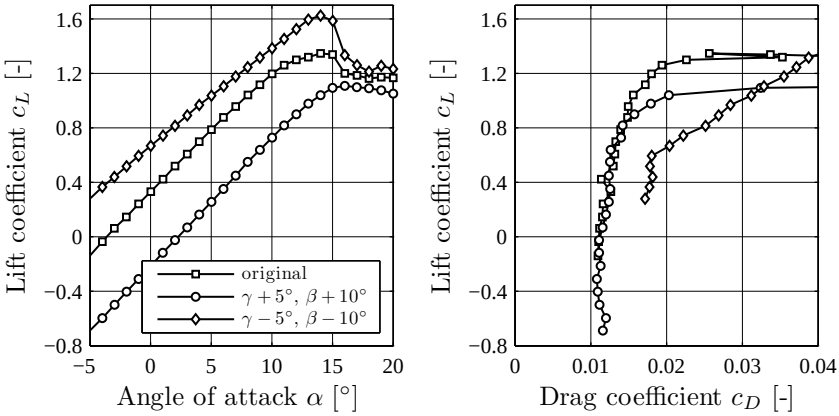

Figure 5.13: Influence of fixed leading and trailing-edge flap deflection on force coefficient; NACA 64_3618 rigid, $c = 0.5\,\mathrm{m}$, $V_\infty = 40\,\mathrm{m/s}$, $Re = 1.36\,\mathrm{E6}$;

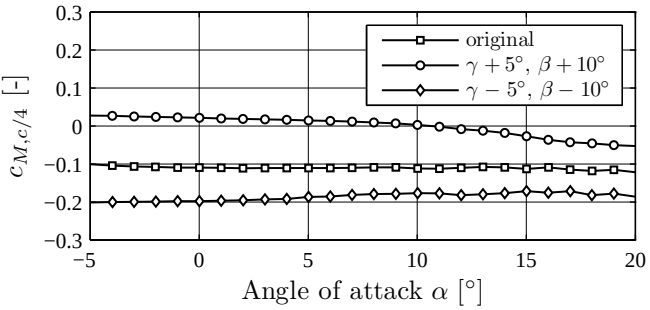

Figure 5.14: Influence of fixed leading and trailing-edge flap deflection on moment coefficient; NACA 64_3618 rigid, $c = 0.5\,\mathrm{m}$, $V_\infty = 40\,\mathrm{m/s}$, $Re = 1.36\,\mathrm{E6}$;

5.3 Flexible Airfoil

This section presents the conclusions obtained for the parametric study of the flexible airfoil. The results presented here will indicate the dominating parameters and will characterise the airfoil concept at quasi-steady conditions.

5.3.1 Influence of Velocity

Each polar was measured for three velocities. It is apparent that the velocity influences the loads significantly since the dynamic pressure is dependent on the velocity square. The diagrams in Figure 5.15 are of major importance and are considered first.

The left diagram shows the normal force read from the balance in Newton. The right diagram shows the normal coefficient from an integration of the pressure. The solid symbols indicate the rigid airfoil, whereas the open symbols indicate the flexible airfoil.

For a velocity $V_\infty = 40\,\mathrm{m/s}$ the normal force increases with increasing angle of attack until the airfoil separates (solid circles). The normal force for $V_\infty = 20\,\mathrm{m/s}$ is in equal measure smaller (solid squares). Additionally, if the coefficients are calculated with the respective dynamic pressure the obtained curves are the same since Reynolds number effects do not arise

as has already been seen in the previous section.

A preload moment of $M_0 = 10\,\mathrm{Nm}$ has been applied to the leading edge of the flexible airfoil by pretension of the spring at constant $k_\gamma = 30\,\mathrm{Nm/rad}$. The coupling ratio is $n = 3$. The stoppers were adjusted to: $\gamma_{max} = 6.3°$, $\gamma_{min} = -4.1°$, $\beta_{max} = 17.7°$, $\beta_{min} = -13.5°$. One can see that the coupling ratio is not exactly $n = 3$ and the maximum deflections in both direction are not identical.

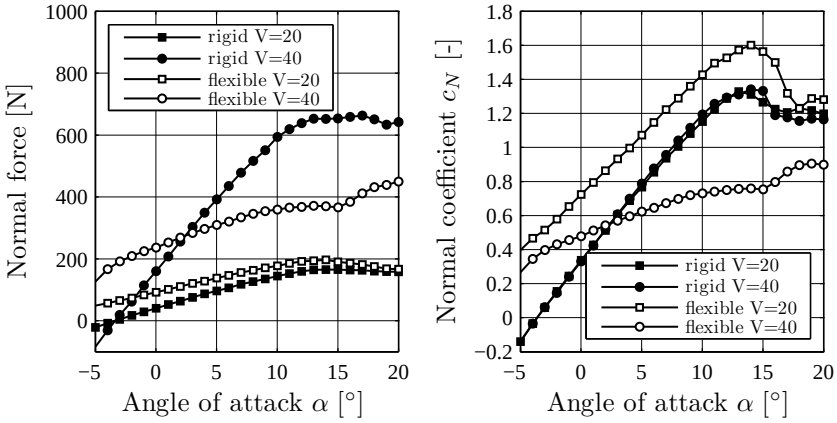

Figure 5.15: Influence of freestream velocity on normal force and coefficient; NACA 64_3618, $n = 3$, $k_\gamma = 30\,\mathrm{Nm/rad}$, $M_0 = 10\,\mathrm{Nm}$, $c = 0.5\,\mathrm{m}$;

First the case of $V_\infty = 40\,\mathrm{m/s}$ is considered. At low angle of attack ($\alpha = -5° \rightarrow 3°$) the preload moment is higher compared to the aerodynamic moments acting on the flaps. That means the airfoil has an increased camber line and produces more lift compared to the rigid airfoil. This can also be seen in Figure 5.16 where the leading-edge flap angle γ is given versus angle of attack. Below $\alpha = 3°$ the flap angle is negative. If the angle of attack increases above 3° the airfoil decambers further, since the aerodynamic moments increase. The flap angle motion indicates a linear behavior. This in turns means that the absolut lift force is smaller compared to the rigid airfoil. For the present configuration the lift force

is nearly constant. This is due to the fact that the camber line decreases until the flap deflection is limited by the stoppers. This takes place at approximately $\alpha = 15°$; the leading-edge flap is then deflected about $\gamma = 6.3°$. If the normal coefficient is calculated for this force curve one sees that it exhibits the same slope.

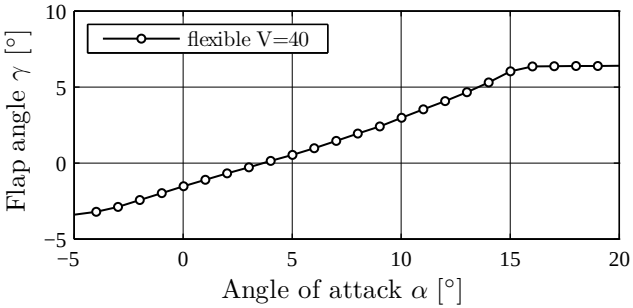

Figure 5.16: Leading-edge flap angle γ for $V_\infty = 40\,\mathrm{m/s}$; NACA 64_3618, $n = 3$, $k_\gamma = 30\,\mathrm{Nm/rad}$, $M_0 = 10\,\mathrm{Nm}$, $c = 0.5\,\mathrm{m}$;

Secondly, the case of $V_\infty = 20\,\mathrm{m/s}$ is considered. As expected the aerodynamic moments are much smaller compared to the preload moment. This means that the airfoil has an increased camber line during most of the time, resulting in a higher normal force (light square) as seen in the left of Figure 5.15. However, the difference is not significant. A different picture occurs if one compares the normal coefficient in the right diagram. It clearly shows that the airfoil produces more lift. The airfoil indicates the same characteristics as for the cambered airfoil with fixed flaps.

Figure 5.17 shows the drag coefficient for all configurations. One sees that the drag is smaller for the decambered airfoil, but this cannot be finally concluded because of the uncertainty of the measurement. Yet, the drag increases significantly for the cambered airfoil at $V_\infty = 20\,\mathrm{m/s}$. In the range $\alpha = 5° \rightarrow 10°$ the drag is about 5 times higher.

Furthermore, it is important to notice the changes in the pitching moment around the airfoil. This is shown in Figure 5.18. The pitching moment remains constant for the cambered airfoil, as expected. But for the airfoil which constantly changes its camber line over the entire angle of attack range the pitching moment varies. It changes from a nose-down

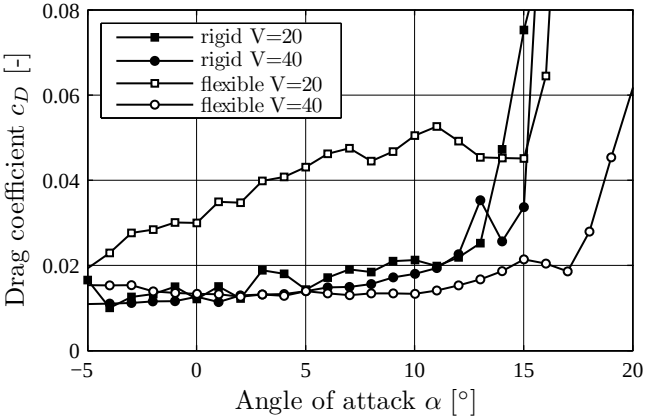

Figure 5.17: Influence of freestream velocity on drag coefficient; NACA 64_3618, $n = 3$, $k_\gamma = 30\,\mathrm{Nm/rad}$, $M_0 = 10\,\mathrm{Nm}$, $c = 0.5\,\mathrm{m}$;

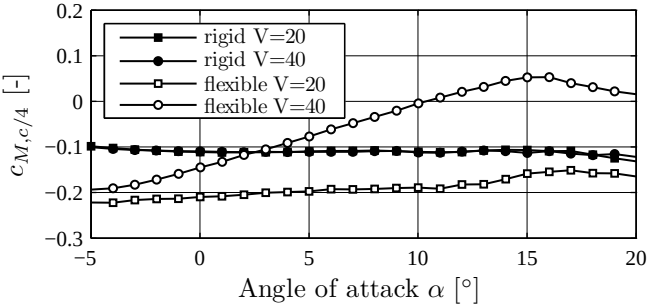

Figure 5.18: Influence of freestream velocity on moment coefficient; NACA 64_3618 , $n = 3$, $k_\gamma = 30\,\mathrm{Nm/rad}$, $M_0 = 10\,\mathrm{Nm}$, $c = 0.5\,\mathrm{m}$;

moment at low angle of attack to a nose-up moment at higher angles of attack. This means that the aerodynamic center moves from the aft part to the front part of the airfoil.

The above results characterize the principal idea of the novel concept. The parameters have not been optimized for a specific application or objective function. It is the primary goal of this study to identify possibilities how those curves may be manipulated by certain parameters. This will be presented in the next sections.

5.3.2 Influence of Preload Moment

Figure 5.19 shows the normal force for different preload moments. The velocity is $V_\infty = 40\,\mathrm{m/s}$. Moments in the range of $M_0 = 2\,\mathrm{Nm} \rightarrow 10\,\mathrm{Nm}$ have been applied by different elongations of the spring with constant $k_\gamma = 30\,\mathrm{Nm/rad}$. It can be explicitly seen that with increasing moment the mean normal force increases. The slope does not change. The reason is that for higher preload moments higher aerodynamic moments are required before the flaps start to change the camber line.

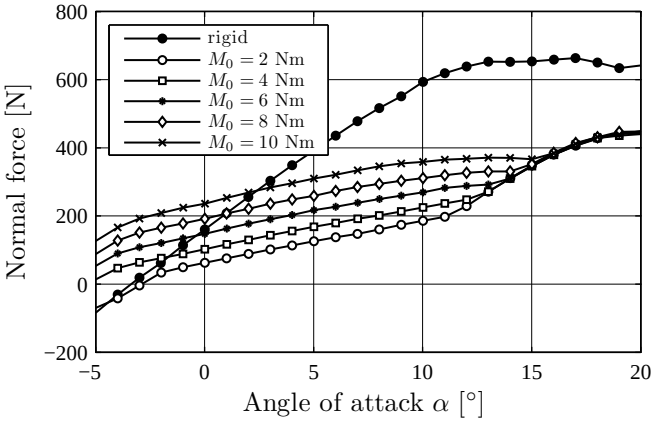

Figure 5.19: Influence of preload moment on normal force; NACA 64_3618, $n = 3$, $k_\gamma = 30\,\mathrm{Nm/rad}$, $c = 0.5\,\mathrm{m}$, $V_\infty = 40\,\mathrm{m/s}$;

There are different intersection points with the flexible and rigid curves. These intersections are where the flexible airfoil produces the same lift as the rigid airfoil. This point is called the design angle of attack. Above this angle the flexible airfoil produces less lift, below this angle it produces more lift compared to the rigid airfoil. Furthermore, it reveals that the elastic region is also effected by the preload moment. For lower preload moments the flaps reach the stoppers earlier. Once the flaps are fixed in the end position all lift curves converge to the same curve.

Figure 5.20 shows that this behavior is independent of the spring stiffness. To apply the same preload moment with a less stiff spring, higher elongations are necessary.

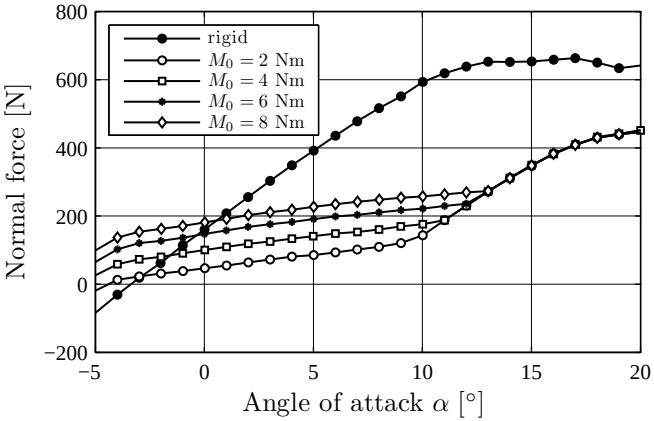

Figure 5.20: Influence of preload moment on normal force; NACA 64_3618, $n = 3$, $k_\gamma = 10\,\mathrm{Nm/rad}$, $c = 0.5\,\mathrm{m}$, $V_\infty = 40\,\mathrm{m/s}$;

5.3.3 Influence of Spring Stiffness

The influence of the spring stiffness on the lift-curve slope is presented in Figure 5.21. Taking the curves into consideration it is apparent that the slope changes as the stiffness decreases.

According to this finding it is interesting to explore how far the lift-curve slope can be decreased. In other words to examine what happens

when the stiffness goes to zero. Therefore, a test run without a spring was conducted. The results are shown in Figure 5.21 (open circles). Since no spring is used it is also not possible to apply a preload moment. That is the reason why the mean lift is small, which in turn demonstrates that this is not a case of practical interest. However, the additional slope reduction compared to lift-curve slope of the lower stiffness is insignificant. This means with an optimized stiffness constant one might obtain best results if the aim is to keep the loads constant.

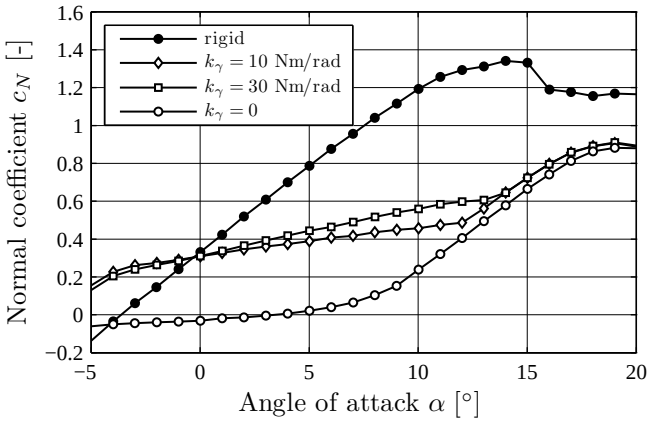

Figure 5.21: Influence of spring stiffness k_γ on normal coefficient; NACA 64_3618, $n = 3$, $M_0 = 6\,\mathrm{Nm}$, $c = 0.5\,\mathrm{m}$, $V_\infty = 40\,\mathrm{m/s}$;

The above statements also hold for the velocity $V_\infty = 30\,\mathrm{m/s}$, as pictured in Figure 5.22. It can be seen that the curve slope decreases when it passes the design angle of attack.

In addition to the fact that the design angle of attack determines the preload moment, it is vital to define a design velocity. This issue will be the topic of chapter 7. For a wind turbine including modern control strategies several scenarios are possible. The discussion in chapter 7 will start with the assumption that a load alleviation concept of this type should be optimized for the conditions and loads at rated speeds. The effects and respective load reductions will then be discussed.

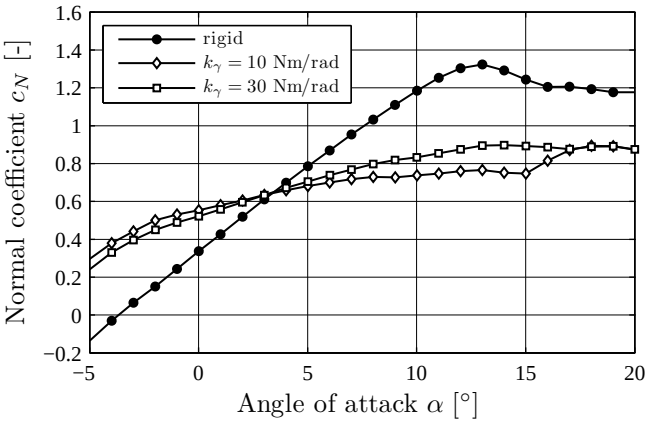

Figure 5.22: Influence of spring stiffness k_γ on normal coefficient; NACA 64_3618, $n = 3$, $M_0 = 6\,\mathrm{Nm}$, $c = 0.5\,\mathrm{m}$, $V_\infty = 30\,\mathrm{m/s}$;

5.3.4 Influence of Coupling Ratio

The next parameter investigated was the coupling ratio n. The experimental setup realizes ratios up to 5. From the preliminary design study it was learned that ratios above 4 do not improve the obtained load fluctuation reduction any further.

To separate the influence of the coupling ratio from any other parameter, the results presented in Figure 5.23 are obtained omitting the spring; hence no preload moment is applied. Coupling ratios from 1, 2 and 3 are considered. The coupling ratio has the same effect as the stiffness, namely the adjustment of the lift slope. The curve for $n = 3$ is the curve which has already been presented in Figure 5.21. If the coupling ratio is reduced to $n = 2$ one can see that the slope becomes negative over a certain range of angle of attack ($-5° \rightarrow 5°$). Furthermore, the slope for a coupling ratio of $n = 1$ exhibits a much steeper negative slope albeit over a smaller range of angle of attack ($-2° \rightarrow 1°$).

The reason for this behavior cannot be conclusively identified. However, before discussing possible reasons one should consider the leading-edge flap angles in Figure 5.24. The elastic range of the airfoil is much smaller for $n = 1$. It becomes apparent that the maximum deflections are

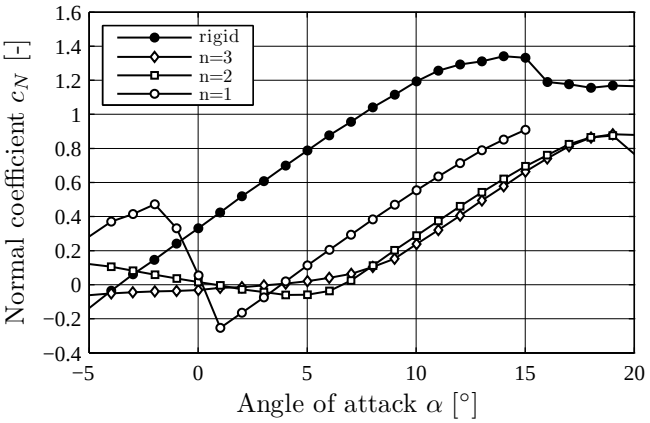

Figure 5.23: Influence of coupling ratio n on normal coefficient, no spring; NACA 64_3618, $c = 0.5\,\mathrm{m}$, $V_\infty = 40\,\mathrm{m/s}$;

different. Due to the mechanical construction the maximum deflection of the leading-edge flap is determined by $\beta_{max,min}/n$. Hence if the coupling ratio increases the deflections decrease.

It was first assumed that the higher deflections of the leading edge were responsible for achieving a negative lift curve slope but even when the leading-edge flap is limited to $\beta_{max,min}/3$ one can obtain negative lift curve slopes. Negative lift curve slopes usually occur when the flow separates. A detailed analysis of the pressure distribution leads to the conclusion that it makes sense in comparison with the obtained lift coefficients in Figure 5.23. At about $\alpha = 0°$ the lift coefficient is zero, which is also indicated by the pressure distribution. It will be seen in the next section that the potential flow model is able to predict these negative lift curve slopes as well, although this model does not incorporate flow separation. The numerical model showed the same behavior for a NACA 0012 and for computations where a small preload moment was applied.

Taking these elements into consideration it can only be stated generally that there is a relation between the angle of attack and the camber line for which the lift curve turns negative. However, these results indicate the sensitive interaction among the influencing parameters such as stiffness,

airfoil shape and coupling ratio.

Last but not least it should be mentioned that the airfoil flaps move very smoothly although no preload moment is applied. This indicates once more the benefit of the coupling mechanism in terms of stability. Again, the coupling mechanism transfers the leading-edge angles n times to the trailing-edge flap, contrary the aerodynamic moment of the trailing-edge flap is transferred n times to the leading-edge hinge point. That means under certain pressure distributions the trailing-edge flap actuates the leading-edge flap.

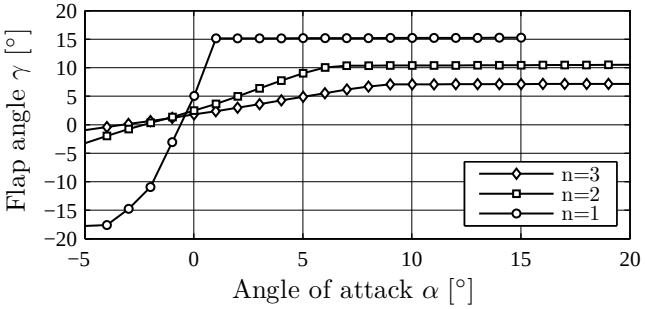

Figure 5.24: Influence of coupling ratio n on leading-edge flap angle γ, no spring; NACA 64_3618, $c = 0.5\,\mathrm{m}$, $V_\infty = 40\,\mathrm{m/s}$;

5.4 Comparison with Theory

The experimental results of the previous section have confirmed the basic working concept of the passively cambered airfoil. It is possible to adjust the lift force passively by load-dependent flap deflections. The influence of each parameter is identified and quantified. However, an optimization of the setup has not yet been performed. For the following investigation and for future designs of such a flexible airfoil it is necessary to have a numerical model which is able to predict the various effects on the lift.

The aeroelastic model used in the present study determines the pressure distribution from a potential flow formulation, in which flow separation and boundary layer effects are not captured. Nevertheless, reduced model complexity is a big advantage when parameter studies need to be carried out.

A further objective of the present investigation is therefore to confirm the validity of the potential flow model. The design of the wing was determined using Eq. 2.56. Since the experiment was carried out under quasi-steady conditions, measurements at every angle of attack were performed only after the flow has settled. The equation of motion is therefore replaced by a simple moment balance around the leading-edge hinge point:

$$\sum M_i^l = M_B - nM_D - M_0 = 0 \tag{5.5}$$

where the moments are defined in Figure 2.7 and $M_0 (= k_\gamma \gamma_0)$ is the preload moment. The solution is then obtained by an iteration scheme until convergence is reached.

Pressure Distribution

First a comparison of the pressure distribution is presented. At the beginning of this chapter it was stated that the trailing vortex causes an induced angle of attack. The computed pressure in Figure 5.25 to Figure 5.30 is related to the effective angle of attack α_{eff} (Eq. 5.4) and is given in each figure caption. These pressure distributions are compared to the measured angle of attack. Generally, the results agree satisfactorily when one keeps the comparison of Figure 5.3 in mind.

At $\alpha = -2°$ the pressure on the suction side agrees well with the theory. The measured data show a small separation at the trailing edge. A

discrepancy can be seen on the pressure side of the airfoil. The measured pressure values are significantly lower in the region of the leading edge and slightly lower between 20% and 60% chord. It seems that the flow is more accelerated in the experiment compared to the computations. This behavior occurs also for $\alpha = 0°$ and $\alpha = 2°$

At $\alpha = 4°$, $6°$ and $8°$ the situation changes. Here the pressure on the pressure side agrees well. The results are in better agreement with the inviscid computations rather than with the viscous computations. From this finding it can be concluded that the leading edge has a different shape compared to the airfoil coordinates used in the computations. This is plausible since a manufacturing imperfection required some rework on the airfoil nose. It might be the reason that the different curvature of the nose causes the different flow acceleration.

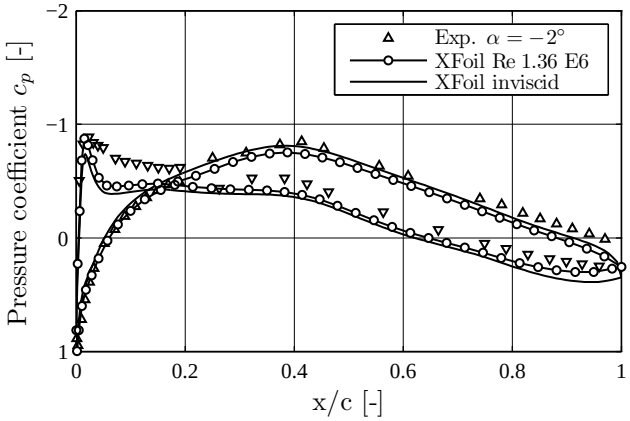

Figure 5.25: Comparison of measured pressure distribution ($\triangle \equiv$ upper side; $\triangledown \equiv$ lower side) with XFoil computations; $\alpha_{eff} = -2.5°$; NACA 64_3618, $c = 0.5\,\mathrm{m}$, $V_\infty = 40\,\mathrm{m/s}$, $Re = 1.36\,\mathrm{E6}$;

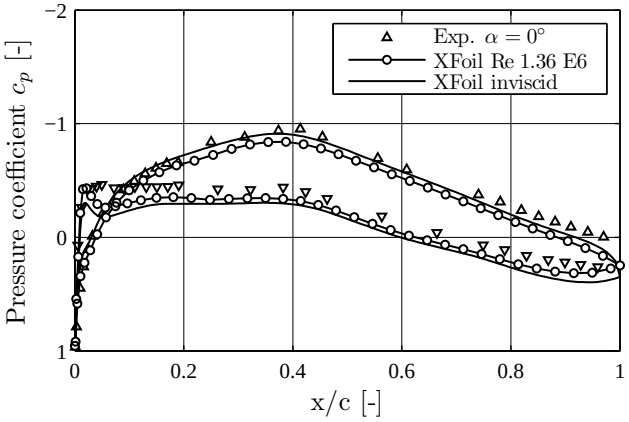

Figure 5.26: Comparison of measured pressure distribution ($\triangle \equiv$ upper side; $\bigtriangledown \equiv$ lower side) with XFoil computations; $\alpha_{eff} = -1.2°$; NACA 64_3618, $c = 0.5\,\mathrm{m}$, $V_\infty = 40\,\mathrm{m/s}$, $Re = 1.36\,\mathrm{E6}$;

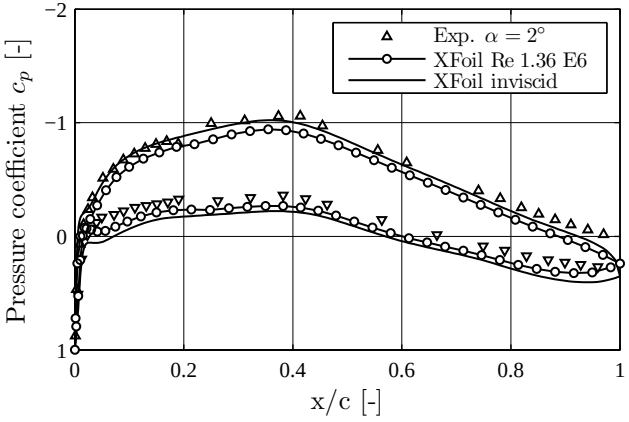

Figure 5.27: Comparison of measured pressure distribution ($\triangle \equiv$ upper side; $\bigtriangledown \equiv$ lower side) with XFoil computations; $\alpha_{eff} = -0.2°$; NACA 64_3618, $c = 0.5\,\mathrm{m}$, $V_\infty = 40\,\mathrm{m/s}$, $Re = 1.36\,\mathrm{E6}$;

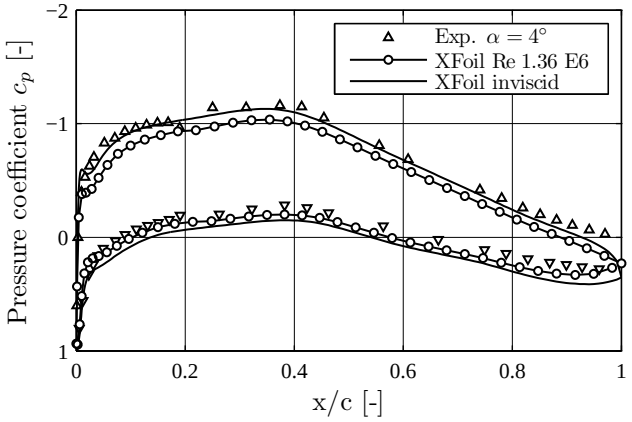

Figure 5.28: Comparison of measured pressure distribution ($\triangle \equiv$ upper side; $\triangledown \equiv$ lower side) with XFoil computations; $\alpha_{eff} = 1.5°$; NACA 64_3618, $c = 0.5\,\mathrm{m}$, $V_\infty = 40\,\mathrm{m/s}$, $Re = 1.36\,\mathrm{E6}$;

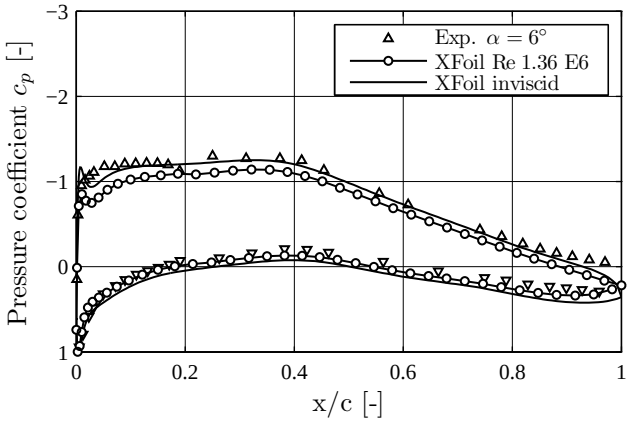

Figure 5.29: Comparison of measured pressure distribution ($\triangle \equiv$ upper side; $\triangledown \equiv$ lower side) with XFoil computations; $\alpha_{eff} = 2.9°$; NACA 64_3618, $c = 0.5\,\mathrm{m}$, $V_\infty = 40\,\mathrm{m/s}$, $Re = 1.36\,\mathrm{E6}$;

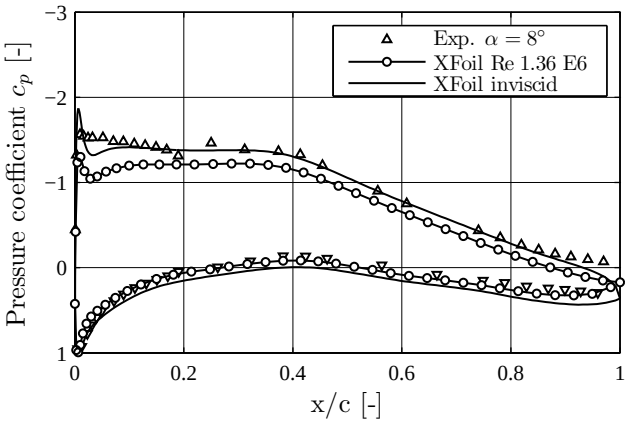

Figure 5.30: Comparison of measured pressure distribution ($\triangle \equiv$ upper side; $\triangledown \equiv$ lower side) with XFoil computations; $\alpha_{eff} = 4.3°$; NACA 64_3618, $c = 0.5\,\mathrm{m}$, $V_\infty = 40\,\mathrm{m/s}$, $Re = 1.36\,\mathrm{E6}$;

Fixed Flaps

Figure 5.31 shows the comparison of the fixed flap configuration with the numerical model. The experimental lift coefficients have been corrected by the induced angle of attack.

It can be seen that the decambered airfoil is in good agreement with the computations.

As expected the lift computed by the potential flow model for the case where the flaps are deflected down is much higher compared to the experimental result. This is reasonable since in the experiments the flow separates on the flaps.

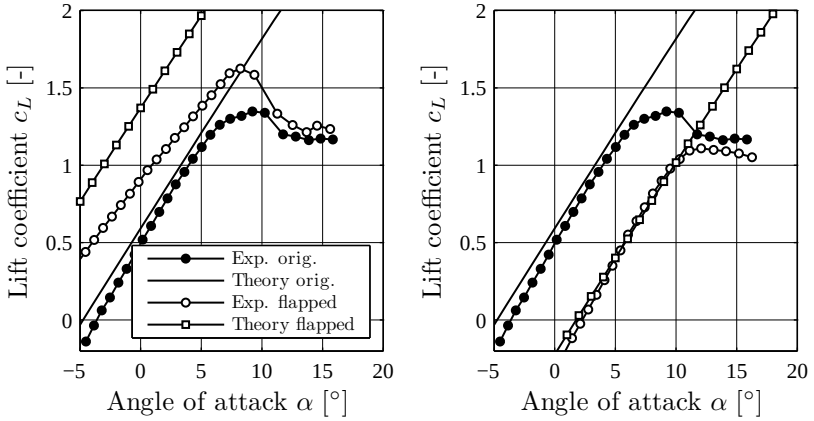

(a) $\gamma - 5°$, $\beta - 10°$ **(b)** $\gamma + 5°$, $\beta + 10°$

Figure 5.31: Fixed flap position: Comparison of theory with experiment; NACA 64_3618, $c = 0.5\,\mathrm{m}$;

Freestream Velocity

Figure 5.32 compares the numerical prediction (square symbols) with the experimental results presented in section 5.3.1. The agreement is not good and this has several reasons.

The determination of the spring constant $k_\gamma = 30\,\mathrm{Nm/rad}$ has been achieved by measuring the elongation of the translatory spring used in the experiment. This has then been recomputed to a torsional spring constant. This procedure involves some uncertainties.

Furthermore, the pressure difference of the calculated pressures is higher compared to the measured pressure. This results in higher forces and explains the fact that the computed lift-curve slope for $V_\infty = 40\,\mathrm{m/s}$ is lower. However, the trends and effects are predicted by the model.

The results for $V_\infty = 20\,\mathrm{m/s}$ show the same behavior as for the fixed flaps. The lift coefficient is too high. At $\alpha = 1°$ and a lift coefficient c_L of 1.6 the airfoil flaps start to change the airfoil camber. This result is theoretically correct but of course physically not realistic.

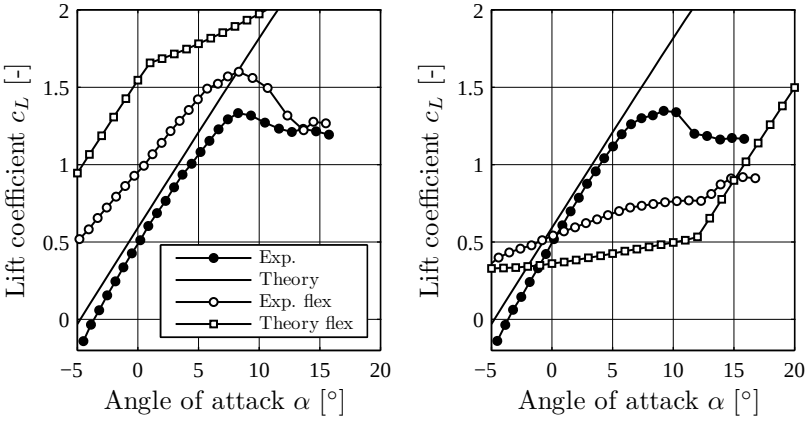

(a) $V_\infty = 20$ m/s **(b)** $V_\infty = 40$ m/s

Figure 5.32: Comparison of theory with experiment; NACA 64_3618, $n = 3$, $k_\gamma = 30\,\mathrm{Nm/rad}$, $M_0 = 10\,\mathrm{Nm}$, $c = 0.5\,\mathrm{m}$;

Preload Moment

Figure 5.33 shows the influence of different preload moments. This figure does not need any further explanations. The model is able to predict the same trend as observed in the experimental results.

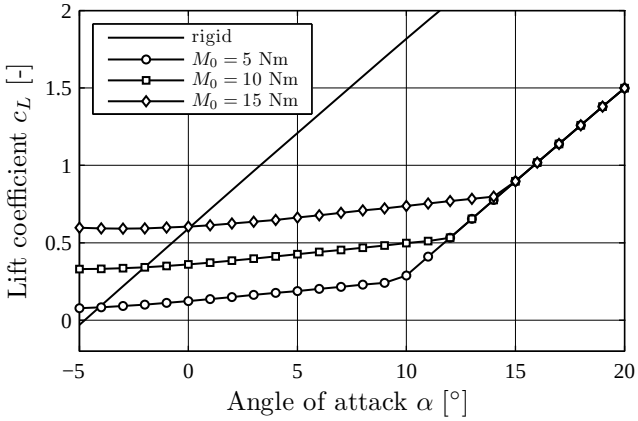

Figure 5.33: Numerical prediction of experimental case, no comparison; NACA 64_3618, $n = 3$, $k_\gamma = 30\,\mathrm{Nm/rad}$, $V_\infty = 40\,\mathrm{m/s}$, $c = 0.5\,\mathrm{m}$;

Spring Stiffness

The same holds for the influence of different spring constants. Figure 5.34 shows that the numerical model indicates the same behavior as the experimental results. The stiffness of the spring can be used to adjust the lift-curve slope.

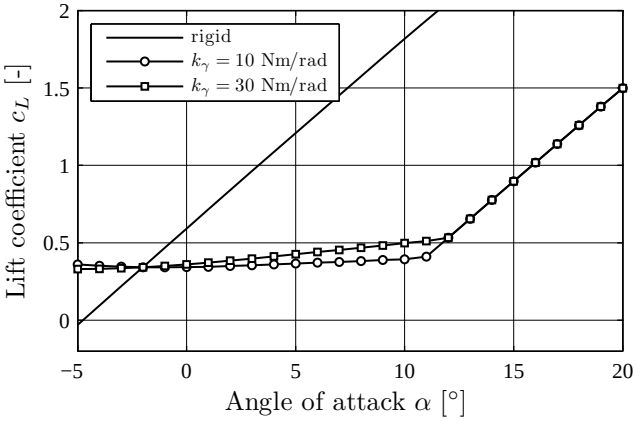

Figure 5.34: Numerical prediction of experimental case, no comparison; NACA 64_3618, $n = 3$, $V_\infty = 40\,\mathrm{m/s}$, $c = 0.5\,\mathrm{m}$;

Coupling Ratio

The coupling ratio can be used to adjust the lift-curve slope. Figure 5.35 shows on the left the lift curve for the case when the leading-edge flap angles are limited to the maximum of the $n = 3$ case. The right diagram presents the results in which the maximum leading-edge flap angles are different for each case. However, the model predicts negative lift curve slops for coupling ratios smaller 2. This indicates that this effect is not related to flow separation.

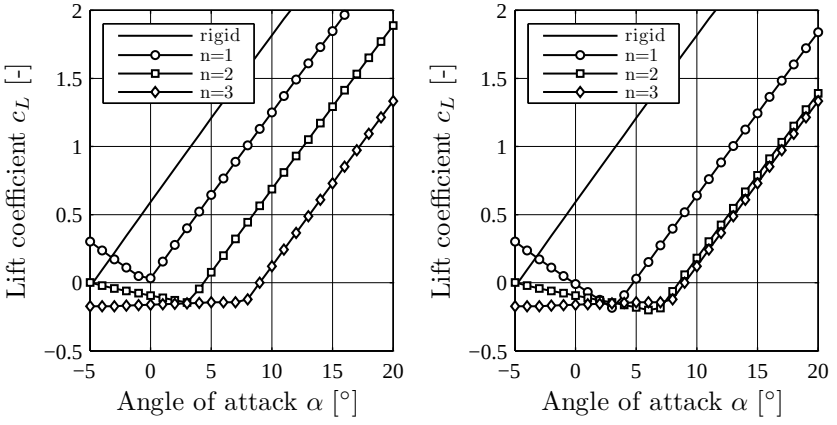

(a) γ fixed to n=3 case **(b)** γ free

Figure 5.35: Numerical prediction of experimental case, no comparison; NACA 64_3618, $c = 0.5\,\mathrm{m}$;

Chapter 6

Results - Enhanced Models

The numerical and experimental investigations in the previous chapters have only considered the flap motion. The remaining wing was assumed to be rigid and fixed with respect to the inertial frame of reference. However, a wind turbine rotor blade undergoes large deflections, affecting the dynamics of the flap motion. To evaluate the influence on the airfoil performance the contribution of blade flexibility will be addressed in this section. To capture the bending and torsional flexibility of the blade the airfoil model is extended to include a translatory and torsional spring as described in section 2.2.

In previous studies it was assumed that a reduction in load amplitudes can be directly translated into an increase of the fatigue limits (durability). The main focus in this section will be the bending deflection of the rotor blade, i.e. the q_1 degree of freedom. Therefore, the load reduction is now defined by

$$LR = 1 - \frac{\text{std}\,(q_1)_{\text{3DOF}}}{\text{std}\,(q_1)_{\text{2DOF}}} \tag{6.1}$$

where 2DOF is related to the airfoil with a rigid camber line undergoing heaving and pitching motions only, and 3DOF means the flapped airfoil which can also experience deflections q_3.

6.1 Parameter Space

The additional parameters required to model this situation are given in Table 6.1. The moment of inertia and the mass of each flap have been estimated via CAD software. It was assumed that the flaps are made of fiberglass and the rotation hinge tube is made of carbon fiber. The bending and torsional eigenfrequency have been taken from Kallesø (2006) and Bergami and Gaunaa (2010). From the given eigenfrequencies the stiffness k_h and k_θ are computed. The corresponding heaving deflection for a steady load at rated wind speed has been compared to the static deflection at a spanwise position of 75% of the NREL blade (Jonkman et al., 2009) and is in good agreement. Nevertheless, an error is unavoidable when defining an equivalent stiffness for the entire bending behavior of the blade. Additionally, structural damping of 1% is applied to the heaving and pitching motion. For all simulations it is assumed that the flaps are mass balanced, i.e. the center of gravity of the flaps is identical to the rotation point. The onflow velocity in the horizontal direction to the airfoil is $v_x = 60\,\mathrm{m/s}$. This corresponds to a typical angular velocity in the outer part of a MW wind turbine.

Table 6.1: Structural parameters for the airfoil section

Description	Parameter	Value
mass main wing	m_f	$22\,\mathrm{kgm^{-1}}$
mass leading-edge flap	m_l	$12\,\mathrm{kgm^{-1}}$
mass trailing-edge flap	m_l	$10\,\mathrm{kgm^{-1}}$
moment of inertia main wing	θ_f	$0.56\,\mathrm{kgm}$
moment of inertia leading-edge flap	θ_l	$0.12\,\mathrm{kgm}$
moment of inertia trailing-edge flap	θ_t	$0.1\,\mathrm{kgm}$
bending eigenfrequency	$\omega_h/2\pi$	$1\,\mathrm{Hz}$
torsional eigenfrequency	$\omega_h/2\pi$	$10\,\mathrm{Hz}$
chord	c	$1\,\mathrm{m}$
center of gravity behind elastic axis	s_{fx}	$0.1\,\mathrm{m}$
elastic axis from leading edge	x_p^*	$0.3\,\mathrm{m}$

6.2 Steady Aerodynamics

According to a definition given by Leishman (2006, p. 427) a reduced frequency k below 0.05 can be assumed to adhere to quasi-steady aerodynamics, where the frequency is related to the half-chord. The aeroelastic behavior of the flap motion was computed with the steady formulation of the Hess-Smith panel method. The frequency of the sinusoidal change of the velocity v_z was chosen to meet a reduced frequency of $k = 0.01$.

For the DOF2 and DOF3 case this velocity change is pictured in Figure 6.1. The wind speed and its fluctuation is again considered through a change in the heaving velocity $\dot{h}(t)$. The heaving deflection q_1 of the airfoil is plotted versus time. The initial results have been omitted since in this period the aerodynamics settle and reach an equilibrium with the structural deflections.

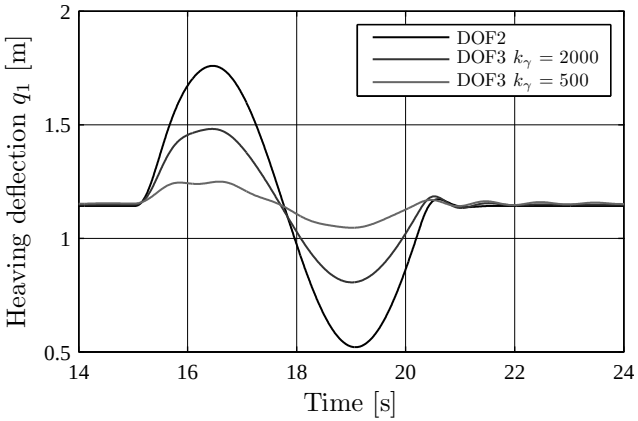

Figure 6.1: Influence of stiffness k_γ on heaving motion q_1 for $k = 0.01$ assuming steady aerodynamics; NACA 64_3618; $v_x = 60\frac{\text{m}}{\text{s}}$; $x_l^* = 0.2$; $x_t^* = 0.7$; $d_\beta = 1\frac{\text{Nms}}{\text{rad}}$; $n = 3$

After a total time of 15 seconds the velocity increase is applied, which means the relative flow angle seen by the airfoil increases. This in turns increases the loads. For the DOF2 case this results directly in an increase of the heaving deflection q_1. The motion follows then the sinusoidal change

in velocity. Additionally, the results of the flapped airfoil for two different spring stiffnesses k_γ are given. Once the loads increase the airfoil starts to decamber and reduces the generated lift. This can be seen in the reduced amplitudes of the heaving motion. As expected the heaving deflections become smaller when the torsional stiffness k_γ decreases. This is due to higher flap deflections.

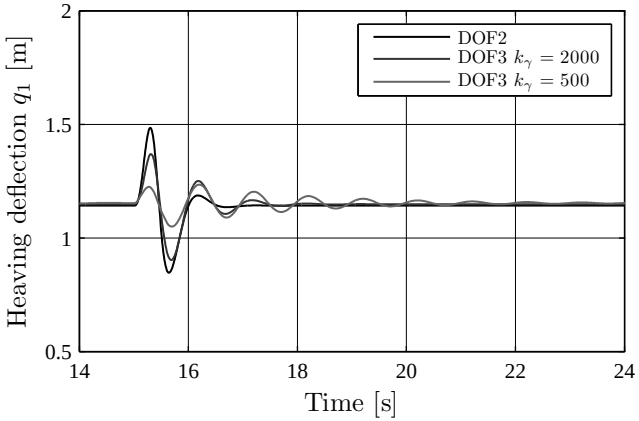

Figure 6.2: Influence of stiffness k_γ on heaving motion q_1 for $k = 0.1$ assuming steady aerodynamics; NACA 64_3618; $v_x = 60\frac{\mathrm{m}}{\mathrm{s}}$; $x_l^* = 0.2$; $x_t^* = 0.7$; $d_\beta = 1\frac{\mathrm{Nms}}{\mathrm{rad}}$; $n = 3$

As one can see in Figure 6.1 after the velocity change ends at about 21 seconds the heaving motion continues with small oscillations for the case with the lower flap stiffness. This would normally be unwanted. For a more detailed investigation of this effect the reduced frequency was increased to $k = 0.1$. The results are presented in Figure 6.2. The velocity change is again applied at 15 seconds and, since the frequency has increased, the period duration has decreased. Note, it is still assumed that the aerodynamics are steady. One can see that the oscillations increase for the $k_\gamma = 500\,\mathrm{Nm/rad}$ case. One reason for this behavior is the induced velocity due to the downstroke of the airfoil, preventing the airfoil from increasing its camber. This results in a lower lift force and the restoring force of the blade structure increases the deflection. Addition-

ally, it seems that this is supported by the fact that the frequencies of the excitation and flap motion become closer to one another. Although the maximum amplitudes have reduced the number of cycles have increased. A parametric study showed that the main improvement in reducing these oscillations can be obtained by increasing the flap stiffness. This can be seen from the curve for $k_\gamma = 2000\,\mathrm{Nm/rad}$. This in turn reduces the obtained load reduction. However, all degrees of freedom are damped and the system remains stable over the integration time for this parameter set. The assumption of steady aerodynamics will be evaluated in the next section.

A turbulent wind field with a turbulence intensity of 20% is now considered. The reference wind speed is $v_{z0} = 10\,\mathrm{m/s}$. The offset pitch angle is set to $\alpha_0 = -5°$. The method to generate a stochastic time series of a one-dimensional velocity component follows the description presented by Hansen (2008, pp. 147-151). As might be expected from the previous results, when a continuous change in angle of attack due to turbulence is considered the positive effects of the flapped airfoil increase. This is shown in Figure 6.3. The load reduction is $LR_{q_1} = 44\%$. The fluctuations of the lift coefficient in Figure 6.4 are higher. This is due to the fact that the lift coefficient includes the contribution of the pitching motion of the airfoil. A reduction of $LR_{c_L} = 44\%$ is obtained.

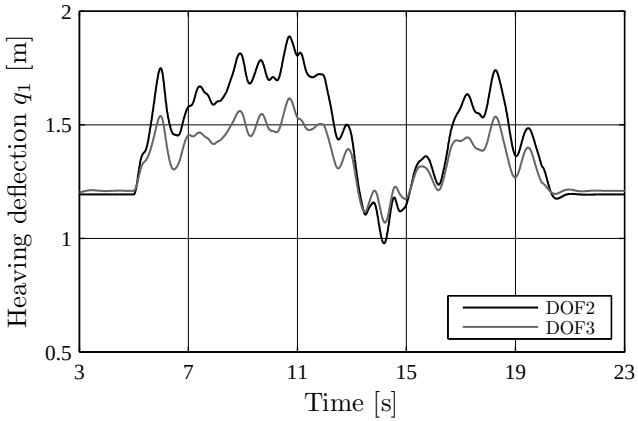

Figure 6.3: Influence of stiffness k_γ on heaving motion q_1 due to turbulence; NACA 64_3618; $v_x = 60\frac{\mathrm{m}}{\mathrm{s}}$; $x_l^* = 0.2$; $x_t^* = 0.7$; $d_\beta = 1\frac{\mathrm{Nms}}{\mathrm{rad}}$; $n = 3$

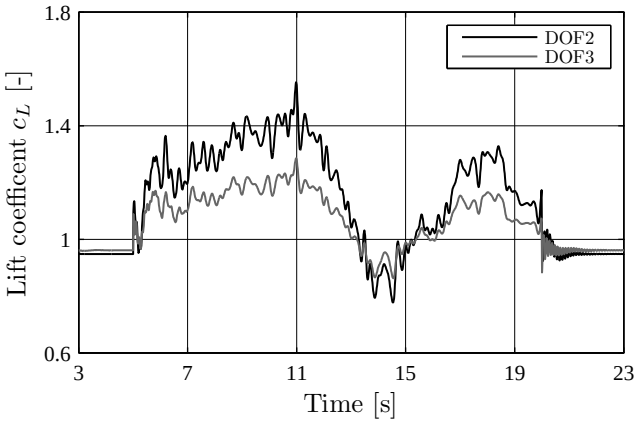

Figure 6.4: Influence of stiffness k_γ on lift coefficient c_l due to turbulence; NACA 64_3618; $v_x = 60\frac{\mathrm{m}}{\mathrm{s}}$; $x_l^* = 0.2$; $x_t^* = 0.7$; $d_\beta = 1\frac{\mathrm{Nms}}{\mathrm{rad}}$; $n = 3$

6.3 Outlook: Unsteady Aerodynamics

Although the structural model considers the necessary degrees of freedom for predicting flutter (pitch and heave), the aeroelastic study has assumed steady aerodynamics. From flutter calculations it is known that flutter speeds determined with steady aerodynamics are much lower compared to the ones obtained with unsteady aerodynamics, see Lobitz (2004). The shed vortices due to heaving and pitching motion cause a time and phase lag of the aerodynamic response, which influences the direction of the energy exchange between the fluid and the structure.

An estimation of this influence on the present computations is given in Figure 6.5. The extension of the Hess-Smith formulation, which incorporates a time varying wake, is used to compute the effect of the reduced frequency. The eigenfrequency of the torsional degree of freedom is 10 Hz. For a freestream velocity of $v_x = 60\,\mathrm{m/s}$ this corresponds to a reduced frequency k of 0.5, which requires unsteady computations. However, from Figure 6.5 it can be seen that for a sinusoidal pitching motion the lift amplitude reduces about 13% for the unsteady computation, but no phase shift occurs. This allows the conclusion that the simplification of steady

fluid forces is justifiable, especially in the light that the intention of the present study was not to determine the flutter limits but to explore by then the unknown behavior of the adaptive airfoil.

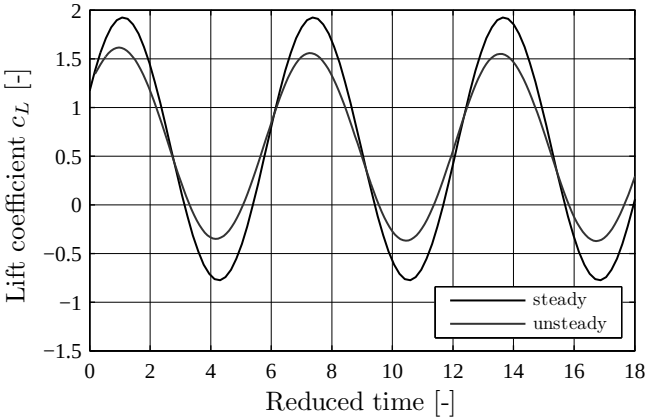

Figure 6.5: Comparison of steady and unsteady computation for a sinusoidal pitching motion of $k = 0.5$; NACA 64_3618;

Chapter 7

Turbine Simulation

Until here the investigation considered the flapped airfoil as a typical wing section, i.e. two-dimensionality was assumed. However, the primary goal of this study is to develop a concept for the alleviation of load fluctuations on wind turbines. The arising questions are subject of this chapter. The main focus is drawn to the root bending moment which is given by the integration of the distributed forces along the blade.

The design study in chapter 4 assumed a constant inflow velocity, i.e. the dynamic pressure was constant. The load alleviation was characterized by the reduction of lift coefficient fluctuations due to camber changes. A constant relative velocity can be assumed on a rotor blade in the outer part span sections where the tip rotational velocity is 6 to 9 times higher than the wind speed. Fluctuations of wind speed therefore result in velocity magnitude changes of only a few percent.

However, modern MW wind turbines are operated with control strategies, which adapt the rotational speed in the partial load region (below rated speed) and adjust the blade pitch angle over the full load range. This means the relative velocity measured by a wing section changes rather significantly in the partial load region. It was already seen in the experimental results that the influence of the velocity has a major impact on the final camber line.

Therefore, the present chapter addresses two aspects: First the influence of section load changes on the integral bending moment must be examinded. In the past years several publications have addressed this topic

with respect to an active trailing-edge flap. Although parallels can be drawn the underlying aerodynamic characteristics are different. Second, the interaction of the present concept with the overall control strategy must be explored since different airfoil characteristics will be applied.

These issues clearly indicate that the maximum gain can only be obtained when the present concept is incorporated into the initial design of the turbine. Since this is not the objective of this study a baseline turbine is used and the potential of the concept is estimated under prescribed conditions.

7.1 Simulation Environment

The aerodynamics of wind turbines can be calculated using the blade-element momentum (BEM) theory. The basic assumption is that the momentum exchange between the blade and the air is considered at a discrete blade element and that there is no radial interaction between the elements, see e.g. Burton et al. (2001). The National Renewable Energy Laboratory (NREL) provides the aeroelastic simulator FAST in conjunction with AeroDyn which incorporates the BEM theory (Jonkman and Buhl, 2005).

NREL has further defined an offshore 5 MW reference wind turbine (NREL 5MW RWT). The specifications are given by Jonkman et al. (2009). The machine is a 3-bladed upwind turbine with a rotor radius of 63 m and a hub height of 90 m. The turbine is a variable speed, collective pitch controlled turbine. The cut-in wind speed is 3 m/s, rated speed is 11.4 m/s and cut-off speed is 25 m/s. The aerodynamics are evaluated at 17 blade elements. The blade and the turbine are assumed to be rigid. All deflections have been disabled in FAST.

TurbSim, a stochastic wind field generator developed by Jonkman (2009), has been used to provide generic wind fields for the FAST simulations. The generated wind fields have a size of 145 m × 145 m and were discretized with 31 × 31 points. The chosen time step dt was 0.04 s. The wind loads followed the IEC 61400-1 Ed.3 standard. A Normal Turbulence Model (NTM) class A is considered for three wind speeds: 6, 11.4 and 18 m/s. The corresponding turbulence levels are: 27%, 20% and 18% (see Jonkman (2009, p. 13)). The turbulence spectrum is given by the Kaimal Model. An atmospheric boundary layer with a roughness

length of $z_0 = 0.001\,\mathrm{m}$ is assumed.

The FAST simulations have been performed for a total run time of 630 seconds with a time step dt of $0.004\,\mathrm{s}$. The first 30 seconds were omitted from evaluation of the data. The turbine controller is not considered. The pitch angle and rotor speed have been fixed for each wind speed according to the turbine design.

The assumption of a rigid turbine and the disabled turbine controller are simplifications which influence the absolut results. Nevertheless, for the understanding of the new concept it is preferable to separate the two influences.

7.2 Model Enhancements

The BEM theory calculates an angle of attack from the resultant velocity at each section. The airfoil characteristics are stored in look-up tables from which the corresponding lift, drag and moment coefficient are taken.

The concept of the passive camber change has been incorporated in FAST by modifying these airfoil tables in such a way that they include the characteristics of the concept. The characteristics have been presented in chapter 5.4. It was shown that the airfoil tables can be generated from the potential flow model and the static moment equilibrium around the leading-edge point, to determine the static flap deflection.

The airfoil characteristics of the flexible airfoil are dependent on the design angle of attack and the design freestream velocity. It is possible to define Reynolds number dependent airfoil tables in FAST. For the present case this option was used to recalculate the Reynolds number into a corresponding velocity with the respective chord length at each section. In this manner it was possible to consider the velocity dependence of the camber line. However, it is now crucial to choose the respective design angle and velocity. It is the intention of the next section to outline some guidelines for this task.

The potential flow model is able to predict certain characteristics of the concept, but it is not possible to calculate drag and to consider flow separation. It was seen that the calculated lift coefficients for the cambered airfoil (flaps down) are over predicted. Furthermore, the potential flow considers only steady aerodynamics. Due to the fact that the potential flow model will in general produce higher forces, the airfoil characteristics

for all airfoils used for the blade need to be determined by the potential flow model. This guarantees that the computed change in the subsequent comparison is always related to the same mean loads. In other words the rigid airfoil characteristics were further determined by the potential flow model, and the provided airfoil tables by NREL were not used.

Due to these limitations and modifications some investigations were carried out to assess these assumptions.

To verify the assumption of attached flow the mean angles of attack and mean relative velocities were calculated for a constant wind speed, using the original airfoil data. The results are given in Table 7.1. In the outer part of the rotor blade ($r/R > 0.38$) the mean angles of attack are in the attached flow region. At the inboard part the angles of attack increase but since it is assumed that this part does not contribute in such a manner to the bending moment the error is of minor influence. A comparison of the potential flow calculations and the original airfoil data shows that the mean bending moment, the rotor torque and the power coefficient increase about 5%.

Table 7.1: Comparison of angle of attack and relative velocity along the rotor blade for a constant velocity V_w 11.4 m/s using original airfoil data

r/R	0.19	0.25	0.32	0.38	0.45	0.51	0.58
α_{max}	36.69	30.65	26.92	19.39	16.13	16.17	15.40
α_{mean}	15.03	10.53	8.10	6.53	5.32	4.83	4.43
α_{min}	-0.22	-1.59	-2.26	-2.31	-2.89	-2.56	-2.90
V_{max}	24.46	28.22	33.69	37.90	44.07	47.32	52.44
V_{mean}	18.57	22.91	27.61	32.42	37.31	42.28	47.30
V_{min}	13.01	18.02	21.66	27.04	31.56	37.58	42.08

r/R	0.64	0.71	0.77	0.84	0.89	0.93	0.98
α_{max}	13.21	11.56	12.89	10.86	10.97	10.58	10.64
α_{mean}	4.39	4.81	4.82	4.89	4.91	4.81	4.63
α_{min}	-2.82	-2.24	-1.90	-1.37	-1.01	-0.53	0.00
V_{max}	57.83	62.85	67.89	72.94	77.19	81.22	85.79
V_{mean}	52.34	57.44	62.52	67.63	71.85	75.19	78.51
V_{min}	47.39	51.59	57.87	62.74	66.52	69.65	72.82

Another aspect is the degree of unsteadiness in the change of angle of attack. As explained in the previous section the excitation frequency is of significant influence. Various authors have performed frequency analysis to estimate the power spectral density (PSD) of the frequency content in the angle of attack change. It is obvious that the results will be highly dependent on several parameters e.g. the turbulence level. This can also be seen in the different results provided by Lackner and Kuik (2010), Barlas (2008) and Pierce (1996). The published data show that based on the assumption that changes with a reduced frequency below 0.05 are of steady nature the proportion in the quasi-steady region is between 75% and 90%.

To estimate the frequency content for the wind field used in the present study the PSD was performed at the blade section of 0.77% span. The PSD was calculated with Matlab using an FFT algorithm. For the evaluation of a non-periodic signal in the frequency domain it is essential to treat the signal with a window function. Neglecting the window function would cause an effect known as leakage which would distort the PSD. This effect appears due to the non-periodicity of the signal, more precisely because its magnitude is different at both ends of the considered time array. In using a window function this is rectified. The window used for these calculations is a Hann window which basically consists of a cosine function, bringing the magnitude to zero at both interval ends. The total signal was divided into a number of segments, each overlapping by 50 percent. The PSD of each segment is averaged to obtain the final solution for the PSD of the entire signal (Block averaging).

Figure 7.1 presents the results. The harmonics of the blade rotational frequency are dominant. Integration of the power at these frequencies yields the following results: 46% appear at frequencies larger than $k = 0.01$, 28% appear at frequencies larger than $k = 0.05$ and 16% appear at frequencies larger than $k = 0.1$. That means 72% of the frequency content is below $k = 0.05$ and the assumption of steady aerodynamics is quite reasonable at this stage of the research.

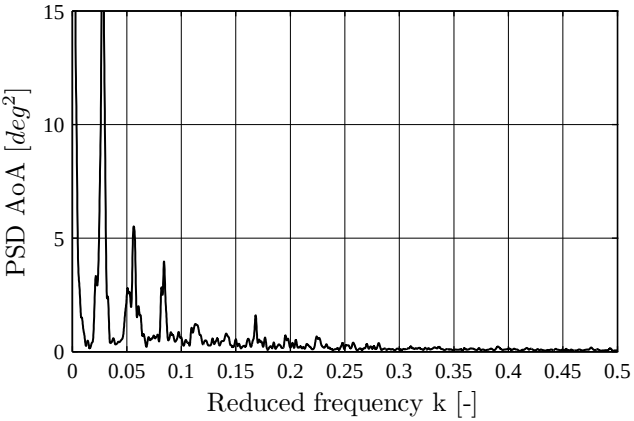

Figure 7.1: Power spectral density of angle of attack at spanwise section 0.77 r/R of NREL 5MW RWT; turbulent windfield: IEC1 class A, $V_w = 11.4m/s$

7.3 Design Points

The conditions under which a wind turbine operates change continually. The main goal of the present concept is to reduce these load fluctuations. However, a passive concept cannot change its characteristics during operations. Therefore, the definition and optimization of a design point is a crucial task.

The highest thrust force occurs on the NREL 5MW RWT at rated speed, see Jonkman et al. (2009, p. 32). The present concept is therefore optimized for the rated wind speed of V_w 11.4 m/s. A further aim is to estimate the behavior of the turbine under off-design conditions. Additionally, the wind speed $V_w = 6\,\mathrm{m/s}$ was chosen to represent a velocity in the partial load region, where the rotational speed is adjusted according to the wind speed, and $V_w = 18\,\mathrm{m/s}$ was chosen to investigate the behavior in the full load region where the pitch angle is normally adjusted.

The highest normal forces on the rotor blade occur at the rated speed in the sections between 70% and 90% rotor span. It is assumed that a camber changing device should preferably be installed in this region. A study on this topic had been performed by Andersen et al. (2006). The NREL turbine consists of four evaluation points in that region (radial positions (RP) 12 ($\equiv 0.71\ r/R$), 13 ($\equiv 0.77\ r/R$), 14 ($\equiv 0.84\ r/R$), 15 ($\equiv 0.89\ r/R$), see Jonkman et al. (2009)). For the present study it is assumed that for each section the concept can be optimized individually. That means the design angle of attack and design velocity changes between the sections; hence different spring constants and preload moments can be applied. Studies have been performed with the modification of one, three and four sections. The results presented here incorporate the modification of four sections. It is obvious that this modification has the highest influence on the load reduction, but it is not clear from the results that it is necessary to modify such a long blade section.

A guide for the calculation of the preload moment and prescription of the spring constant is given in Table 7.2. For the three considered wind speeds the average angles of attack and average resultant velocities are computed for the turbulent wind field. It can be seen that the average angle of attack at these three sections is about $\alpha = 4.8°$ for the rated speed. If the wind speed decreases to $V_w = 6\,\mathrm{m/s}$ the average angle of attack decreases to $\alpha = 2.6°$. The angle of attack decreases to $\alpha = -1.6°$

when the wind speed increases to $V_w = 18\,\mathrm{m/s}$. The velocity changes between $V_w = 11.4\,\mathrm{m/s}$ and $V_w = 18\,\mathrm{m/s}$ are not so large compared to the change in the average velocity of about $20\,\mathrm{m/s}$ when the wind speed is decreased to $V_w = 6\,\mathrm{m/s}$. On the basis of these results it was decided to define the first design point at $\alpha_D = 4.8°$ for all four sections. The following design velocities are defined: $0.71\ r/R \equiv 57\,\mathrm{m/s}$, $0.77\ r/R \equiv 63\,\mathrm{m/s}$, $0.84\ r/R \equiv 68\,\mathrm{m/s}$, $0.89\ r/R \equiv 72\,\mathrm{m/s}$. The trailing-edge flap is $0.2c$, the leading-edge flap is $0.3c$, the coupling ratio $n = 3$, the leading-edge flap angles γ are limited to $\pm 3°$.

Table 7.2: Comparison of angle of attack and relative velocity for different wind speeds at outboard sections

r/R	0.71			0.77			0.84		
V_w	6	11.4	18	6	11.4	18	6	11.4	18
α_{max}	10.59	11.56	8.96	11.19	12.89	6.15	10.95	10.86	5.38
α_{mean}	2.55	4.81	-1.10	2.67	4.82	-1.61	2.88	4.89	-1.96
α_{min}	-2.90	-2.24	-8.57	-2.31	-1.90	-10.73	-1.71	-1.37	-10.60
V_{max}	41.48	62.85	66.37	44.44	67.89	71.78	47.80	72.94	76.24
V_{mean}	37.45	57.44	59.17	40.80	62.52	64.13	44.17	67.63	69.08
V_{min}	33.83	51.59	51.70	36.85	57.87	57.28	40.62	62.74	60.39

The computed airfoil tables are displayed in Figure 7.2. The polars were calculated for velocities between $30\,\mathrm{m/s}$ and $80\,\mathrm{m/s}$ in $5\,\mathrm{m/s}$ increments. The lift-curve slopes have been optimized to exhibit a good behavior over most of the velocities. The design angle of attack is plotted in Figure 7.2. The curves below the design point show the airfoil characteristics (decambered) for higher velocities compared to the design velocity. The curves above the design point describe the airfoil characteristics for lower velocities compared to the design velocity (cambered). The wind tunnel experiment has proven that these types of lift curves can be generated, with one exception. The cambered airfoil generates too much lift since it does not stall. This will be discussed in the next section.

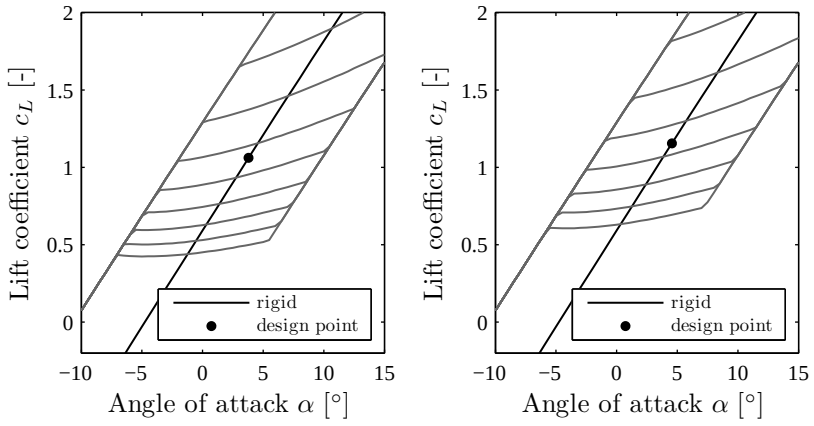

(a) r/R 0.71 **(b)** r/R 0.77

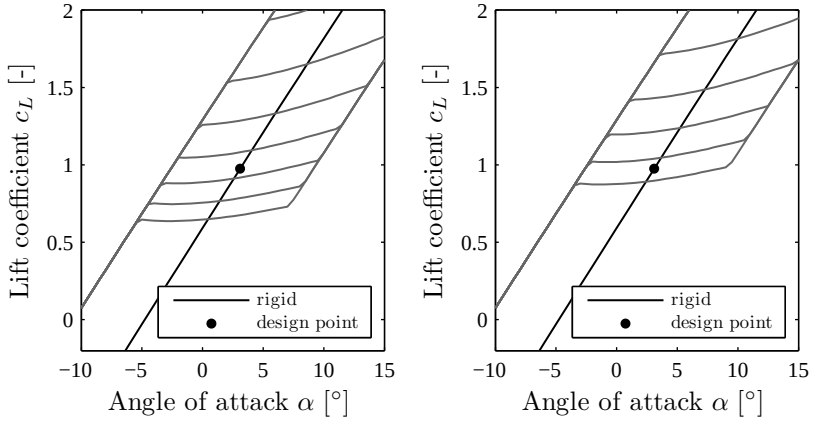

(c) r/R 0.84 **(d)** r/R 0.89

Figure 7.2: Design point 1: lift coefficient polars for radial positions between 0.71% and 0.89% computed with steady panel method; design velocities: 0.71 $r/R \equiv 57\,\mathrm{m/s}$, 0.77 $r/R \equiv 63\,\mathrm{m/s}$, 0.84 $r/R \equiv 68\,\mathrm{m/s}$, 0.89 $r/R \equiv 72\,\mathrm{m/s}$, coupling ratio $n = 3$, leading-edge flap angle γ limited to $\pm 3°$, each polar calculated for velocities between 30 m/s and 80 m/s in 5 m/s increments; velocity increases in curves below design point; velocity decreases in curves above design point;

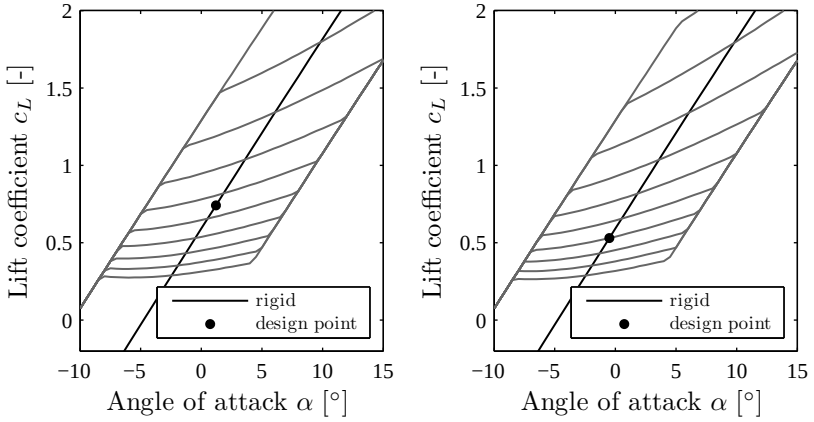

(a) r/R 0.71

(b) r/R 0.77

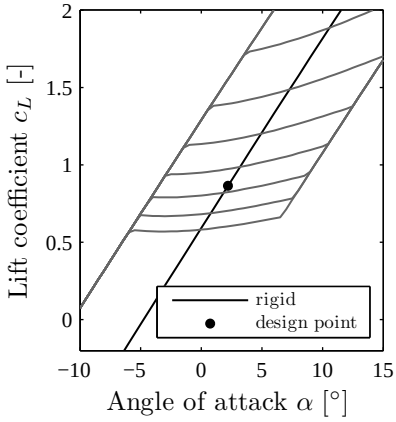

(c) r/R 0.84

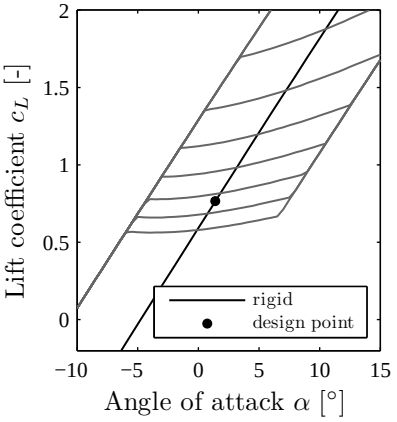

(d) r/R 0.89

Figure 7.3: Design point 2: lift coefficient polars for radial positions between 0.71% and 0.89% computed with steady panel method; design velocities: 0.71 $r/R \equiv 57\,\mathrm{m/s}$, 0.77 $r/R \equiv 63\,\mathrm{m/s}$, 0.84 $r/R \equiv 68\,\mathrm{m/s}$, 0.89 $r/R \equiv 72\,\mathrm{m/s}$, coupling ratio $n = 3$, leading-edge flap angle γ limited to $\pm 3°$, each polar calculated for velocities between 30 m/s and 80 m/s in 5 m/s increments; velocity increases in curves below design point; velocity decreases in curves above design point;

7.4 Results

For the assessment of the results four integral quantities are considered. These are the changes in the flapwise root bending moment M_y, the rotor torque M_t, the rotor thrust T and the power coefficients C_P. The reduction of fluctuation of each quantity is calculated with the help of the standard deviation, here exemplified for the flapwise moment:

$$LR = 1 - \frac{\mathrm{std}\,(M_y)_{\mathrm{flexible}}}{\mathrm{std}\,(M_y)_{\mathrm{rigid}}} \tag{7.1}$$

where flexible means the simulation is using the modified airfoil tables and rigid refers to the computations with the rigid lift-curve slope, see Figure 7.2. Positive values of LR indicate a reduction. Additionally, the change of the mean value of each quantity is compared by

$$MC = 1 - \frac{\mathrm{mean}\,(M_y)_{\mathrm{flexible}}}{\mathrm{mean}\,(M_y)_{\mathrm{rigid}}} \tag{7.2}$$

Note, positive values of MC indicate a reduction, negative values determine an increase of the respective quantity.

The results of design point 1 are summarized in Table 7.3 for the three considered wind speeds. One can see that LR_{My} is 40% for the rated wind speed, which is the design point. Considering the bending moment changes for 6 m/s and 18 m/s one can see that for both velocities the fluctuation has been reduced but the mean bending moment has increased significantly. The lower fluctuation reduction at 6 m/s might has been expected because in this region the airfoil is cambered due to smaller aerodynamic forces. Although the mean bending moment has increased for both velocities, the absolute value is still below the mean bending moment at rated speed.

The reduction of rotor torque fluctuations is small, but a significant increase of the mean torque has occurred for the 18 m/s wind speed. For all three wind speeds the fluctuations in the thrust force were reduced, but again an increase of the mean thrust force has occurred. Considering the power coefficient, a significant increase has arisen at 18 m/s.

After the above assessment, the mean angles of attack and resultant velocities were again computed in the same manner as already presented

Table 7.3: Design Point 1: Comparison of change in integral quantities for the three wind speeds

	LR_{My} [%]	MC_{My} [%]	LR_{Mt} [%]	MC_{Mt} [%]	LR_T [%]	MC_T [%]	LR_{Cp} [%]	MC_{Cp} [%]
6	5.2	-21.4	-0.3	13.8	4.2	-15.9	19.0	16.7
11.4	40.5	-0.3	1.6	3.3	30.0	-0.2	7.2	4.4
18	18.7	-46.0	4.9	-34.7	13.4	-31.9	-26.8	-40.9

for the original data in Table 7.2. It was found that the mean angle of attack decreased when the modified tables were used. This might be explained by the higher induction due to higher lift coefficients. Based on this finding a second design point had been defined in which the design angle of attack was set to $\alpha_D = 2°$. The resulting airfoil tables are displayed in Figure 7.3. It clearly shows that the polars are shifted to lower angles of attack.

The assessment of the simulation results is again summarized in Table 7.4. One can see that the reduction of flapwise bending moment fluctuations has increased for the off-design wind speeds and slightly decreased for rated wind speed. The mean bending moment has also decreased. In conclusion the overall performance has been improved compared to design point 1.

Table 7.4: Design Point 2: Comparison of change in integral quantities for the three wind speeds

	LR_{My} [%]	MC_{My} [%]	LR_{Mt} [%]	MC_{Mt} [%]	LR_T [%]	MC_T [%]	LR_{Cp} [%]	MC_{Cp} [%]
6	8.9	-20.9	-1.3	13.4	7.1	-15.6	18.8	16.4
11.4	36.9	10.1	11.4	5.5	27.6	8.5	0.8	4.2
18	35.2	-28.4	16.5	-20.1	25.0	-19.4	-11.5	-25.8

The above investigation presents an indication of the interaction between the passive adaptation of the camber line and the turbine loads. To explore the characteristics of the cambered airfoil in conjunction with a wind turbine further simulations were performed to investigate how the BEM theory utilizes the modified airfoil tables. It is apparent from the underlying theory that once an angle of attack is computed the cor-

responding lift coefficient will again influence the angle of attack until convergence is reached. Using the modified airfoil tables this interaction becomes more complex. This in turn indicates that it is essential to include the present concept in the initial design to ensure an optimized turbine performance.

Moreover, simulations with a constant wind speed over the entire turbine were performed to explore which points the BEM theory uses on the airfoil tables. These wind speeds are: 4, 6, 8, 10, 11.4, 14, 16 and 18 m/s. The mean angle of attack and mean lift coefficient were computed for the four considered spanwise stations for each wind speed. The result is pictured in Figure 7.4. Each square symbol represents a wind speed. The line begins on the left with the averaged lift coefficient at 4 m/s and moves in clockwise direction to the last square representing 18 m/s. It can be seen that for low wind speeds (4, 6, 8 m/s) the lift coefficient is much higher compared to the rigid airfoil. This was expected and explains why the load reduction at 6 m/s was small. The airfoil is in a cambered position. However, as already mentioned, these lift coefficients are unrealistic since it was observed in the wind tunnel that, due to stall phenomena on the flap, this coefficient might not be generated by the airfoil, which would be beneficial in this case. For the wind velocities 10 and 11.4 m/s the airfoil is in the decambered region. The velocities in the full load region (14, 16, 18 m/s) indicate the advantage of the concept. The velocities do not increase significantly but the angles of attack are reduced (see Table 7.2). In sum the airfoil camber line increases which keeps the lift coefficient constant. This explains why the load reduction at 18 m/s is comparable to the one obtained at rated speed.

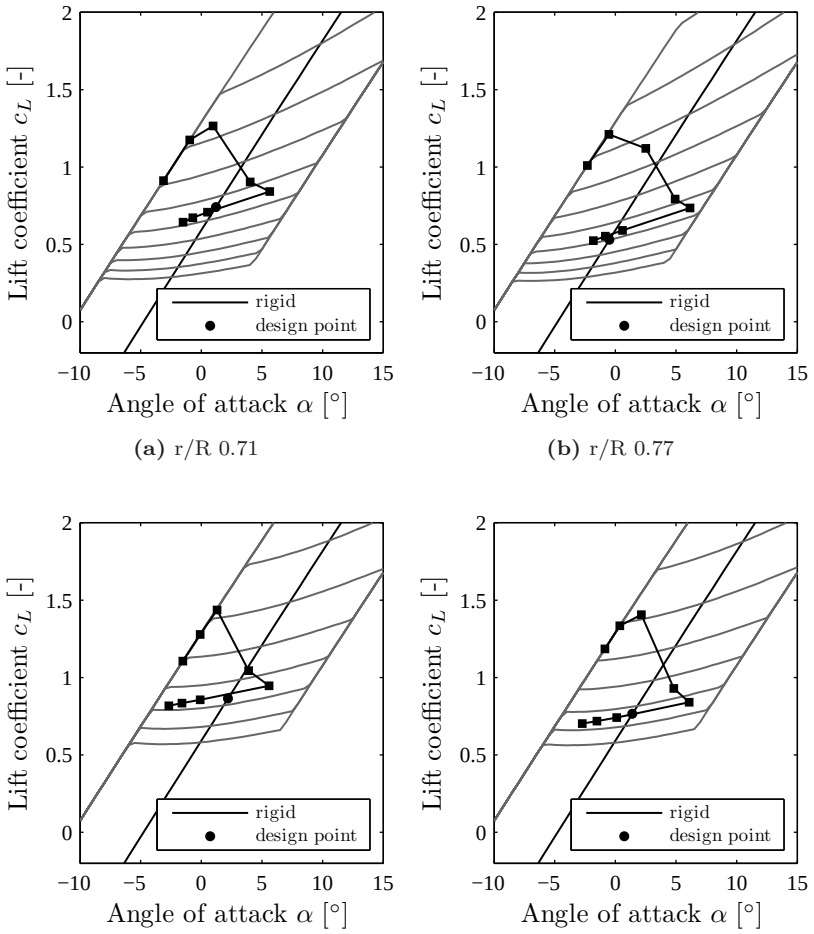

(a) r/R 0.71 **(b)** r/R 0.77

(c) r/R 0.84 **(d)** r/R 0.89

Figure 7.4: Use of airfoil tables for constant wind speed simulations: 4, 6, 8, 10, 11.4, 14, 16 and 18 m/s; square symbol represents a wind speed; line begins on the left with the averaged lift coefficient at 4 m/s and moves in clockwise direction to the last square representing 18 m/s;

Chapter 8

Summary and Outlook

In the present study an airfoil with self-adaptive camber has been developed and investigated experimentally under quasi-steady conditions. The experimental results show that it is possibly to adapt the camber line of an airfoil passively with the use of coupled leading and trailing-edge flaps.

The preliminary design study determined that the flap length of the leading-edge flap should be 20% of the chord length, whereas the trailing-edge flap should be 30% of the chord. It was found that the kinematic coupling ratio should be 2 or 3. The preload moment and stiffness are a function of the design angle of attack and the design velocity. The results showed that significant load reductions were obtained with leading-edge flap deflection of $\pm 2°$.

The experimental results confirmed that a coupling ratio of 2 or 3 is sufficient to realize the potential of the device. The results further showed how important the kinematic coupling is. The leading-edge flap should not only be seen as an actuator for the trailing-edge flap, where its deflections are transferred to the trailing-edge flap. It is of major importance to realize that under certain pressure distributions the trailing-edge flap actuates the leading-edge flap. This is crucial for the aeroelastic stability of the system as a whole. Experiments without a spring; hence without a preload moment, confirm that the flaps move in a stable manner. This is due the fact that under steady conditions a static moment equilibrium is reached.

In the experiments the structural parameters spring stiffness, preload

moment and coupling ratio were evaluated. It was shown that the preload moment can be used to define the mean load level, which is used as a design point. With the help of the coupling ratio and the spring stiffness it was possible to adjust the lift-curve slope. Under certain parameters even a negative lift-slop gradient was obtained.

A comparison with the potential flow model showed that the effects seen in the experiments could have been reproduced with an aeroelastic model. A difference was of course found in the absolute values, since certain aspects are not captured by the aeroelastic model. Especially the aerodynamic forces produced by the potential flow model for the cambered airfoil (flaps down) are higher. The experimental results showed flow separation on the trailing-edge flap, which caused a decrease in the lift-curve slope compared to numerical results.

A numerical investigation of the structural behavior when a pitching and heaving motion of the airfoil is considered in addition to the flap motion shows that in general the dynamic response of the airfoil is improved in terms of reduced heaving amplitudes. The results indicate further that the choice of the spring stiffness needs to be matched to the frequency of the excitation. Since the aerodynamic forces in the aeroelastic model are assumed to be steady an examination using the unsteady formulation of the panel method needs to be carried out.

The application of this concept to wind turbine simulations showed a significant reduction of the flapwise root bending moment fluctuations. The obtained load reductions are remarkably high compared to much lower values given in the literature achieved by using active trailing-edge flaps. This is due to the idealized assumptions in the computation. Further, only one specific wind field has been considered, which does not provide a confidence level. However, the turbine simulation results provide a good guidance for the formulation of the optimization problem.

Finally, it can be concluded that the main goal of this research, namely the development and experimental testing of a passive camber change concept has been achieved. No fundamental obstacles to further development of the concept have been found.

Based on the findings in the present study the following recommendations can be made.

Future experimental investigations can be divided into two aspects:

- Firstly, optimization of the parameter setup using the existing wind tunnel model: Some effort needs to be put into the definition and installation of an optimized spring stiffness. From the results it can be concluded that presumably a nonlinear spring stiffness might improve the aerodynamic behavior. Since the velocity has a major impact on the camber line, a progressive stiffness characteristic could overcome this drawback. At low velocities the deflections should be small. As the velocity increases, the forces increase quadratically, hence the stiffness should increase to incorporate this effect.

- Secondly, a full aeroelastic experiment needs to be conducted. The experimental wing should be extended for a heaving and pitching motion. This can be done by mounting the complete wing elastically in the wind-tunnel. This type of experiment, in combination with an unsteady excitation (gust generator), would finally test the total aeroelastic behavior of the concept. These results would also give more realistic insights in terms of load reduction, since inertial forces are considered.

From a pure aerodynamic point of view investigations need to be carried out to optimize the airfoil shape in conjunction with the flap deflections. The chosen airfoil was used since it is in common use for wind turbine blades. The camber of the airfoil with flap deflections is not ideal and flow separation can be reduced by an improved airfoil shape. It can also be stated that the trailing-edge flap length of 30% is too large.

For the numerical modeling a general statement can be made that the complexity should be kept as low as possible. The panel method predicts the pressure quite well, but in combination with the structural model the computation time can reach several minutes, depending on the considered wind field. The computation time increases for the unsteady panel method, since in each time step a vortex is shed into the wake. The next step will be to couple the structural model to an unsteady aerodynamic formulation. It is recommended to implement a simpler aerodynamic model based on thin airfoil theory. Several models can be found in the literature, e.g. Peters, Hsieh and Torrero (2006) and Gaunaa (2010). Low computation time will still be a key issue in the future design pro-

cess. Additionally, a tool for a stability analysis needs to be implemented, which will be most likely in the frequency domain.

As already stated in the conclusion of the turbine simulation chapter, the underlying polars should be obtained from measurements with the experimental wing, after optimizing the spring stiffness in the above described manner.

References

Abbott, I.H. and Doenhoff, A.E. (1959): *Theory of Wing Sections*. Dover - Edition, Dover Publications

Aghajari, N. (2009): *Konzeption und Numerische Validierung eines 'Morphing-Wing' Versuchsaufbaus*. Master Thesis, TU Darmstadt

Andersen, P.; Gaunaa, M.; Bak, C. and Buhl, T. (2006): Load Alleviation on Wind Turbine Blades using Variable Airfoil Geometry. In *European Wind Energy Conference & Exhibition (EWEC), Athens, Greece, 27 February - 2 March*.

Barlas, T. (2008): Smart Rotor Blade Technology applied to the Upwind Reference Turbine. In *The Application of Smart Structures for Large Wind Turbine Rotor Blades - 56th IEA Topical Expert Meeting, Albuquerque, USA*.

Barlas, T.K. and Kuik, G.A.M. van (2010): Review of State of the Art in Smart Rotor Control Research for Wind Turbines. *Progress in Aerospace Sciences*, Vol. 46 No. 1, pp. 1–27

Barlow, J.B.; Rae, W.H. and Pope, A. (1999): *Low-Speed Wind Tunnel Testing*. 3rd edition. John Wiley & Sons

Behrens, T. and Zhu, W.J. (2011): Feasibility of Aerodynamic Flap Hinge Moment Measurements as Input for Load Alleviation Control. In *EWEA Annual event (formerly known as EWEC), Brussels, Belgium, 14-17 March*.

Berg, D.E.; Wilson, D.G.; Resor, B.R.; Barone, M.F.; Berg, J.C.; Kota, S. and Ervin, G. (2009): Active Aerodynamic Blade Load Control Impacts on Utility-Scale Wind Turbines. In *AWEA Windpower, Chicago, USA*.

Bergami, L. and Gaunaa, M. (2010): Stability Investigation of an Airfoil Section with Active Flap Control. *Wind Energy*, Vol. 13, pp. 151–166

Betz, A. (1926): *Wind-Energie und ihre Ausnutzung durch Windmühlen*. Ökobuch - reprint

Buhl, T.; Gaunaa, M. and Bak, C. (2005): Potential Load Reduction Using Airfoils with Variable Trailing Edge Geometry. *Journal of Solar Energy Engineering*, Vol. 127, pp. 503–516

Burton, T.; Sharpe, D.; Jenkins, N. and Bossanyi, E. (2001): *Wind Energy Handbook*. 1st edition. John Wiley & Sons

Cebeci, T.; M.Platzer; H.Chen; Chang, K.C. and J.P.Shao (2005): *Analysis of Low-Speed Unsteady Airfoil Flows*. 1st edition. Springer-Verlag

Ferber, A. (2010): *Dynamic Load Reduction in Wind Turbine Blades*. Bachelor Thesis, University of Toronto Institute for Aerospace studies (UTIAS) in cooperation with TU Darmstadt

Försching, H.W. (1974): *Grundlagen der Aeroelastik*. 1st edition. Springer-Verlag

Gaunaa, M. (2010): Unsteady Two-Dimensional Potential-Flow Model for Thin Variable Geometry Airfoils. *Wind Energy*, Vol. 13 No. 2-3, pp. 167–192

Goett, H.J. (1939): *Experimental Investigation of the Momentum Method for Determining Profile Drag*. NACA (TR-660). – Technical report

Hansen, M.O.L. (2008): *Aerodynamics of Wind Turbines*. 2nd edition. Earthscan

Hess, J.L. and Smith, A.M.O. (1967): Calculation of Potential Flow about Arbitrary Bodies. *Progress in Aerospace Sciences*, Vol. 8, pp. 1–138

Hoerner, S.F. and Borst, H.V.; Borst, H.V., editor (1985): *Fluid-Dynamic Lift*. 2nd edition. L.A. Hoerner

Johnson, S.J.; Dam, C.P. van and Berg, D.E. (2008): *Active Load Control Techniques for Wind Turbines*. Sandia National Laboratories (SAND2008-4809). – Technical report

Jonkman, B.J. (2009): *TurbSim User's Guide: Version 1.50*. National Renewable Energy Laboratory (NREL/TP-500-46198). – Technical report

Jonkman, J.M. and Buhl, M.L. Jr. (2005): *FAST User's Guide*. National Renewable Engergy Laboratory (NREL/EL-500-38230). – Technical report

Jonkman, J.M.; Butterfield, S.; Musial, W. and Scott, G. (2009): *Definition of a 5-MW Reference Wind Turbine for Offshore System Development*. National Renewable Energy Laboratory (NREL/TP-500-38060). – Technical report

Kallesø, B.S. (2006): A Low-order Model for Analysing Effects of Blade Fatigue Load Control. *Wind Energy*, Vol. 9, pp. 421–436

Kane, T.R. and Levinson, D.A. (1985): *Dynamics: Theory and Application*. 1st edition. McGraw-Hill

Karamcheti, K. (1980): *Principles of Ideal-Fluid Aerodynamics*. 2nd edition. Krieger Publishing

Katz, J. and Plotkin, A. (2001): *Low-Speed Aerodynamics*. 2nd edition. Cambridge University Press

Lackner, M.A. and Kuik, G.v. (2010): A Comparison of Smart Rotor Control Approaches using Trailing Edge Flaps and Individual Pitch Control. *Wind Energy*, Vol. 13 No. 2-3, pp. 117–134

Lambie, B.; Krenik, A. and Tropea, C. (2010): Numerical Simulation of an Airfoil with a Flexible Trailing Edge in Unsteady Flow. In *51st AIAA/ASME/ASCE/AHS/ASC Structures, Structural Dynamics and Materials Conference, Orlando, USA.*

Lecheler, S. (2009): *Numerische Strömungsberechnung.* 1st edition. Vieweg+Teubner

Leishman, J.G. (2006): *Principles of Helicopter Aerodynamics.* 2nd edition. Cambridge University Press

Lobitz, Don W. (2004): Aeroelastic Stability Predictions for a MW-Sized Blade. *Wind Energy*, Vol. 7 No. 3, pp. 211–224

Menter, F.R. (1994): Two-Equation Eddy-Viscosity Turbulence Models for Engineering Applications. *AIAA Journal*, Vol. 32 No. 8, pp. 1598– 1605

Moran, J. (1984): *An Introduction to Theoretical and Computational Aerodynamics.* Dover Publications - Reprint

Nitsche, W. and Brunn, A. (2006): *Strömungsmesstechnik.* 2nd edition. Springer-Verlag

Peters, D.A.; Hsieh, M.A. and Torrero, A. (2006): A State-Space Airloads Theory for Flexible Airfoils. In 62^{nd} *Annual Forum of the American Helicopter Society, Phoenix, USA.*

Pierce, K.G. (1996): *Wind Turbine Load Prediction using the Beddoes-Leishman Model for Unsteady Aerodynamics and Dynamic Stall.* Master Thesis, Univeristy of Utah

Prandtl, L. and Betz, A. (1927): *Ergebnisse der Aerodynamischen Versuchsanstalt zu Göttingen, III. Lieferung.* R. Oldenbourg, München und Berlin

Schäfer, M. (1999): *Numerik im Maschinenbau.* 1st edition. Springer-Verlag

Send, W. (1992): The Mean Power of Forces and Moments in Unsteady Aerodynamics. *Zeitschrift für Angewandte Mathematik und Mechanik*, No. 2, pp. 113 – 132

Send, W. (1995): *Zur Lösung des räumlichen Interferenzproblems in der Instationären Aerodynamik*. DLR (95-42). – Technical report

Sippola, M. and Lindroos, T. (2009): Modelling and Testing of a Load-Limiting Sandwich Structure. In 8^{th} *European Symposium on Martensitic Transformations (ESOMAT), Prague, Czech.*

Spurk, J. and Aksel, N. (2006): *Technische Strömungslehre*. 6th edition. Springer-Verlag

Veers, P.; Bir, G. and Lobitz, D. (1998): Aeroelastic Tailoring in Wind Turbine Blade Applications. In *AWEA Windpower, Bakersfield, USA.*

Appendix A

Verification Panel Method

Steady Formulation

The steady formulation of the Hess-Smith panel method was verified with inviscid XFoil computations. Figure A.1 to A.5 show various comparisons for a NACA 4415 and the NACA 64_3618. The results document that the panel method is implemented correctly. However, it should be noted that the method is sensitive to the airfoil coordinates. The quality of the NACA 4415 coordinates is higher compared to the NACA 64_3618 coordinates. Therefore, the results between HSPM and XFoil for the NACA 4415 are identical. Further, it should be noted that the number of panels has clearly an impact, especially on the moment coefficient, as can be seen in Figure A.3. The deviation in the pressure distribution in the region of the flap hinge point results from different panel discretization between XFoil and HSPM implementation.

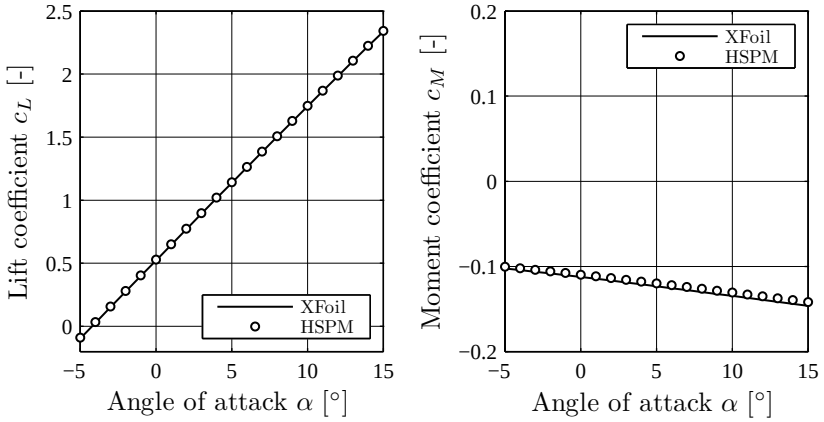

Figure A.1: Comparison of lift and moment coefficient about quarter point: XFoil and HSPM, NACA 4415, panel number $n = 160$;

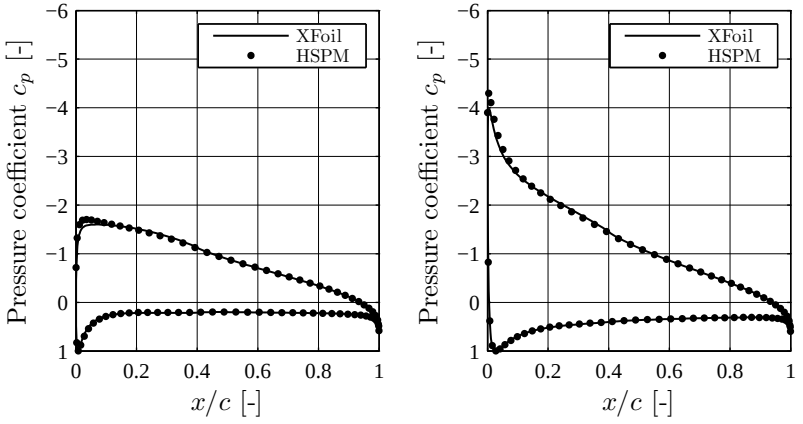

(a) $\alpha = 5°$ **(b)** $\alpha = 10°$

Figure A.2: Comparison of pressure coefficient: XFoil and HSPM, NACA 4415, panel number $n = 160$;

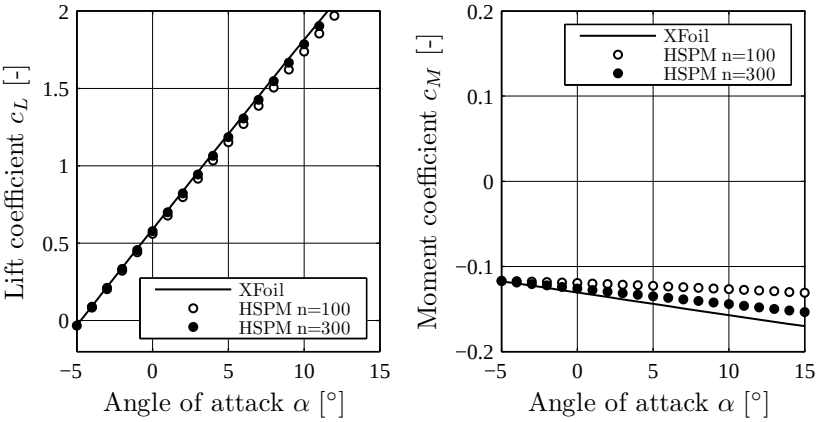

Figure A.3: Comparison of lift and moment coefficient about quarter point: XFoil and HSPM, NACA 64_3618;

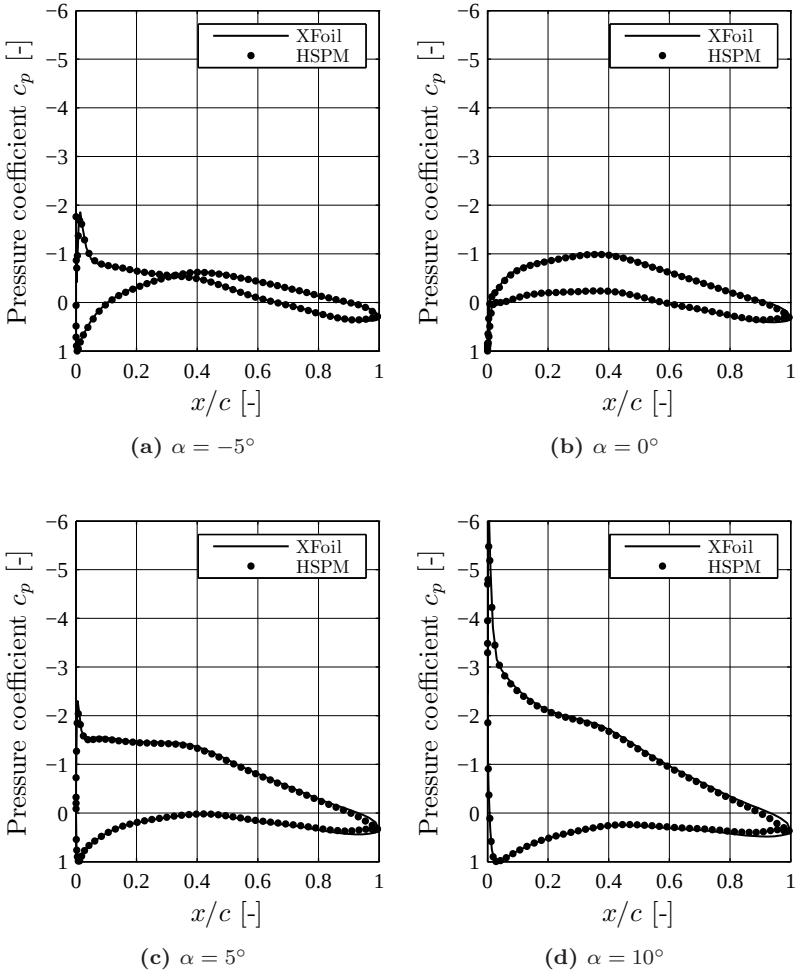

(a) $\alpha = -5°$ **(b)** $\alpha = 0°$

(c) $\alpha = 5°$ **(d)** $\alpha = 10°$

Figure A.4: Comparison of pressure coefficient: XFoil and HSPM, NACA 64_3618, panel number $n = 100$;

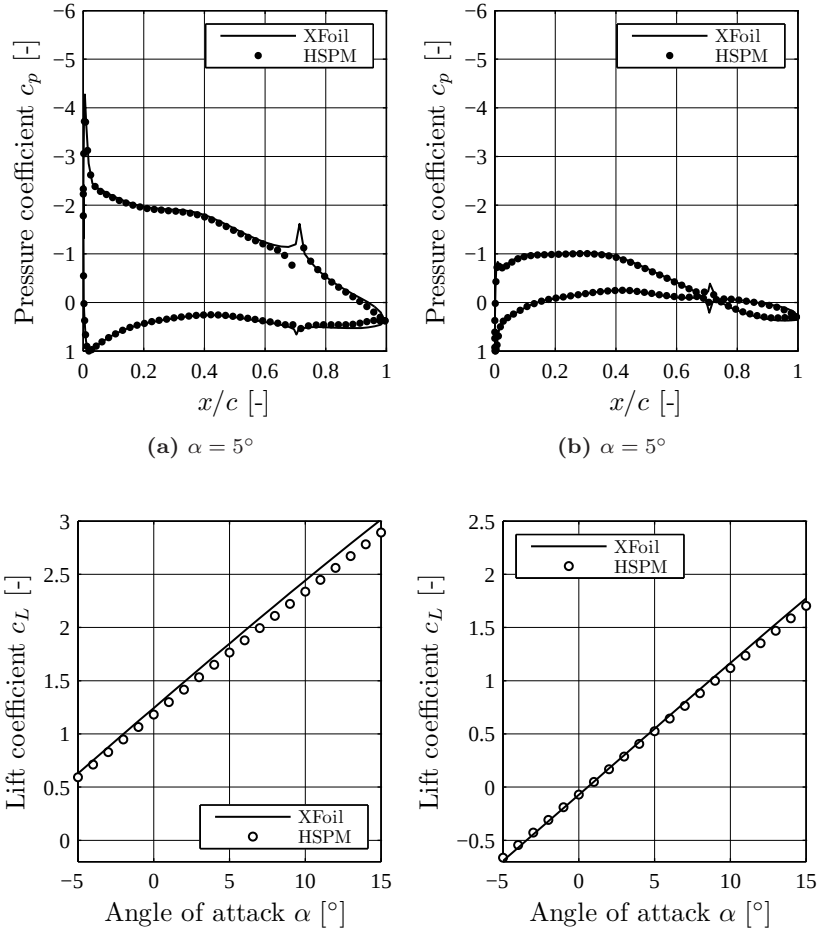

(a) $\alpha = 5°$ **(b)** $\alpha = 5°$

Figure A.5: Comparison of pressure and lift coefficient: XFoil and HSPM, NACA 64_3618, panel number $n = 100$;
Left column: Flap deflected down $\beta = -8°$;
Right column: Flap deflected up $\beta = 8°$;

Unsteady Formulation

The verification of the unsteady Hesse-Smith formulation was achieved by a comparison with the model of Gaunaa (2010). The Gaunna model is an unsteady, inviscid 2D potential flow model for thin airfoils. The model allows to calculated variable chordwise deflections and is therefore capable to consider flap deflections. To match the assumption of thin airfoils the UHSPM calculations were carried out for a NACA 0001 airfoil. Figure A.6 and A.7 compare the model results for a combined pitching and heaving motion of the airfoil. Reduced frequencies k of 0.1 and 1 in terms of the pitching frequency were chosen. Figure A.8 shows the comparison where additionally a flap motion is superimposed to the pitching and heaving motion. The results show that the model is implemented correctly although for higher reduced frequencies some deviation is presented. This is related to the different formulations of the models.

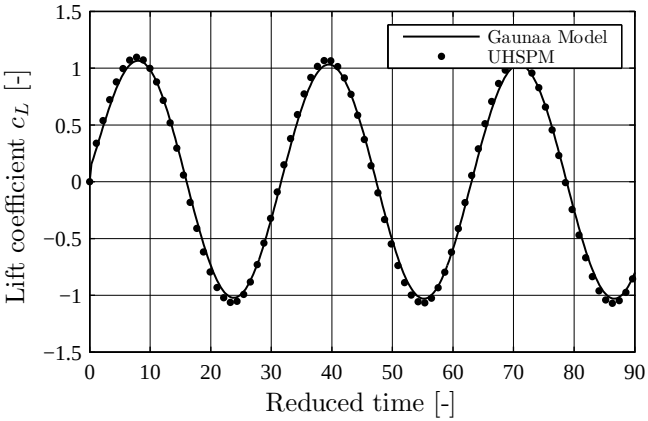

Figure A.6: Comparison of unsteady lift coefficient for a sinusoidal pitching and heaving motion; $k = 0.1$; $\alpha_0 = 10°$; $h_0 = 0.1c$; NACA 0001;

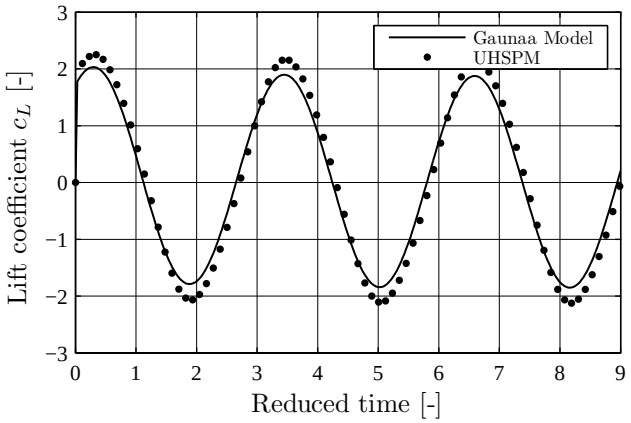

Figure A.7: Comparison of unsteady lift coefficient for a sinusoidal pitching and heaving motion; $k = 1$; $\alpha_0 = 10°$; $h_0 = 0.1c$; NACA 0001;

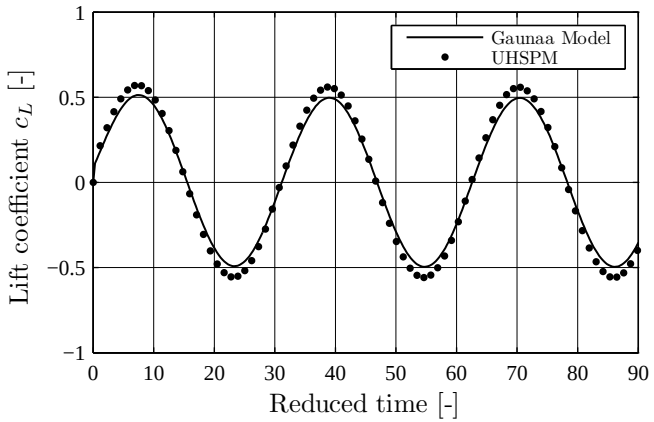

Figure A.8: Comparison of unsteady lift coefficient for a sinusoidal pitching and heaving motion including flap motions; $k = 0.1$; $\alpha_0 = 10°$; $h_0 = 0.1c$; $\gamma_0 = 3°$; $n = 3$; NACA 0001;

Appendix B

Verification RANS Domain

The freeflow domain size was determined by the comparison of the velocity distribution over the height with the freestream velocity. One can see from Figure B.1 that the velocity at $0.25c$ behind the inlet is equal to the freestream velocity, i.e. the disturbance of the airfoil is not present at the inlet. At the outlet a small velocity difference exists.

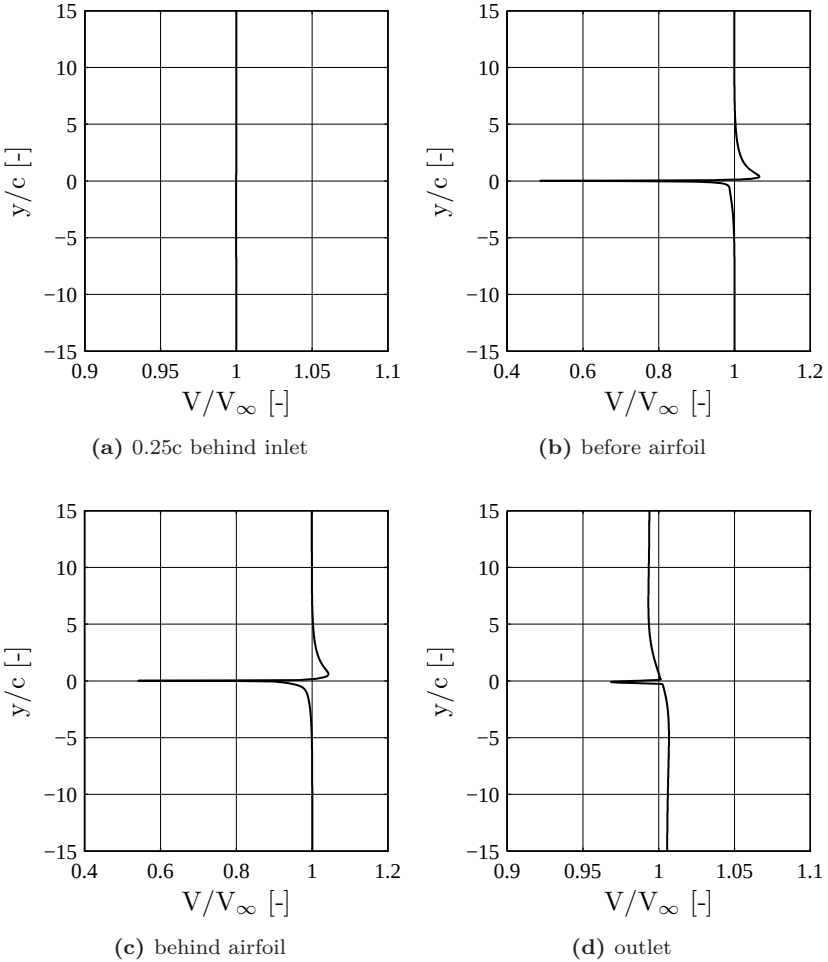

(a) 0.25c behind inlet

(b) before airfoil

(c) behind airfoil

(d) outlet

Figure B.1: Comparison of local velocity to freestream velocity at different streamwise positions over domain height; RANS computation at $V_\infty = 40\,\mathrm{m/s}$ for the freeflow domain

Lebenslauf

Persönliche Daten

Benjamin Lambie

Geboren am 17.08.1980 in Essen
Ledig, deutsch

Schulausbildung

1991 - 2000	Adolf-Reichwein-Gymnasium in Heusenstamm
Juni 2000	Abschluss: Allgemeine Hochschulreife

Studium

10/2001 - 07/2007	Allgemeiner Maschinenbau an der Technischen Universität Darmstadt
01/2007 - 06/2007	Studienaufenthalt i.R.d. ERASMUS-Programms an der University of Glasgow, Glasgow, UK
Juli 2007	Abschluss: Diplom-Ingenieur

Promotionsstudium

03/2008 - 04/2011	Exzellenzcluster 259 „Smart Interfaces - Understanding and Designing Fluid Boundaries “ der Technischen Universität Darmstadt

Darmstadt, 27. April 2011